Review

State of the practice on energy-based liquefaction evaluation and research significance

Takaji Kokusho*

Professor Emeritus, Department of Civil & Environmental Engineering, Chuo University, Tokyo, 112-8551, Japan

* **Correspondence:** Email: koktak@ad.email.ne.jp; Tel: +81-90-1459-4857.

Abstract: Since the 1964 Niigata and Alaskan earthquakes, which incurred severe liquefaction damage, liquefaction-related design for infrastructures and buildings has been developed exclusively on the principle of force equilibrium. However, the energy concept is increasingly recognized as superior for simplified and robust liquefaction designs because of the uniqueness of energy capacity in soil failures regardless of the differences in earthquake loads. The energy-based liquefaction evaluation method (EBM) has been pursued by many investigators where dissipated energy for liquefaction is focused in place of liquefaction strength defined in the conventional stress-based method (SBM). Furthermore, the EBM enables sound liquefaction-related designs without resorting to sophisticated but highly variable/tricky numerical analyses and contributes as a scale to measure the reliability of those numerical tools. Thus, the EBM, though short of practical use in today's engineering works, should be able to serve as a simplified liquefaction evaluation tool besides the SBM. We reviewed the basic idea as well as the recent developments of the EBM together with the supporting data. We also discussed how to simplify and approximate the energy-based liquefaction behavior to implement robust evaluations in practical problems. The EBM liquefaction evaluation steps were delineated and exemplified by case studies for practicing engineers compared to the SBM.

Keywords: soil liquefaction; dissipated energy; earthquake-wave energy; energy capacity; energy demand; pore-pressure buildup; induced strain; settlement; laboratory test; vertical array records

1. Introduction

In the 1960s the great impact of earthquake-induced liquefaction on the sustainability of a modern society was first recognized when the Alaskan and Niigata earthquakes incurred severe damage to urban infrastructures and buildings constructed on poor soils of newly urbanized lowlands. Since then, liquefaction damage has occurred often in many countries around the world as one of the serious impacts on the sustainability and resilience of society. As populations and economies are growing rapidly in developing countries, urbanization in lowlands of poor soil conditions will make the liquefaction threats more serious because of the rising groundwater table due to surging sea levels deemed to be inevitable in global warming. Thus, the liquefaction mitigation of urban facilities is increasingly prioritized in engineering designs not only in developed but also in developing countries.

Moreover, from the dawn of the liquefaction research, a stress-based method (SBM), wherein undrained cyclic strength as liquefaction capacity compares with seismically induced shear stress as liquefaction demand, has been developed (Seed & Idriss 1971 [1]), and standardized in engineering practice for liquefaction potential evaluations in many design codes worldwide. In its simplified procedure wherein the earthquake effect is idealized by harmonic stress of a given amplitude and given cycles, the cyclic resistance ratio (CRR) is determined by in situ tests such as Standard Penetration Tests (SPTs) or Cone Penetration Tests (CPTs) using their depth-dependent penetration resistances plus pertinent soil parameters (fines content F_c and plasticity index I_p), while the earthquake-induced cyclic stress ratio (CSR) is calculated from peak ground horizontal acceleration (PGA) assuming depth-dependent stress decay curves or SH-wave propagation analyses using design acceleration motions. However, the liquefaction behavior is not governed solely by applied stress but also by earthquake-induced shear strain and associated soil dilatancy which builds up the pore pressure in undrained saturated soils. Hence, not only earthquake-induced stresses but also other pertinent parameters governing strains are needed to make relevant liquefaction evaluations.

Apart from that, a possibility of a unified liquefaction theory was first presented (Nemat-Nasser and Shokooh, 1979 [2]), which paved the way to develop the energy-based method for liquefaction evaluation (EBM). Instead of the SBM, it focuses on dissipated energy determined from the stress versus strain relationship causing dilatancy and pore-pressure buildup for liquefaction during cyclic loading. Since then, quite many experimental efforts have been made to confirm and demonstrate the superiorities of the EBM compared to the SBM.

As obvious merit of the EBM, Figure 1 exemplifies undrained torsional simple shear test results on medium loose clean sand ($D_r \approx 50\%$) cyclically loaded by two widely varied earthquake motions: (a) The 2011 Tohoku earthquake ($M_J = 9.0$: M_J = Japanese Meteorological Agency Magnitude similar to the surface-wave magnitude M_s) lasting more than 4 minutes, and (b) 1995 Kobe earthquake ($M_J = 7.2$) lasting only 20 seconds. This indicates that the cumulative dissipated energy normalized by initial effective confining stress $\sum \Delta W / \sigma'_c$ in the horizontal axis can uniquely predict the pore-pressure buildup ratio $r_u = \Delta u / \sigma'_c$ despite the tremendous difference between the two motions in amplitudes, time durations, and waveforms. This implies that whatever earthquake motions are in terms of intensities, focal distances, durations, waveforms, predominant frequencies, irregularities, etc., the liquefaction behavior in terms of pressure buildup is determined exclusively by the cumulative energy dissipated in soils $\sum \Delta W$ during earthquake motions.
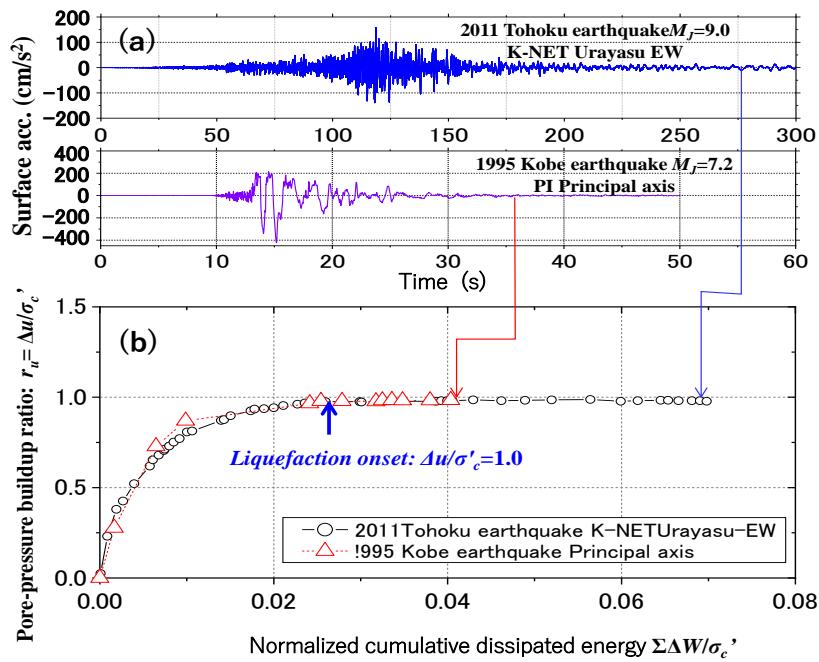
Figure 1. Unique correlation of cumulative dissipated energy versus pore-pressure buildup ratio for two different earthquake motions.

The SBM, in contrast, has to properly choose pertinent parameters critical to make a reliable prediction. Despite such advantages of the EBM, it has rarely been used in engineering practice partly because the SBM has long been authorized in design manuals as a standardized evaluation procedure in the historical background of the force-equilibrium using acceleration in earthquake engineering in general.

However, with the maturity of the EBM research and the increasing need for more reasonable and robust liquefaction evaluation tools, the energy-based liquefaction design method should be authorized so that it can be followed widely by practicing engineers to prepare for increasing liquefaction threats to resilient and sustainable societies.

In this review article, major research developments of the energy-based liquefaction evaluation method (EBM) are summarized by revisiting major previous research. Then, the EBM is discussed concerning the issues.

- How to determine capacity energy (dissipated energy) for liquefaction
- How to evaluate demand energy (earthquake wave energy) from design earthquake motions or relevant parameters
- How to compare the capacity energy with the demand energy to make a reasonable and simplified liquefaction evaluation.

Theoretical backgrounds and experimental data associated with these issues are also addressed to discuss in comparison with the SBM whenever necessary.

Finally, the evaluation procedures of the EBM in engineering practice are delineated step by step based on preceding discussions, which are followed by a couple of case studies to demonstrate its features and differences compared to the SBM.

2. Previous research on energy-based methods

The energy-based liquefaction evaluation method (EBM) was first proposed by Davis and Berrill (1982) [3] and Berrill & Davis (1984) [4], followed by Law et al. (1990) [5]. In their model, the pore-pressure buildup for liquefaction was correlated with the capacity energy represented by dissipated energy expressed as a function of in situ penetration resistance. The demand energy was seismologically given as a function of earthquake magnitude and hypocenter distance by Gutenberg (1956) [6]. It was motivated by the pioneering research on energy capacity for liquefaction by Nemat-Nasser and Shokooh [2].

Since then, the uniqueness of dissipated energy or energy capacity in the liquefaction behavior has been experimentally demonstrated by quite many test data in various laboratory cyclic loading tests. Among them, Towhata and Ishihara (1985) [7] conducted hollow cylindrical torsional shear tests with various loading paths in which a unique relationship was found between shear work (dissipated energy) and excess pore-pressure buildup to be independent of the shear stress path. Yanagisawa and Sugano (1994) [8] conducted similar cyclic shear tests using irregular time histories and found again the uniqueness of cumulative energy on the pressure buildup. Laboratory soil tests were also conducted in a strain-controlled torsional shear test by Figueroa et al. (1994) [9], demonstrating the uniqueness of dissipated energy in pore-pressure buildup under different confining stresses. Baziar and Sharafi (2011) [10] conducted stress-controlled undrained cyclic torsional tests on silty sands under different confining stresses and found that the dissipated energy for pore-pressure buildup is independent of *CSR* but highly dependent on the effective confining pressure and fines content. Pan and Yang (2017) [11] and Azeiteiro et al. (2017) [12] both presented systematic cyclic triaxial test results with irregular time histories to find that the pore-pressure generation and the number of cycles for liquefaction are significantly influenced by the stress amplitudes and their sequence. Conversely, a unique relationship was found between the cumulative dissipated energy and the pore pressure wherein the effect of loading conditions can be ignored, indicating a superiority of the energy-based approach.

Empirical relationships correlating the dissipated energy with the pore-pressure buildup ratio were developed by Green et al. (2000) [13] and Jafarian et al. (2012) [14] to be used for liquefaction evaluations. Furthermore, the dissipated energy concept has been employed in evaluating liquefaction resistance in practical engineering problems such as plant-rooted soils (Karimzadeh et al. 2021) [15] and calcium-carbonate treated sands (Baziar and Alibolandi 2023) [16] by developing their energy versus *CRR* relationships.

Apart from those mainly concerned with pore-pressure buildup, Kazama et al. (2000) [17] carried out strain-controlled cyclic triaxial tests to focus on the dissipated energy evaluated in stress ~ strain hysteretic loops even after 100% pressure-buildup to take soil ductility into account in liquefaction design. Kokusho (2013) [18] summarized a series of their own cyclic triaxial test results by harmonic loading and found that the cumulative dissipated energy is uniquely correlated with not only pore-pressure buildup but also induced strain not only up to 100% pore-pressure buildup (initial liquefaction) but beyond. Hence, unlike the pressure buildup, the strain can serve as an index to evaluate the severity of liquefaction even after the onset of liquefaction. In torsional simple shear tests on loose sands without/with non-plastic fines, Kokusho and Kaneko (2018) [19] confirmed the uniqueness of $\Sigma\Delta W$ in determining liquefaction-induced strain not only for harmonic motions but also a variety of earthquake motions.

In some of the research, using reconstituted sand specimens, $\Sigma\Delta W$ in EBM and *CRR* in SBM were found to be uniquely correlated despite wide differences in relative density and fines content in triaxial tests [18] and in torsional tests [19]. Furthermore, Kokusho and Tanimoto (2021) [20] visited a set of cyclic triaxial test results on numerous intact soils sampled from various sites, wherein a unique correlation between the dissipated energy $\Sigma\Delta W$ and *CRR* for the number of cycles for initial liquefaction N_L = 15 or 20 was developed irrespective of soil types.

Thus, a close correlation between the dissipated energy and the excess pore pressure or induced strain has been found and a great possibility of the EBM for liquefaction evaluation has been demonstrated in the previous research. Nevertheless, its application has been very limited so far in contrast to the conventional SBM in engineering practice. One of the reasons besides the historical background may be because concrete/detailed procedures for the EBM have not been discussed concerning how to evaluate the demand (earthquake wave energy) in particular and how to compare it with the capacity (dissipated energy), simply and reasonably.

In the earlier EBM papers [3–5], both capacity and demand energies were not explicitly quantified but intuitively represented respectively by SPT N-values and by well-known empirical formulas in seismology [6]. Namely, a liquefaction triggering curve was given as a boundary curve drawn on a chart of capacity versus demand energies segregating site-specific manifestation plots into occurrence and non-occurrence of liquefaction in case history records at various sites during past earthquakes. In a similar approach based on previous liquefaction case histories, Kayen and Mitchell (1997) [21] used Arias Intensity (1970) [22] as a demand for liquefaction potential evaluation, although the Arias Intensity was defined to be different from the energy in its physical meaning. Apart from the above, in the EBM proposed by Kazama et al. [17], the earthquake demand was not quantified to directly compare with the capacity energy, but a dynamic response analysis using design earthquake motions was carried out instead, to implicitly compare with the dissipated energy.

Moreover, Kokusho (2013) [18] developed another type of EBM wherein upward seismic wave energies are quantified as the demand energies and directly compared with dissipated energies at individual soil layers. Theoretical backgrounds of the comparison were discussed by Kokusho (2017) [23] on how to evaluate the energy of design motions and compare it with the dissipated energy based on laboratory soil tests. How to quantify the demand energy during earthquakes was first investigated based on an energy flow model of SH-wave using vertical array records during the 1995 Kobe earthquake by Kokusho & Motoyama (2002) [24] followed by Kokusho & Suzuki (2011, 2012) [25,26] using numerous vertical array data during strong earthquakes throughout Japan.

Kokusho and Mimori (2015) [27] conducted EBM studies on a hypothetical uniform soil deposit as well as actual liquefaction case histories where geotechnical data and recorded earthquake motions nearby were available. In the former, the significant impact of predominant frequency on the liquefaction potential was vividly shown. In the latter, the results demonstrated that, for several ground motions, the EBM tends to be mostly compatible with the SBM, if stress reduction coefficients r_n, similar to Magnitude Scaling Factors, *MSF*, in the USA (e.g. Idriss and Boulanger 2008) [28], are properly chosen in SBM. However, the gap between them tended to widen for ground motions with exceptionally large or small demand energy compared to the corresponding acceleration. In those cases, the EBM successfully replicated actual field performance whereas SBM could not properly appreciate the great impact of the demand energy.

Lau et al. (2019) [29] conducted comparative studies of the EBM developed by Kokusho [18] at several sites in Christchurch utilizing strong motion records during the 2010–2011 Canterbury

Earthquake sequence and also at three sites in the Wellington and Marlborough for the 2013 Lake Grassmere and 2016 Kaikoura earthquakes in New Zealand. The method was compared with the SBM evaluation recommended by Idriss & Boulanger [28] concerning critical liquefaction depth and layer thickness, data scatter, and the number of false-negative (unconservative) predictions. As a result, the EBM was confirmed to make the least unconservative predictions compared to the CPT-based SBM, while yielding comparable results to the SBM as a whole.

Besides, the base-isolation mechanism of upward wave energy caused by soil liquefaction has also been investigated from the viewpoint of energy demand by Kokusho (2014) [30]. Furthermore, Kokusho (2020) [31] developed simplified evaluation steps to predict not only liquefaction potential but also associated induced strain and soil settlement, if liquefied, by assuming an equal allocation of the demand energy to potentially liquefiable layers. This reflects one of the excellent features of the EBM; total demand energy available is quantified to pursue the overall liquefaction behavior of a given site by allocating it among multiple potentially liquefiable layers. In contrast, no such interlayer interference of acceleration can be considered in the global liquefaction development of a site in the SBM.

Thus, after having revisited the previous research in this Chapter, the energy capacity is first dealt with in detail in Chapter 3 by utilizing various laboratory soil test data on reconstituted as well as intact natural soils to discuss the uniqueness of dissipated energy despite the variability of pertinent parameters in developing liquefaction. Then, in Chapter 4, wherein the energy demand, defined as cumulative upward energy by the SH-wave, is discussed concerning theories and earthquake records on how to compare with the capacity energy for liquefaction evaluation. Most of the data incorporated here are cited from previous papers in the references published by our research group.

3. Energy capacity for liquefaction

In this Chapter, cyclic triaxial test results on reconstituted specimens are first addressed to summarize correlations of the dissipated energy with pore-pressure buildup and induced strain to examine the effects of relative density, fines content, and effective confining stress. Similar results on intact soils from in situ are also addressed to discuss the impact of natural soils on dissipated energy. In these tests, dissipated energy is compared with corresponding resistant stress *CRR* in the SBM for liquefaction onset to find a unique relationship between them. Then, torsional simple shear tests, which can more closely mimic in situ stress conditions during earthquakes, are addressed to recognize the similarity of the dissipated energy with that in the triaxial tests. Finally, the effect of wave irregularity of various earthquakes on the liquefaction behavior is discussed based on the torsional tests from the viewpoint of the uniqueness of dissipated energy.

3.1. Triaxial tests on reconstituted specimens by harmonic loading

A series of stress-controlled undrained cyclic triaxial tests were carried out [18] using reconstituted specimens of Futtsu beach sand (along the Tokyo Bay), non-weathered sub-round particles with the mean grain size $D_{50} = 0.19$ mm, and the uniformity coefficient $C_u = 1.9$. The size of the specimen was 10 cm in diameter and 20 cm in height. In some of them, low-plasticity fines, (the plasticity index $I_p = 6$) originated from decomposed granite was mixed with parametrically changing fines content $F_c = 0\sim20\%$.

All the samples with various target relative densities D_r were consolidated to effective stress of $\sigma'_c = 98$ kPa, with back-pressure of 196 kPa, and cyclically loaded with frequency 0.1 Hz under an undrained condition with constant axial stress amplitudes σ_d. Following the SBM practice, Figure 2 shows cyclic stress ratios $CSR = \sigma_d/2\sigma'_c$ in isotropically consolidated triaxial tests versus the number of load cycles N_c plotted on the log-log chart to attain double-amplitude (DA) axial strain $\varepsilon_{DA} = 5\%$ and pore-pressure buildup ratio $\Delta u/\sigma'_c = 1.0$ for all the tests; (a) clean sands (F_c=0) with $D_r \approx 30, 50,$ 70%, (b) $F_c = 0\sim20\%$ with $D_r \approx 50\%$ and (c) $F_c = 0\sim20\%$ with $D_r \approx 70\%$. Then, the plots for $\varepsilon_{DA} = 5\%$ in the chart are approximated by lines regressed by the following empirical formula with positive constants a and b, which are listed in the chart;

$$CSR = aN_c^{-b} \tag{1}$$

Despite data scatters, the CSR-values for $\varepsilon_{DA} = 5\%$ and $r_u = 1.0$ tend to increase systematically with increasing D_r and decreasing F_c. From the regression lines for $\varepsilon_{DA} = 5\%$, cyclic resistance ratio $CRR = \sigma_d/2\sigma'_c$ in isotropically consolidated triaxial tests is determined as $CRR = CSR$ at the number of cycles $N_c = N_L = 15$ as summarized in Figure 2 for the initial liquefaction to be used in the normal SBM practice.
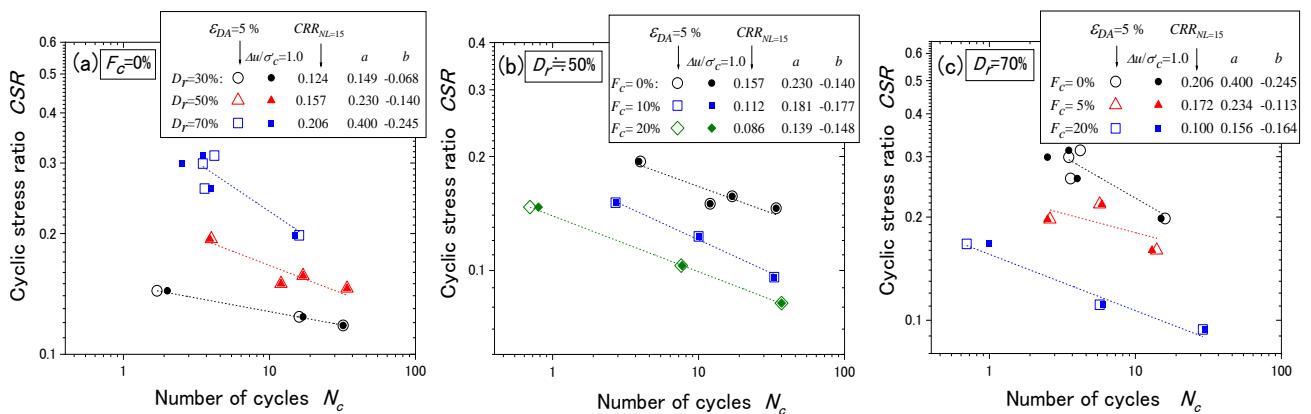

Figure 2. CSR versus N_c plots by undrained cyclic triaxial tests on reconstituted Futtsu sand: (a) $D_r \approx 30, 50, 70\%$ ($F_c = 0\%$), (b) $F_c = 0, 10, 20\%$ ($D_r \approx 50\%$), and (c) $F_c = 0, 5, 20\%$ ($D_r \approx 70\%$).

3.1.1.   Dissipated energy versus pore-pressure and shear strain in triaxial shear tests

Figure 3(a) exemplifies a typical cyclic stress-strain relationship for $D_r = 51\%$ and $F_c = 0\%$. Dissipated energy per unit volume in the test specimen is calculated from a hysteretic area ABCD of a thick dashed curve for a k-th stress cycle and summed up to have a cumulative value from the start to that cycle as;

$$\sum \Delta W = \sum_k \left(\int_A^D \sigma_d d\varepsilon \right)_k \tag{2}$$

The details of this energy calculation from the stress versus strain hysteresis curve will be addressed again in torsional shear tests in Eq. (7).
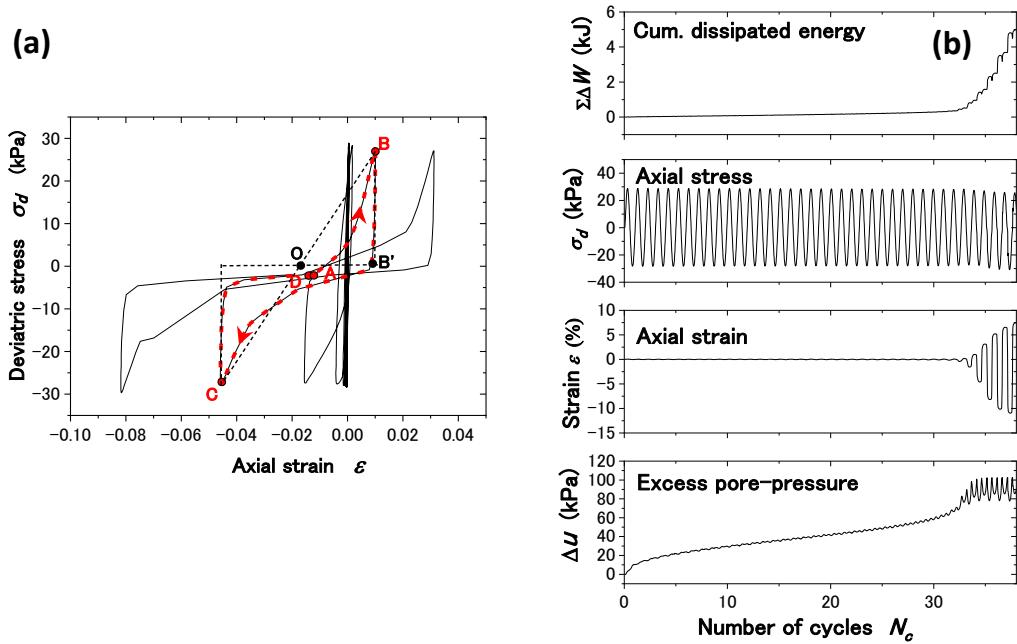
Figure 3. How to calculate cumulative dissipated energy in stress ~ strain hysteretic curve (a), and cyclic variations of cumulative dissipated energy, axial stress, strain, and pore-pressure (b), in cyclic triaxial tests.

In the top of Figure 3 (b), the cumulative dissipated energy per unit volume $\sum\Delta W$ calculated by Eq. (2) for the stress ~ strain curve in Figure 3 (a) is plotted versus the stress cycle N_c, together with axial stress σ_d, axial strain ε and excess pore-pressure Δu. The energy staying minimal in the earlier loading is followed by a drastic increase after the pore-pressure approaches $\sigma'_c = 98$ kPa at the onset of liquefaction. Note that the energy also keeps increasing steeply with increasing strain amplitude, though the pore pressure stops rising.
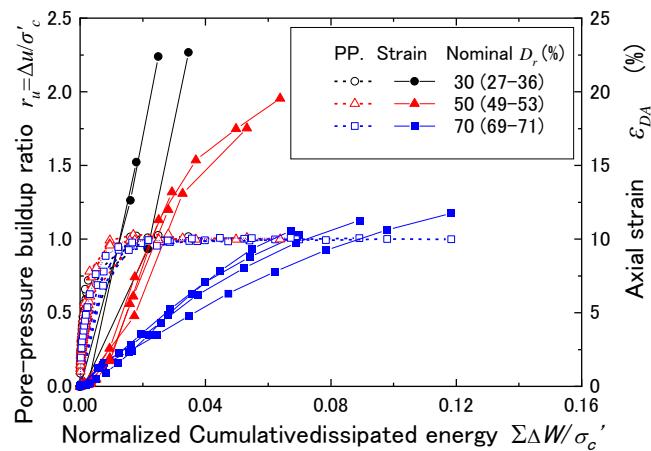
Figure 4. Relationships between normalized cumulative dissipated energy $\Sigma\Delta W/\sigma_c'$ and corresponding pore-pressure buildup ratio $r_u = \Delta u/\sigma_c'$ & DA axial strain ε_{DA} at each cycle.

Based on a series of similar tests, the maximum pore pressure in each cycle is plotted against corresponding cumulative dissipated energy together with double-amplitude axial strain ε_{DA} for each loading cycle in Figure 4 for sands of $F_c = 0$. Here, the pore pressure is normalized by the initial effective confining stress which is named the pore-pressure buildup ratio $r_u = \Delta u/\sigma'_c$, and the energy is also normalized as $\sum\Delta W/\sigma'_c$ in the horizontal axis. The plots are shown with different symbols for different nominal relative densities $D_r = 30, 50,$ and 70%. The pore-pressure buildup ratio r_u correlates well with the dissipated energy and becomes $r_u = 1.0$ at around $\sum\Delta W/\sigma'_c = 0.01 \sim 0.04$ with small D_r-dependent differences.

In good contrast, a dominant effect of D_r is clear for the strain amplitude ε_{DA} plotted in the right vertical axis versus the normalized energy $\sum\Delta W/\sigma'_c$, despite some data scatters caused by gaps between the targeted and actual D_r values. The induced strain ε_{DA} is almost in proportion to the normalized energy $\sum\Delta W/\sigma'_c$ for each relative density D_r up to a strain around $\varepsilon_{DA} = 10\%$. The strain development can thus be correlated consistently with dissipated energy not only up to the initial liquefaction ($\varepsilon_{DA} = 5\%$) but also beyond and serves as an indicator for the severity of liquefaction.
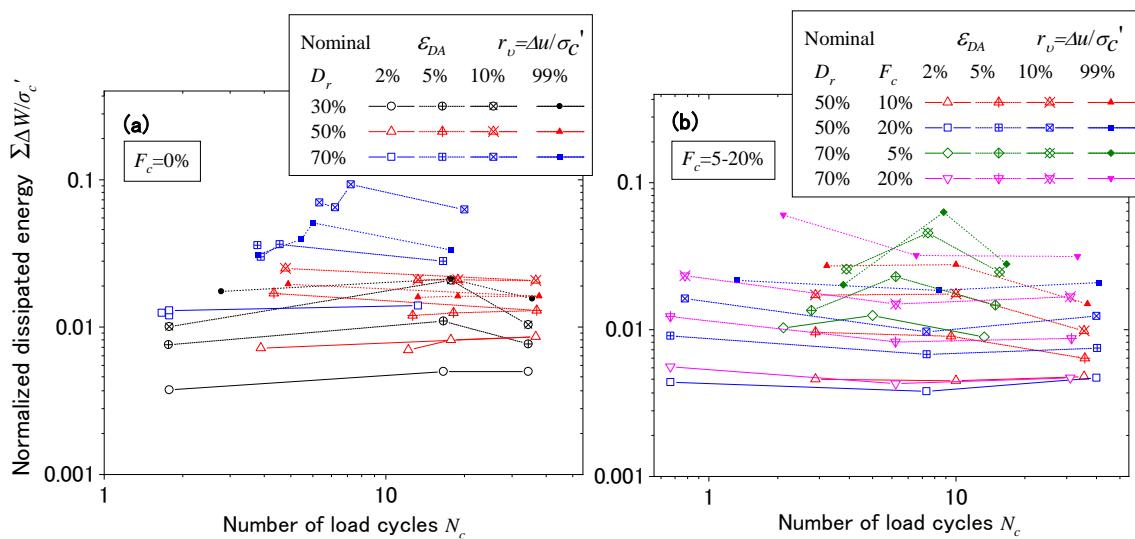
Figure 5. Normalized dissipated energy $\sum\Delta W/\sigma'_c$ for $\varepsilon_{DA} = 2, 5, 10\%$ and $r_u \approx 1.0$ plotted versus the number of loading cycles N_c in triaxial tests on reconstituted specimens.

In Figure 5, the normalized dissipated energies $\sum\Delta W/\sigma'_c$ to attain specific values of strain amplitudes, $\varepsilon_{DA} = 2, 5, 10\%$ as well as the pressure buildup ratio $r_u = \Delta u/\sigma'_c = 1.0$ are plotted in the vertical axis versus numbers of cycles N_c corresponding to achieve the specific values in the horizontal axis on the log-log chart. The plots in (a) are for clean sands ($F_c = 0$) with parametrically varying D_r, and those in (b) are for sands of parametrically changing fines content ($F_c = 5\sim20\%$) of nominal $D_r =$ 50% and 70%. There are groups of 2 to 4 data points with the same symbols corresponding to the same strain ε_{DA} or $r_u = 1.0$ achieved at different cycles N_c, which were read off from multiple tests carried out with different CSR for specimens of the same F_c and nominal D_r. The lines connecting the same symbols are essentially flat without consistent N_c-dependent up/down trends of $\sum\Delta W/\sigma'_c$, despite some different trends in higher strains ε_{DA} for dense sands.

The essentially flat lines seem to indicate that the dissipated energy $\sum\Delta W/\sigma'_c$ almost uniquely determines the induced strain amplitude ε_{DA} or pore-pressure buildup ratio r_u, no matter how many cycles N_c and how large the CSR-values are needed to attain those specific ε_{DA} or r_u. This further indicates that

a $CSR \sim N_c$ line corresponding to a particular strain ε_{DA} or r_u drawn in Figure 2, which normally serves as a basis for liquefaction potential evaluation in the SBM and is interpreted as the lines of equal damage in the fatigue theory (e.g., Annaki and Lee 1977 [32], Green and Terri 2005 [33]), which also represents the line of equal dissipated energy corresponding to specific conditions [18]. This observation paves the way for the EBM using the $CSR \sim N_c$ data in the SBM.

3.1.2. Dissipated energy versus CRR in isotropically consolidated triaxial tests

From the full-logarithmic $CSR \sim N_c$ chart in Figure 2, individual cyclic resistant ratios CRR for $N_c = 15$ (CRR_{15}) can be determined from individual plots of the same symbols using the constant b in Eq. (1) for $\varepsilon_{DA} = 2, 5, 10\%$, and $\Delta u/\sigma'_c \approx 1.0$. This can be done by drawing parallel lines of the same gradient b passing through individual plots to determine the corresponding $CRR_{Nc=15}$. Thus, the CRR_{15}-values determined are directly plotted versus corresponding dissipated energies $\sum \Delta W/\sigma'_c$ to develop the CRR_{15} versus $\sum \Delta W/\sigma'_c$ chart as shown in Figure 6. Despite some data scatters, the CRR_{15}–values for $\varepsilon_{DA} = 5\%$ (open circles) seem to be uniquely correlated with $\sum \Delta W/\sigma'_c$ despite widely varying relative densities and fines contents. The correlation may be approximated by a parabolic function Eq. (3) for $CRR_{20} \geq 0.1$; a practically meaningful condition in normal liquefaction problems with the determination coefficient $R^2 = 0.86$ [18].

$$\sum \Delta W \big/ \sigma'_c = 1.9 \cdot (CRR_{15} - 0.1)^2 + 0.008 \qquad (3)$$

Note that the $\sum \Delta W/\sigma'_c$ -values in the vertical axis correspond to the dissipated energies to attain the axial strain $\varepsilon_{DA} = 5\%$ regardless of CSR and N_c, while CRR_{15}–values in the horizontal axis represent the stress amplitudes at $N_c = 15$. For other strains $\varepsilon_{DA} = 2\%$ and 10%, similar curves with the vertical coordinate 0.4 times and twice that of 5%, respectively, are drawn in the chart. The curves show a fair fitting with the corresponding plots because the strain ε_{DA} is almost in proportion to the normalized energy $\sum \Delta W/\sigma'_c$ up to around $\varepsilon_{DA} = 10\%$ as already indicated in Figure 4.
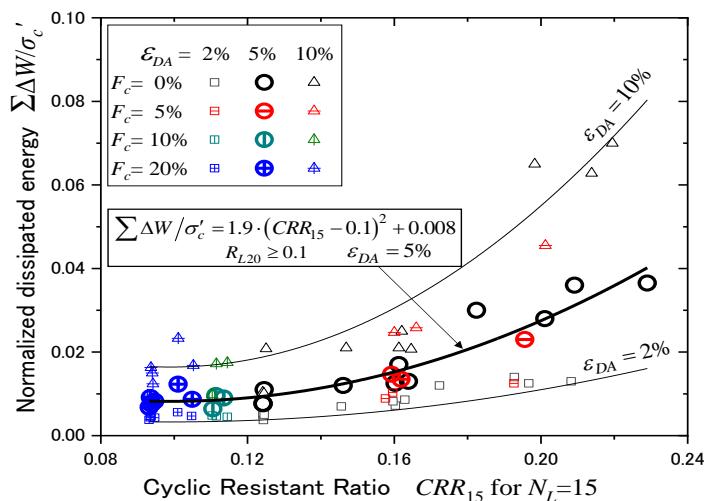

Figure 6. Normalized dissipated energy $\sum \Delta W/\sigma_c'$ versus CRR_{15} for $\varepsilon_{DA} = 2, 5,$ and 10% for sand specimens with different fines content.

3.2. Triaxial tests on intact specimens from in situ by harmonic loading

In most of the experimental studies conducted so far on the dissipated energy for liquefaction, reconstituted clean sands or those mixed with non-plastic fines have been used. Experimental data on intact soils recovered in situ wherein the energy for liquefaction was focused have rarely been available. Here, a series of cyclic undrained triaxial tests conducted on intact soils with various soil properties sampled from different sites are addressed to examine the uniqueness of the cumulative dissipated energy $\Sigma\Delta W$ in determining liquefaction behavior in terms of induced soil strain.

3.2.1. Intact specimens addressed

A systematic test program was implemented by the Public Works Research Institute (PWRI) of the Ministry of Land, Infrastructure and Transportation (MLIT) of the Japanese Government after the 2011 Tohoku earthquake ($M_w = 9.0$) in Japan to review the liquefaction damage in the eastern part of Japan (Sasaki et al. 2016 [34]). Eventually, 190 specimens tested from 49 intact soils sampled from alluvium and hydraulic/land-fills at different sites were used. Among them, softer soils were sampled by fixed-piston thin-wall samplers, while stiffer soils were sampled by rotary triple-tube samplers. The sampling holes were drilled near pilot borings wherein SPT blow-counts and P/S-wave velocities were measured.

Sample		CRR_{15}	a	b	F_c (%)	PI	SPT-N_1
S1	■ ——	0.153	0.325	−0.298	15−19	0	11.3
S2	□ ⋯⋯	0.206	1.721	−0.779	2−19	0	11.1
S3	◨ ⋯⋯	0.205	0.420	−0.259	4−12	0	3.2
S4	⊞ ⋯⋯	0.213	0.410	−0.246	3−37	0	2.7
S5	● ——	0.226	0.446	−0.249	7−43	0	4.4
S6	○ −−−	0.252	0.535	−0.277	44−52	5−7	3.9
S7	◓ −·−	0.285	0.364	−0.091	84−97	10−11	3.7
S8	⊕ ⋯⋯	0.312	0.422	−0.104	1−11	0	10.7
S9	▲ ——	0.334	0.698	−0.269	34−46	0−7	2.3
S10	△ −−−	0.327	0.506	−0.158	72−90	4−16	1.7
S11	▲ −−−	0.348	0.821	−0.308	6−17	0	10.2
S12	✦ −·−	0.357	0.585	−0.182	17−19	0	2.4
S13	▼ ——	0.346	0.497	−0.133	98−99	34−41	0.9
S14	▽ −−−	0.495	0.690	−0.121	99−100	36−50	0.0

Figure 7. Cyclic stress ratio versus number of cycles for 14 selected intact samples S1-S14 and their pertinent properties.

Stress-controlled undrained cyclic triaxial tests of intact specimens with a diameter of 5 cm and a height of 10 cm were carried out, where soil specimens were fully saturated and isotropically consolidated by in situ effective mean stresses and cyclically loaded in the undrained condition. Among the soil samples recovered by tube sampling at various depths of different sites comprising 51 specimens altogether, 14 of them named here as S1 ~ S14 were selected as of higher reliability. The samples were very variable even in the same sample tube in density, F_c, and PI (plasticity index) [34]. In each sample, 3 ~ 4 specimens were tested with different CSRs leading to different N_L. Those from

the same soil sample were assumed uniform, though actually, a certain degree of heterogeneity reflecting soil stratifications was inevitable.

In Figure 7, all the triaxial test results in terms of CSR versus the number of cycles N_c to attain $\varepsilon_{DA} = 5\%$ (corresponding to the initial liquefaction) are shown together with pertinent parameters of the 14 sample S1~S14 in the legend. Note that the soils are sandy, silty and clayey, and very variable with fines content $F_c = 0\sim100\%$, plasticity index $PI = 0\sim50$, and in situ SPT $N_1 = 1\sim11$. The N_1-values were calculated from SPT N-values conducted in pilot borings nearby using the formula $N_1 = 170N/(\sigma'_v + 70)$ where σ'_v = effective overburden in kPa. (Meyerhof 1957 [35]). The $CSR \sim N_c$ plots are approximated on a full-logarithmic diagram with the straight line by Eq. (1) with the constants a and b also listed in the legend. The liquefaction strengths are widely distributed and the gradients of the lines, b, tend to decrease with increasing CRR_{15} except for a few exceptions (S2, S9, S11).

3.2.2. Hysteresis curves and dissipated energy of intact soils

On the left in Figure 8 (a)–(d), four hysteresis curves of cyclic axial stress σ_d versus axial strain ε are exemplified (S3, S4, S8, S10 out of S1 ~ S14), individually. At first glance, one may notice that, in most, the cyclic strain tends to develop larger in the extension side (left) than in the compression. This trend is generally observed in triaxial cyclic loading tests. It may presumably be attributed to the asymmetry in the three-dimensional stress condition inherent to cyclic triaxial tests between compression loading (one-axis vertical compression and two-axes horizontal extension) and tension loading (vice versa), as well as to anisotropy in the soil fabric.

The cumulative dissipated energies per unit area $\Sigma\Delta W$ were calculated from the axial stress σ_d versus strain ε curves using Eq. (2) and nondimensionalized by initial effective confining stresses $\Sigma\Delta W/\sigma'_c$ in the same way as the reconstituted specimens. In the ε_{DA} versus $\Sigma\Delta W/\sigma'_c$ correlations individually shown on the right of Figure 8 (a)–(d), the energy dissipated to attain a given strain amplitude tends to be considerably larger as the CRR of the sample becomes greater from S2 to S10. In S8 of $CRR = 0.303$, for instance, about 10 times difference in energy can occur among the 3 specimens to attain the same strain $\varepsilon_{DA} = 5\%$. Also pointed out is that the ε_{DA}-value is not uniquely correlated with the energy $\Sigma\Delta W/\sigma'_c$ for larger ε_{DA} in particular, while the uniqueness tends to hold better for soils with lower CRR such as S4 of $CRR_{15} = 0.204$. Thus, the uniqueness of energy in determining liquefaction-induced strain, recognized in Figure 5 for reconstituted specimens, does not hold in these triaxial tests on intact samples for larger strains except for the low CRR soils [20].
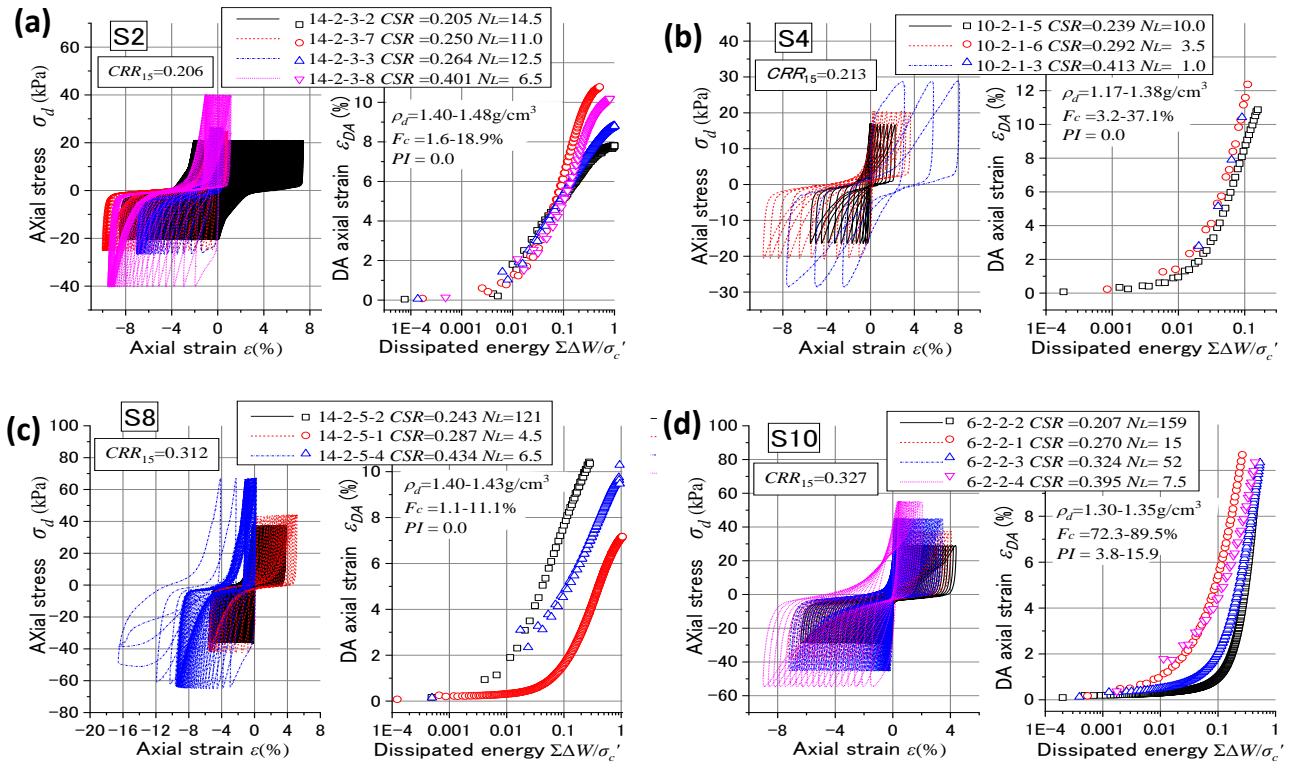
Figure 8. Hysteresis curves of cyclic axial stress σ_d versus axial strain ε on the left together with corresponding plots of double amplitude axial strain ε_{DA} in a log scale versus dissipated energy $\Sigma\Delta W/\sigma'_c$ on the right (S3, S4, S8, S10).

In Figure 9 (a) to (d), the number of cycles N_L to attain reference DA strains ε_{DA} = 2, 5, and 10% are plotted in the horizontal log axis versus corresponding dissipated energies $\Sigma\Delta W/\sigma'_c$ in the vertical axis. The plots represented by different symbols for different samples and reference strains are connected with dashed lines for easy identification of grouping. In (a) the non-cohesive soils S1~S6 of lower CRR ($0.153 \le CRR_{15} \le 0.252$), the dissipated energies $\Sigma\Delta W/\sigma'_c$ are relatively small and almost unchanged along increasing N_L. In contrast, the non-cohesive soils S7~S12 ($0.285 \le CRR_{15} \le 0.357$) in (b), $\Sigma\Delta W/\sigma'_c$ tends to increase with increasing N_L for larger reference strains in particular despite some data scatters. The same trend as (b) can be observed more clearly in (c) the cohesive soils of S13~S14 ($0.346 \le CRR_{15} \le 0.495$).
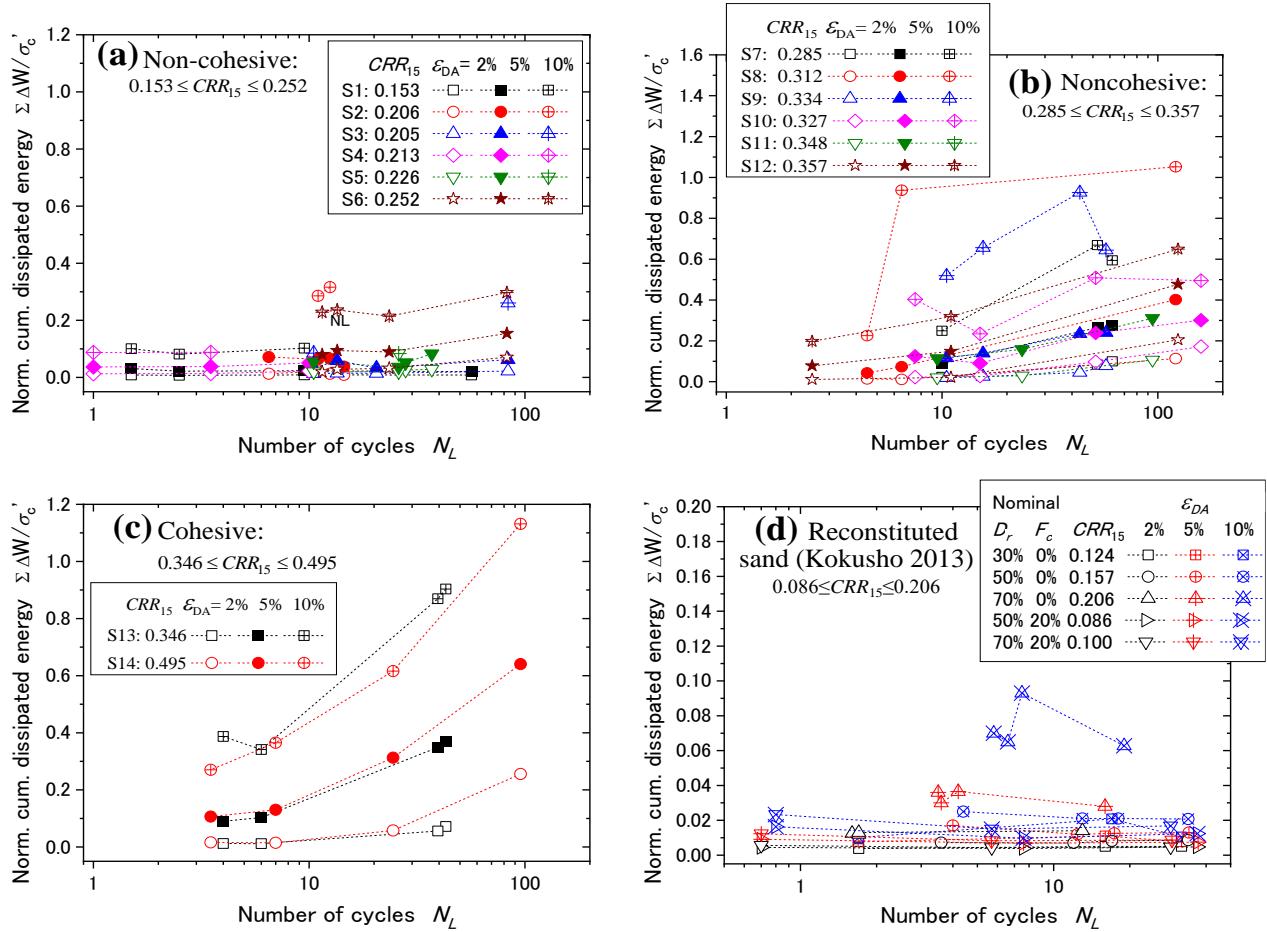
Figure 9. Normalized dissipated energy $\Sigma\Delta W/\sigma'_c$ versus number of cycles N_L achieving DA strains $\varepsilon_D = 2, 5, 10\%$ for intact soils (a), (b), (c) and reconstituted sand (d).

Apart from these intact samples, Figure 9 (d) shows cyclic triaxial test results on reconstituted Futtsu sand of $D_r \approx 30, 50, 70\%$, and $F_c = 0\%$ or 20% with $CRR_{15} = 0.086{\sim}0.206$, already addressed in Figure 5. Their dissipated energies $\Sigma\Delta W/\sigma'_c$ are smaller than the intact samples in Figure 9 (a), and almost unchanged with increasing N_L, presumably reflecting the absence of the aging effect in the reconstituted samples.

In Figure 10, CSR values are plotted versus corresponding dissipated energies $\Sigma\Delta W/\sigma'_c$ in full logarithmic diagrams to attain the reference DA strains $\varepsilon_{DA} = 2, 5,$ and 10%. In the non-cohesive soils of lower CRR, S1~S6 in (a), the energies are mostly constant and independent of CSR despite large data scatters. In contrast, the non-cohesive soils of higher CRR, S7~S12 in (b), exhibit decreasing trends of $\Sigma\Delta W/\sigma'_c$ with increasing CSR (except abnormal S8). In the cohesive soils, S13~S14 in (c), the decreasing trend of $\Sigma\Delta W/\sigma'_c$ with increasing CSR is more visible.
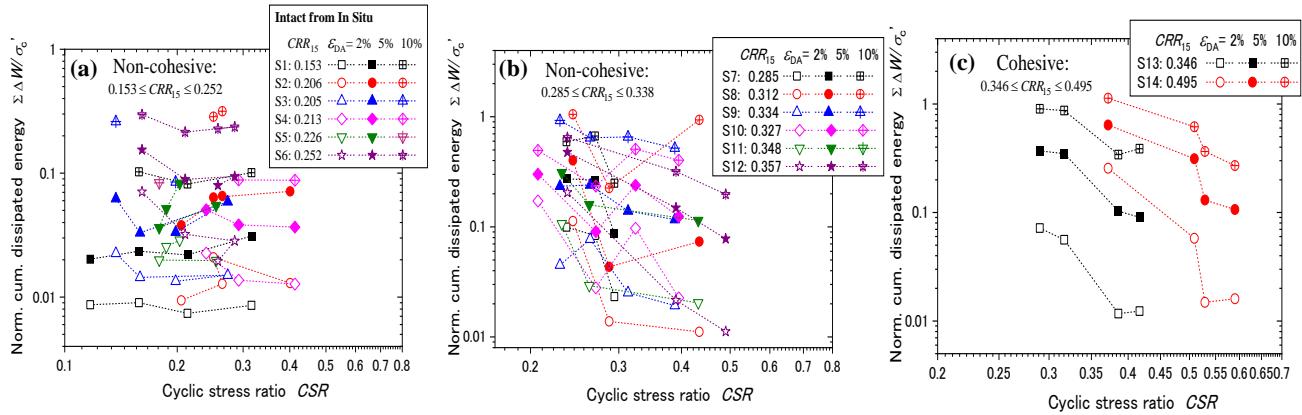
Figure 10. Normalized dissipated energy $\Sigma\Delta W/\sigma'_c$ versus *CSR* for intact samples of different CRR_{15} in (a), (b), (c).

From the test results in Figures 9 and 10, it may be inferred that intact non-cohesive soils of low *CRR* in (a) are similar to reconstituted sands, wherein the energy $\Sigma\Delta W/\sigma'_c$ almost uniquely determines induced strain with no regard to the number of cycles N_L or *CSR*. However, intact non-cohesive/cohesive soils of higher *CRR* which presumably reflect stronger aging appear to lose the uniqueness of energy in liquefaction behavior. Thus, the N_L/*CSR*-dependency of dissipated energy for liquefaction seems more conspicuous for intact soils of higher *CRR* in cyclic triaxial tests [20].
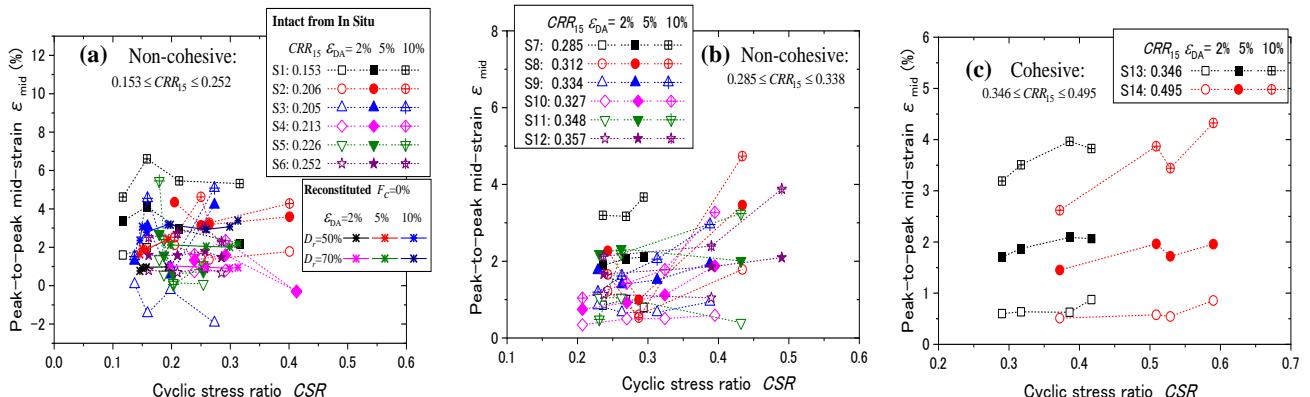

Figure 11. *CSR* versus mid-strain ε_{mid} in triaxial tests on intact soils of different CRR_{15} in (a), (b), and (c).

In order to quantify the extension strain bias thus observed, peak-to-peak mid-strain $\varepsilon_{mid} = (\varepsilon_{max} + \varepsilon_{min})/2$ is calculated from the maximum and minimum strains in each loading cycle, ε_{max} and ε_{min}, respectively, wherein the extension strain is to be positive. The ε_{mid}-values for DA strains $\varepsilon_{DA} = 2, 5, 10\%$ in the triaxial tests are plotted versus corresponding *CSR* in Figure 11 with different symbols. Note that the plots are overwhelmingly on the positive side of ε_{mid}, indicating that almost all cyclically induced strains are biased on the extension side. The ε_{mid}-values are widely varied for the non-cohesive lower *CRR* soils in (a) presumably reflecting variability of in situ natural soils, but they show no meaningful correlations with *CSR*. For the reconstituted Futtsu sand of $D_r \approx 50$ & 70% and $F_c = 0\%$

plotted on the same chart, and the ε_{mid}-values are also positive and essentially flat versus increasing CSR. In the non-cohesive higher CRR soils in (b), however, ε_{mid} tends to increase with increasing CSR for higher strains ε_{DA}, and the same trends are more clearly recognized in the cohesive soils of higher CRR in (c). Thus, the strain bias on the extension side seems intrinsic in triaxial tests in general, which tends to be more pronounced with increasing CSR for intact in situ soils of higher CRR with a larger DA strain in particular, while this trend is not so evident in reconstituted sands.

In Figure 12 (a)–(c), the dissipated energy $\Sigma\Delta W/\sigma'_c$ is directly plotted versus the peak-to-peak mid-strain ε_{mid} for the three groups of samples in terms of their averages for reference DA strains $\varepsilon_{DA} = 2, 5, 10\%$ with the large plots connected with solid lines, while the smaller plots with dashed lines are individual data with different CSRs corresponding to individual ε_{DA}-values. The energy $\Sigma\Delta W/\sigma'_c$ tends to increase with increasing ε_{mid} if the average values are concerned, though $\Sigma\Delta W/\sigma'_c$ for the same ε_{DA} is also dependent on CSR. That dependency is small for the soils of low CRR in (a) though getting stronger with increasing CRR in (b) and (c) as already addressed. Thus, the strain bias in extension is one of the major causes of the apparent non-uniqueness of energy specific in the triaxial stress system [20].
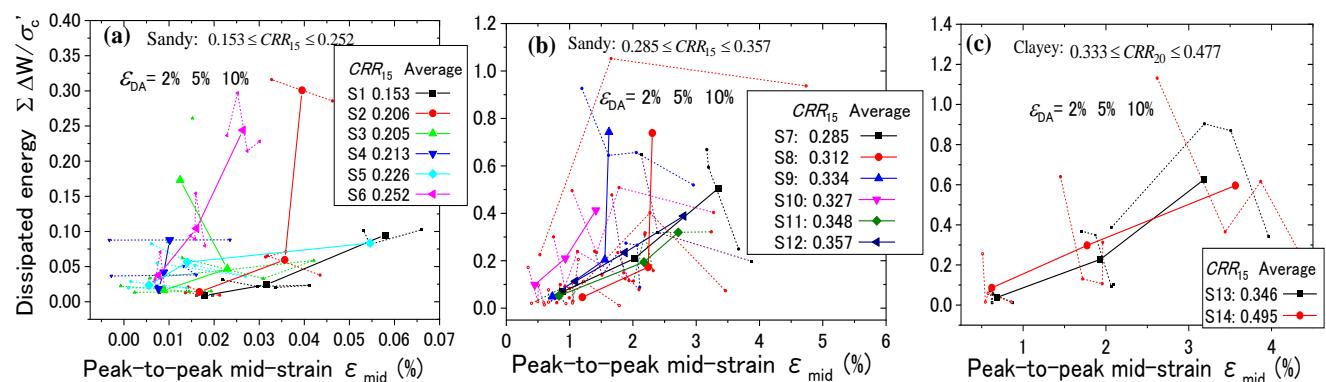
Figure 12. Dissipated energy versus mid-strain ε_{mid} for intact soils of different CRR_{15} in (a), (b), (c).

Unlike cyclic triaxial tests, however, soil layers in situ are cyclically sheared left and right during earthquakes by SH waves on a horizontal plane, wherein no such three-dimensional stress asymmetry in compression/extension exists. The best way to reproduce the in situ stress system in the laboratory is (hollow cylindrical torsional) simple shear tests.

The above experimental finding regarding triaxial tests may have a significant impact not only on the evaluation of liquefaction energy capacity but also on numerical liquefaction analyses by effective stresses, wherein soil constitutive models are calibrated to $CSR{\sim}N_c$ correlations often obtained by laboratory element tests. Considering the significant effect of strain bias in the stress versus strain hysteretic relationship, it is recommended to use simple shear tests rather than triaxial tests for better reliability of the analyses.

3.2.3. Dissipated energy versus CRR correlation for intact soils

Considering that CRR used in SBM is normally defined as CSR at $N_L = 15$, the dissipated energy corresponding to that particular CSR or N_L may be focused and correlated with CRR. For that goal, $\Sigma\Delta W/\sigma'_c$ versus CSR plots of individual samples for $\varepsilon_{DA} = 5\%$ (corresponding to the initial liquefaction)

in triaxial tests depicted in Figure 10 are approximated here by a straight line on the log-log diagram as conceptually illustrated in Figure 13 (a) and formulated by a power function of Eq. (4) [20].

$$\left(\sum \Delta W / \sigma_c'\right)_{\varepsilon_{DA}=5\%} = \alpha \cdot \left(CSR / CRR_{15}\right)^{-\beta} \tag{4}$$
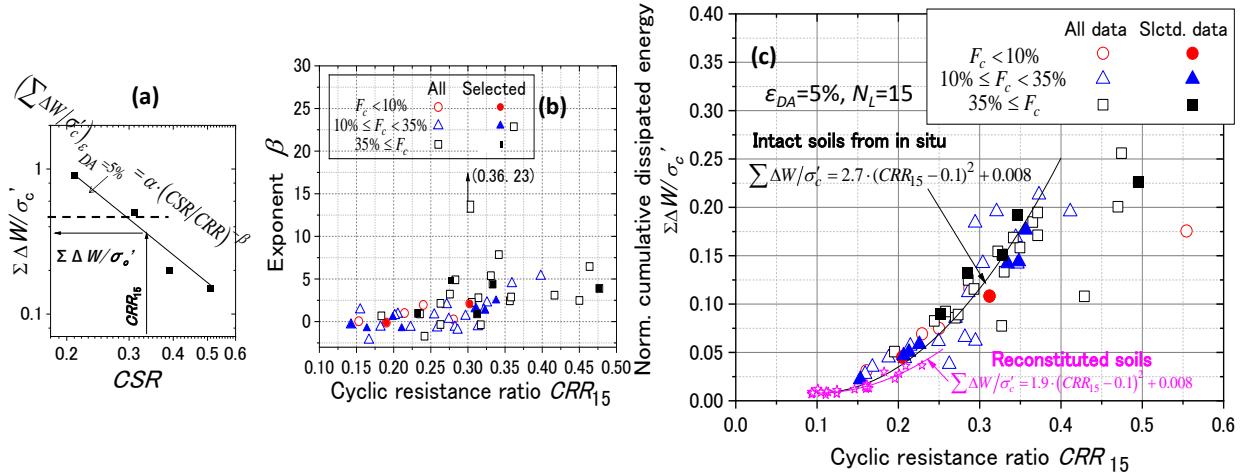
Figure 13. How to modify dissipated energy corresponding to *CRR* from triaxial test data: (a) Schematic function of dissipated energy $\Sigma \Delta W / \sigma_c'$ versus *CSR* correlation, (b) Exponent β versus CRR_{15} calculated for intact samples, and (c) Dissipated energy $\Sigma \Delta W / \sigma_c'$ versus CRR_{15}.

Here, CRR_{15} is the *CSR*-value in isotropically consolidated cyclic triaxial tests at $N_L = 15$ as normally accepted in the SBM liquefaction evaluation, wherein a constant α is equal to $\Sigma \Delta W / \sigma_c'$ when $CSR = CRR_{15}$, and $-\beta$ is a negative gradient of the line. If the energy were uniquely determined irrespective of N_L or *CSR*, the dashed flat line with $\beta = 0$ in Figure 13 (a) would be obtained. Thus, it seems practically meaningful to represent the dissipated energies corresponding to various *CSR*-values in cyclic triaxial tests by the energy for $CRR = CSR$ at $N_L = 15$ by using Eq. (4). It could be $N_L = 20$ or other values in place of $N_L = 15$, whichever possible in engineering practice, as long as the corresponding dissipated energy $\Sigma \Delta W / \sigma_c'$ is postulated to uniquely determine the strain amplitude for liquefaction irrespective of *CSR* or N_L.

Figure 13 (b) depicts the β-values in Eq. (4) plotted versus CRR_{15} for all the 49 intact samples or the 14 selected samples with open or closed plots, respectively, where the symbols are grouped by stepwise F_c-values. For *CRR* around 0.25 or smaller, β is nearly zero, indicating in Eq. (4) that the energy for liquefaction can be uniquely determined independent of N_L or *CSR* as can be seen in Figures 9(a) and 10(a). With increasing *CRR*, β tends to increase from nearly zero to around 5, indicating that the non-uniqueness of energy or dependency on N_L or *CSR* in cyclic triaxial tests is pronounced as demonstrated in Figures 9 and 10.

The α-values, identical to the dissipated energy $(\sum \Delta W / \sigma_c')_{\varepsilon DA = 5\%}$ for $CSR = CRR$ in Eq. (4), are calculated from Figure 10 and plotted versus CRR_{15} in Figure 13 (c). The open and closed dots represent the global and selected data, respectively, and different symbols represent different stepwise F_c-values, again.

For the selected data of $CRR < 0.4$, a good correlation can be obtained between CRR_{15} and the dissipated energy $\Sigma\Delta W/\sigma'_c$ to attain $\varepsilon_{DA} = 5\%$ (the initial liquefaction) as;

$$\sum \Delta W \big/ \sigma'_c = 2.7 \cdot \left(CRR_{15} - 0.1\right)^2 + 0.008 \qquad (5)$$

If CRR_{20} for $N_L = 20$ is chosen instead of 15 in SBM such as in the road-bridge design code in Japan, it becomes;

$$\sum \Delta W \big/ \sigma'_c = 3.5 \cdot \left(CRR_{20} - 0.1\right)^2 + 0.008 \qquad (6)$$

The determination coefficient for both equations is $R^2 = 0.92$ [20].

Remarkably, the liquefaction strength CRR used in SBM is almost uniquely correlated with the energy $\Sigma\Delta W/\sigma'_c$ despite the considerable variations in densities, fines contents, plasticity indices, and ages of in situ soils. Star symbols superposed in Figure 13 (c) are the cyclic triaxial test results of the reconstituted Futtsu sand already addressed in Figure 6, which also showed a unique relationship of Eq. (3) between the energy and CRR_{15} for the initial liquefaction ($\varepsilon_{DA} = 5\%$). Note that the close symbols of the selected data from the intact samples are essentially compatible with the star symbols, though the absolute energies are slightly larger presumably due to the aging effect of the intact soils.

Thus, the widely varied $\Sigma\Delta W/\sigma'_c$ versus CSR plots in Figure 10 obtained at different CSR-values in triaxial tests on intact soils from in situ have yielded a well-correlated $\Sigma\Delta W/\sigma'_c$ versus CRR_{15} plots as shown in Figure 13 (c). Hence, Eqs. (5) or (6) may be conveniently used to evaluate the energy capacity $\Sigma\Delta W/\sigma'_c$ for EBM from CRR to be determined in SBM from in situ penetration tests.

3.3. Torsional shear tests by harmonic loading

As shown above, the triaxial tests despite their good access from practical engineers have intrinsic difficulties in replicating simple shear conditions for evaluating liquefaction-induced dissipated energy. Figure 14 exemplifies stress-strain hysteresis curves of reconstituted clean sands by the torsional simple shear tests of (a) Futtsu sand of $D_r = 45\%$, and (b) Toyoura sand of $D_r = 80\%$, to compare with (c) the triaxial test result on reconstituted Futtsu sand of $D_r = 51\%$. In the simple shear tests, shear strain develops almost symmetrically, whereas, in the triaxial test, the strain tends to be biased on the extension side with increasing numbers of cycles even in medium-density reconstituted sands.
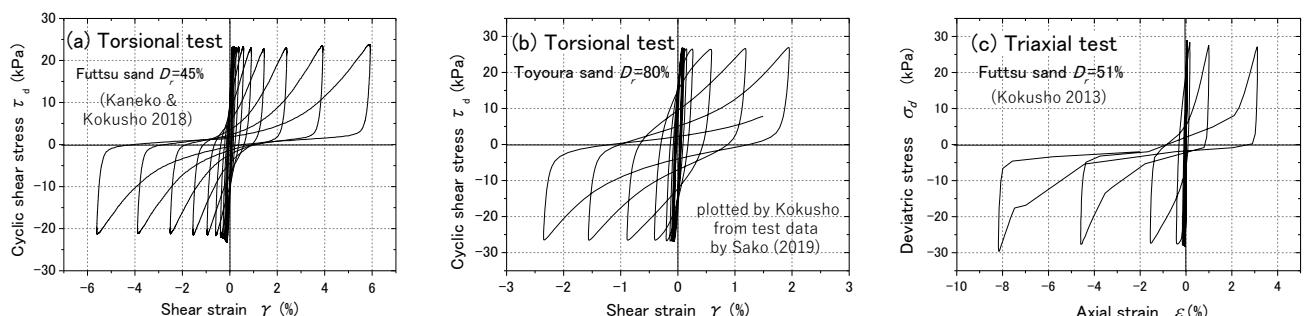

Figure 14. Stress-strain hysteresis exemplified for torsional simple shear tests (a), (b) compared with triaxial tests (c).

In the following, typical torsional undrained simple shear test results on reconstituted samples are addressed to examine the uniqueness of energy [19]. Harmonic and irregular cyclic stresses are given to the specimens without and with non-plastic fines to correlate excess pore pressure and induced strain with the dissipated energy. Effects of cyclic stress ratio *CSR*, number of cycles N_c, and wave irregularity on the energy-dependent strain evaluation are particularly focused.

The specimen size was $r_i = 30$ mm and $r_o = 50$ mm in inner and outer radius, respectively, and *H* = 100 mm in height. The Futtsu beach sand was used with non-plastic fines parametrically changing $F_c = 0$ to 30%. The test specimens were prepared by moist tamping to target relative densities, $D_r = 30$ and 50%. The specimens were saturated and isotropically consolidated by effective confining stress $\sigma_c' = 98$ kPa in most cases, or 48 or 196 kPa in some other cases and cyclically sheared by torsional stress τ_d. The cyclic stress τ_d was either the harmonic motion of frequency 0.1 Hz or irregular seismic motion with its time scale elongated 10 times.

Following the SBM practice, Figure 15 shows cyclic stress ratios $CSR = \tau_d/\sigma_c'$ for $\gamma_{DA} = 7.5\%$ (the initial liquefaction corresponding to axial strain $\varepsilon_{DA} = 5\%$ in triaxial tests) versus the number of cycles N_c on the log-log chart for all the torsional shear tests on reconstituted Futtsu sand specimens; (a) $D_r \approx 50\%$, $F_c = 0–30\%$, $\sigma'c = 49, 98, 196$ kPa and (b) $D_r \approx 30\%$, $F_c = 0\%$, $\sigma'c = 49, 98, 196$ kPa. Then, the plots are approximated by straight lines drawn after the empirical formula Eq. (1) with constants *a* and *b* regressed from the plots. Note that the plots are aligned almost linearly, and increasing F_c tends to reduce *CSR* considerably under the same D_r, while the effective confining stress seems to have only a minor effect.
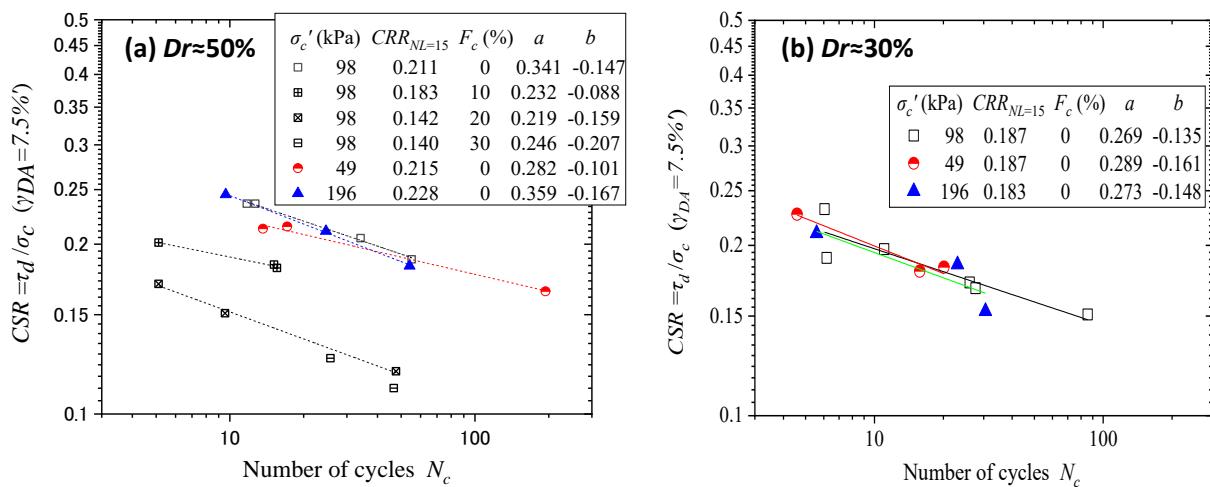
Figure 15. *CSR* versus N_c plots by undrained torsional simple shear tests on sands: (a) $D_r \approx 50\%$ ($\sigma_c' = 49, 98, 196$ kPa, $F_c = 0–30\%$) and (b) $D_r \approx 30\%$ ($\sigma_c' = 49, 98, 196$ kPa, $F_c = 0\%$).

3.3.1. Dissipated energy by harmonic loading

Figure 16 (a) and (b) exemplify the stress τ_d versus strain γ relationship or effective stress path (τ_d versus $p' = \sigma_c' - \Delta u$), respectively, for clean sand of $D_r = 45\%$ and $F_c = 0\%$ sheared by $CSR = \tau_d/\sigma_c' = 0.236$ in the effective confining stress $\sigma_c' = 98$ kPa. Dissipated energy in the cycle ABCDEFGHA′ in (a) can be calculated as;

$$\Delta W = \sum_{sa} \tau \Delta \gamma \approx \oint \tau d\gamma \tag{7}$$

where $\sum_{sa}$ stands for the summation of sliced areas such as PQQ′P′ for a strain increment $\Delta \gamma$, and $\oint$ for the integral in terms of shear strain γ in a single loading cycle. Obviously, the increment of dissipated energy in the sliced *Area* (PQQ'P') can be automatically calculated in Eq. (7) because $\tau \Delta \gamma$ alternates signs plus/minus between *Area* (PQRS) and *Area* (P'Q'RS) for increasing and decreasing strains, respectively.

The cumulative dissipated energy to a *k*-th cycle $\sum \Delta W$ is obtained as the summation of ΔW_k or expressed eventually as a seamless integral from the 1st to the arbitrary cycle as;

$$\sum_k \Delta W_k = \sum_k \left(\oint \tau d\gamma \right)_k = \int \tau d\gamma \tag{8}$$

Eq. (8) is valid not only for harmonic waves but also for irregular motions of variable amplitudes.
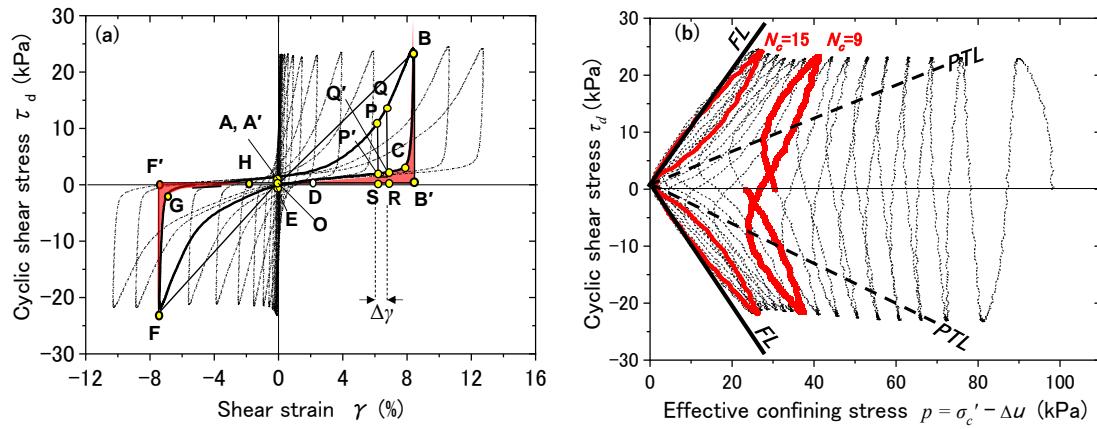

Figure 16. Typical torsional simple shear test results of $D_r \approx 45\%$, $F_c = 0\%$, $CSR = 0.236$, $\Delta u/\sigma_{c0}' = 98$ kPa: (a) Stress versus strain, and (b) Effective stress path.

Figure 17 (a) exemplifies typical time histories of (i) cyclic shear stress τ_d, (ii) excess pore-pressure normalized by effective confining stress $\Delta u/\sigma'_c$, (iii) shear strain γ, (iv) normalized cumulative dissipated energy $\sum \Delta W/\sigma'_c$, (v) axial stress σ_a, and (vi) axial strain ε_a. The axial stress and strain in the hollow cylindrical specimen tend to change slightly after the initial liquefaction as the specimen softens, though the associated energy is negligibly small. $\sum \Delta W/\sigma'_c$ increases its gradient with N_c when the initial liquefaction for $\gamma_{DA} = 7.5\%$ occurs at $N_L = N_c = 12.7$ in this case.

Figure 17 (b) shows typical variations of excess pore-pressure ratio $\Delta u/\sigma'_c$ and shear strain γ versus normalized cumulative dissipated energy $\sum \Delta W/\sigma'_c$ exhibited in the same test as (a). Larger close symbols in the chart represent pore-pressure buildup ratios $r_u = (\Delta u/\sigma'_c)_{\text{peak}}$ at the end of the individual stress cycles, while larger open symbols are double-amplitude shear strains γ_{DA}, peak to peak, in individual cycles. The r_u-value correlates with the dissipated energy in an asymptotic curve with its maximum $r_u \approx 1.0$ for $\sum \Delta W/\sigma'_c \approx 0.03$ at $N_c \approx 13$, corresponding to double-amplitude shear strains $\gamma_{DA} = 7.5\%$ for the initial liquefaction.
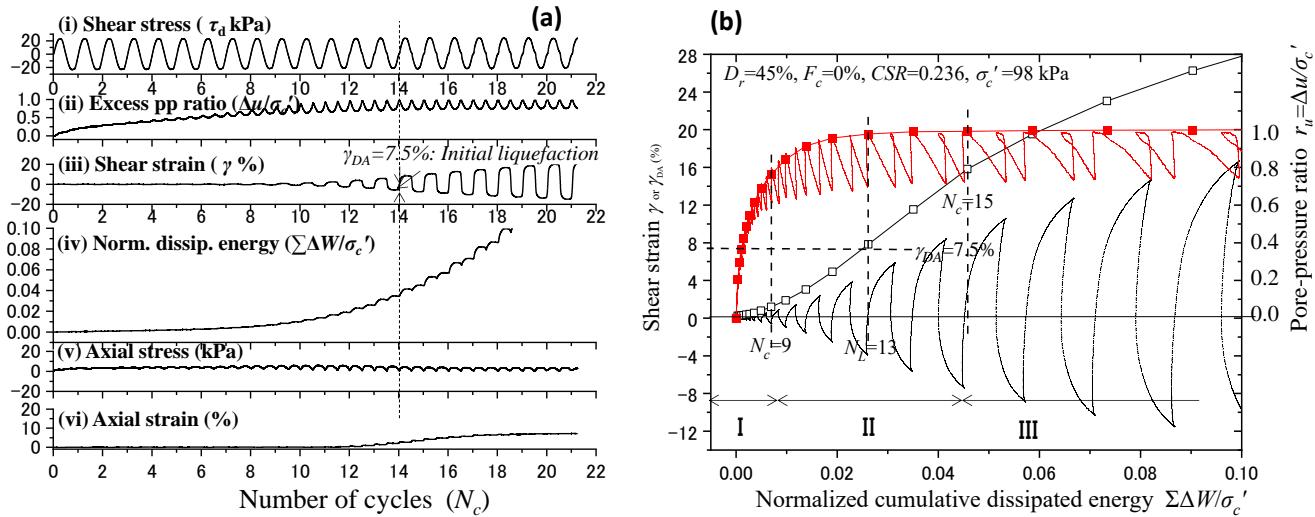
Figure 17. Typical torsional simple shear test result ($D_r = 45\%$, $F_c = 0\%$, $CSR = 0.236$, σ_c' = 98 kPa): (a) Time histories of stresses, pore-pressure, strains, dissipated energy, and (b) Normalized cumulative dissipated energy $\sum \Delta W / \sigma_c'$ versus shear strain & pore pressure buildup ratio r_u.

The γ_{DA} versus $\sum \Delta W / \sigma_c'$ curve changes its gradient at two inflection points, though it is not so strongly nonlinear. In this example, the first inflection occurs at $\sum \Delta W / \sigma_c' \approx 0.01$ around $N_c = 9$th cycle when the pore pressure starts fluctuating up/down due to cyclic mobility. In the $\tau_d \sim p'$ diagram of Figure 16 (b), the effective stress path around there is in a thick solid curve which is positioned about half in the dilative zone crossing the phase transformation line (PTL) (Ishihara et al. 1975 [36]). Moreover, in the same diagram, we observe that the second inflection appears at around N_c=15th cycle where the effective stress path moves up and down along the failure line (FL) shown with another thick curve through the origin. Thus, a γ_{DA} versus $\sum \Delta W / \sigma_c'$ curve in general may be divided into the next three sections. Section I: From the start to the 1st inflection point, where the effective stress path is contractive in cyclic loading with low strain versus energy gradient. Section II: From the 1st to 2nd inflection point, where the effective stress path is highly affected by PTL; semi-dilative in loading versus contractive in unloading, with higher strain versus energy gradient. Section III: The effective stress path moves along the failure line, exhibiting again a low strain versus an energy gradient.

Similarly, the correlations of pore-pressure ratio r_u and double-amplitude strain γ_{DA} are plotted versus dissipated energy $\sum \Delta W / \sigma_c'$ in Figure 18 (a) and (b), respectively, for clean sands of not only $D_r \approx 50\%$ (closed symbols) but also $D_r \approx 30\%$ (open symbols) both tested under $\sigma_c' = 98$ kPa. The r_u-value is almost uniquely correlated with $\sum \Delta W / \sigma_c'$ despite largely diverted CSR or N_L-values. The pressure buildup for $D_r \approx 30\%$ tends to occur slightly faster and attains $r_u = 1.0$ (the initial liquefaction) at lower dissipated energy than that for $D_r \approx 50\%$ around $\sum \Delta W / \sigma_c'$ =0.02.

In the γ_{DA} versus $\sum \Delta W / \sigma_c'$ correlation of Figure 18 (b), the double-amplitude strain γ_{DA} is distinctively larger for $D_r \approx 30\%$ than $D_r \approx 50\%$, indicating a significant effect of D_r on the induced strain. Among the same D_r group, the dissipated energy looks almost uniquely correlated with γ_{DA} up to the initial liquefaction ($\gamma_{DA} = 7.5\%$) and beyond. In the correlations, the energy $\sum \Delta W / \sigma_c'$ at the 1st inflection point around 0.01 or less, tends to be larger with increasing N_L. Hence, the γ_{DA} versus $\sum \Delta W / \sigma_c'$ correlation may not be precisely unique presumably due to the inflection point mentioned above. Nevertheless, as shown later, the dissipated energy $\sum \Delta W / \sigma_c'$ achieving a given γ_{DA} -value for

harmonic waves is found to be almost uniquely determined independent of N_L or *CSR*, presumably because the N_L-dependent effects are not strong enough to overcome the data scatters.
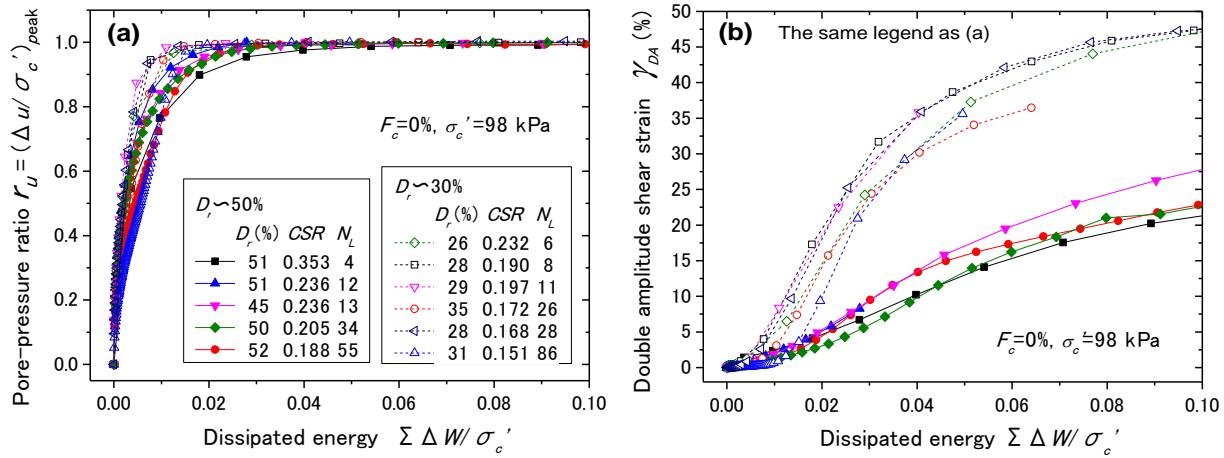
Figure 18. Torsional cyclic shear test results for Futtsu sand of $D_r \approx 50\%$ or 30%, $F_c = 0\%$ and $\sigma_c' = 98$ kPa: (a) Pore-pressure ratio r_u versus dissipated energy $\sum\Delta W/\sigma_c'$ and (b) Double-amplitude shear strain γ_{DA} versus dissipated energy $\sum\Delta W/\sigma_c'$.
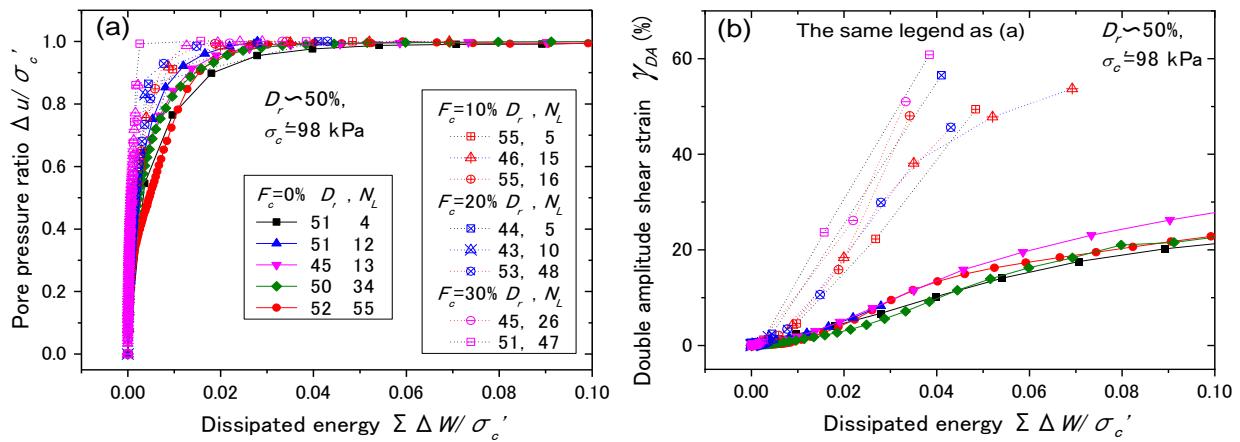
Figure 19. Torsional cyclic shear test results for sands of $D_r \approx 50\%$, $F_c = 0\sim30\%$ & $\sigma_c' = 98$ kPa: (a) Pore-pressure ratio r_u versus dissipated energy $\sum\Delta W/\sigma_c'$ and (b) Double-amplitude shear strain γ_{DA} versus dissipated energy $\sum\Delta W/\sigma_c'$.

Figure 19 shows similar correlations of r_u or γ_{DA} plotted versus $\sum\Delta W/\sigma_c'$ for $D_r \approx 50\%$ sands containing fines tested under $\sigma_c' = 98$ kPa. Plots of sands for fines content $F_c = 10\sim30\%$ are compared with solid plots for $F_c = 0$ already addressed in Figure 18. In Figure 19 (a), $\sum\Delta W/\sigma_c'$ is fairly well correlated with r_u in individual F_c-values, although the pressure buildup tends to occur earlier for the same energy as F_c increases from 0 to 30% and attain $r_u\approx1.0$ at smaller energy of $\sum\Delta W/\sigma_c' < 0.02$. In (b), the γ_{DA}-values for soils of $F_c = 10\sim30\%$ tend to grow larger for the same energy $\sum\Delta W/\sigma_c'$ than those for the clean sand $F_c = 0\%$, indicating a significant effect of F_c particularly due to the increase from $F_c = 0$ to 10%. Thus, the effect of fines content on the $\sum\Delta W/\sigma_c'$ versus γ_{DA} correlation is considerable even for the same D_r.

3.3.2.   Dissipated energy versus *CRR* in torsional shear tests

From the *CSR ~ Nc* chart for the SBM obtained by the torsional test on isotropically consolidated specimens in Figure 15, the cyclic resistant ratio CRR_{15} for γ_{DA} = 7.5% for N_c = 15 can be determined by Eq. (1) for each test specimen using the value *b* available in the legend. Thus, the determined CRR_{15}-values are directly correlated with corresponding dissipated energies $\sum\Delta W/\sigma'_c$ to construct CRR_{15} versus $\sum\Delta W/\sigma'_c$ correlations for γ_{DA} = 7.5% in Figure 20. The similar correlations analogously obtained for γ_{DA} = 3% and 15%, are also plotted in the chart. Despite that the plots included here widely differ in relative density $D_r \approx 30 \sim 50\%$, fines content $F_c = 0 \sim 30\%$ and confining stress= 49 ~ 198 kPa, the CRR_{15}-values for the strain level γ_{DA} = 7.5% plotted by the circles seem to be correlated fairly well with the dissipated energy $\sum\Delta W/\sigma'_c$ and can be approximated by a parabolic function;

$$\sum\Delta W/\sigma'_c = -0.00472 - 0.00143CRR_{15} + 0.582CRR_{15}^2 \tag{9}$$

for $CRR \geq 0.1$ or larger with the determination coefficient $R^2 = 0.79$.

A similar $\sum\Delta W/\sigma'_c \sim CRR$ approximation formula Eq.(3) previously obtained in the triaxial tests under σ'_c =98 kPa using the same reconstituted Futtsu sand of D_r = 30, 50, 70% for axial strain ε_{DA} = 5% (corresponding to γ_{DA} = 7.5% in shear strain) is overlaid with a dashed curve in Figure 20. Note that the dissipated energy in Eq.(3) is defined differently in the chart as 3/4 of that in Eq.(8), because the shear stress and strain in the simple shear stress condition are expressed as $\tau = \sigma/2$ and $\gamma = 3\varepsilon/2$ where σ and ε are the axial stress and strain in triaxial shear, respectively. Despite the significant differences in the test conditions, the solid curve in Eq. (9) looks similar to the dashed curve in Eq. (3).
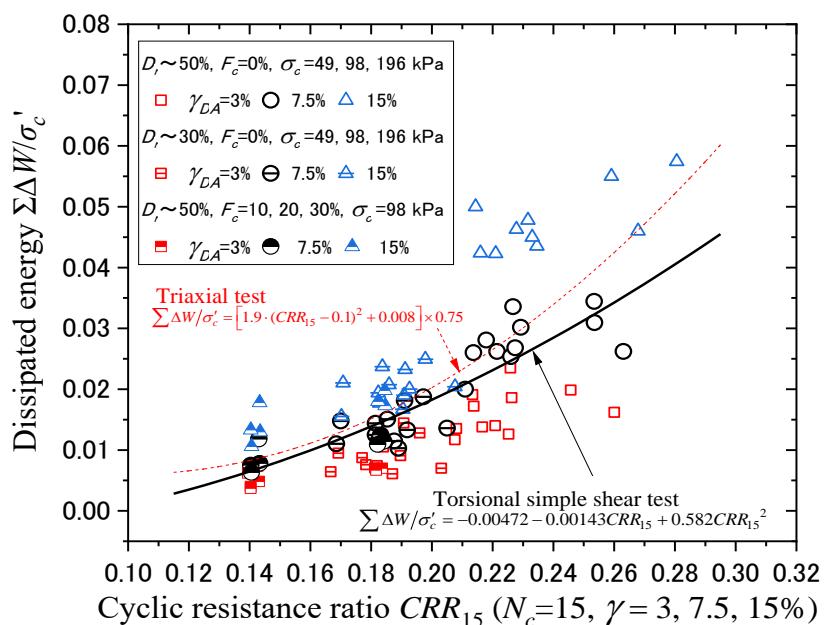
Figure 20. CRR_{15} (N_c = 15, γ_{DA} = 3, 7.5, 15%) plotted versus corresponding normalized dissipated energy $\sum\Delta W/\sigma'_c$ for sands of $D_r \approx 50\%$, F_c = 0~30%, σ_c' = 98 kPa in tortional simple shear tests.

3.3.3. Effect of confining stress on dissipated energy

Figure 21 shows the influence of effective confining stress changing stepwise, $\sigma'_c = 49$, 98, and 198 kPa, on the correlations of $\sum\Delta W/\sigma'_c$ versus ratio r_u in (a) or induced shear strain γ_{DA} in (b) for the sand of $D_r \approx 50\%$ and $F_c = 0\%$. The pressure ratio r_u for the same $\sum\Delta W/\sigma'_c$ -value tends to be lower with increasing σ'_c in (a) while a similar trend can be seen for the γ_{DA} versus $\sum\Delta W/\sigma'_c$ correlation in (b) only for smaller energy values despite larger data scatters.
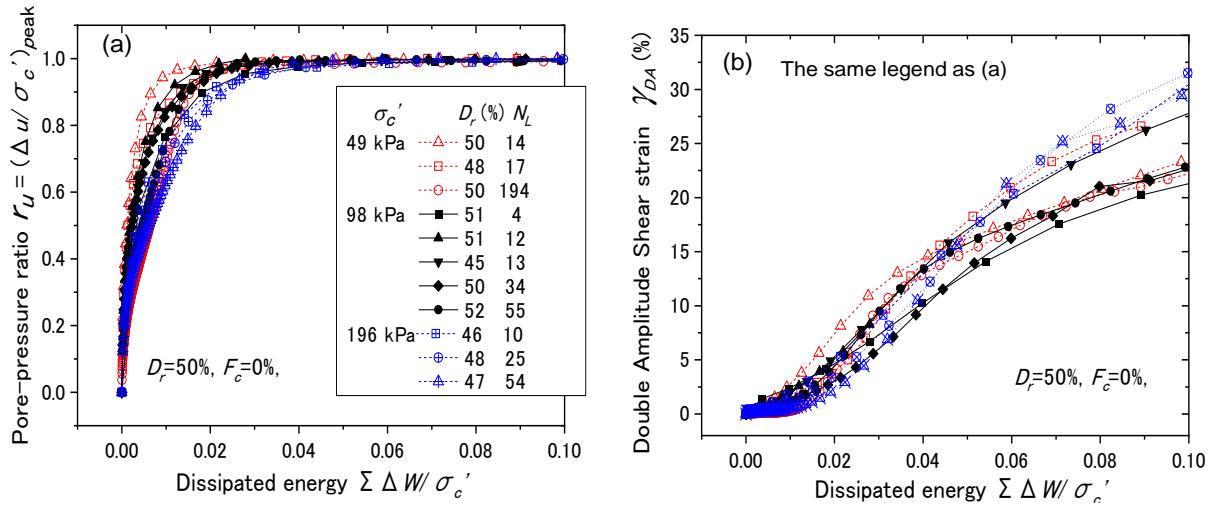
Figure 21. Torsional simple shear test results for sands of $D_r \approx 50\%$, $F_c = 0\%$ and $\sigma_c' = 49$, 98, 196 kPa: (a) Pore-pressure ratio r_u versus dissipated energy $\sum\Delta W/\sigma'_c$, and (b) Double-amplitude shear strain γ_{DA} versus dissipated energy $\sum\Delta W/\sigma'_c$.
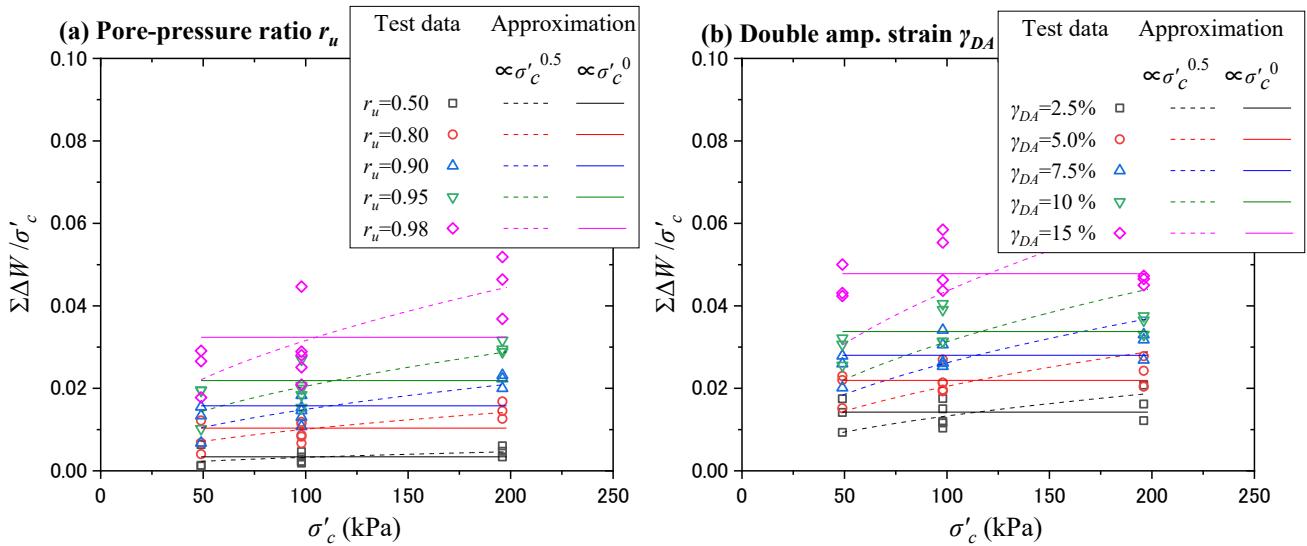
Figure 22. Effect of effective confining stress σ_c' on normalized dissipated energy $\sum\Delta W/\sigma'_c$ for sands of $D_r \approx 50\%$ and $\sigma_c' = 98$ kPa: (a) Pore-pressure ratio $r_u = 0.5\sim0.98$, (b) Double-amplitude shear strain $\gamma_{DA} = 2.5\sim15\%$.

In Figure 22, the energies normalized by confining stress, $\sum \Delta W/\sigma'_c$, to attain (a) stepwise r_u-values or (b) stepwise γ_{DA}-values are plotted versus the effective confining stresses for $\sigma'_c = 49$ to 196 kPa to examine how σ'_c impacts the $\sum \Delta W/\sigma'_c$-value. The inclined dashed lines and horizontal solid lines drawn there assume that $\sum \Delta W/\sigma'_c$ is either dependent on $(\sigma'_c)^{0.5}$ or independent of the confining stress $(\sigma'_c)^0$, respectively.

As for the effect of σ'_c on the dissipated energy, let us assume that a stress τ versus strain γ hysteresis loop of cyclically loaded sands is idealized by the hyperbolic model $f(\ )$ often employed in liquefaction analyses (e.g. Kokusho 2017) [37] as;

$$\tau = G_0 \gamma_r \frac{(\gamma/\gamma_r)}{1 + (\gamma/\gamma_r)} = G_0 \gamma_r f(\gamma/\gamma_r) \tag{10}$$

where G_0 = initial shear modulus, γ_r = reference strain for $G/G_0 = 0.5$. Then, the normalized cumulative dissipated energy is calculated as;

$$\sum \Delta W/\sigma'_c = \int \tau d\gamma/\sigma'_c = \frac{G_0 \gamma_r}{\sigma'_c} \int f(\gamma/\gamma_r) d\gamma = \frac{G_0 \gamma_r^2}{\sigma'_c} \int f(\gamma/\gamma_r) d(\gamma/\gamma_r) \tag{11}$$

Because G_0 and γ_r are dependent on the effective confining stress σ'_c as;

$$G_0 = G_0^* \times (\sigma'_c/p_0)^{0.5} \tag{12}$$

$$\gamma_r = \tau_f/G_0 = \sigma'_c \tan\phi \left/ \left(G_0^* \times (\sigma'_c/p_0)^{0.5} \right) \right. = \frac{(\sigma'_c/p_0)^{0.5}}{G_0^*/p_0} \tan\phi \tag{13}$$

where G_0^* = shear modulus under a unit pressure p_0, $\tau_f = \sigma'_c \tan\phi$ = ultimate shear strength, ϕ = internal friction angle, and p_0 = unit pressure. Then;

$$\sum \Delta W/\sigma'_c = \frac{G_0^* \times (\sigma'_c/p_0)^{0.5}}{\sigma'_c} \left[\frac{(\sigma'_c/p_0)^{0.5}}{G_0^*/p_0} \tan\phi \right]^2 \int f(\gamma/\gamma_r) d(\gamma/\gamma_r)$$
$$= \frac{\tan^2\phi}{G_0^*/p_0} \times (\sigma'_c/p_0)^{0.5} \int f(\gamma/\gamma_r) d(\gamma/\gamma_r) \tag{14}$$

It shows that the normalized cumulative dissipated energy $\sum \Delta W/\sigma'_c$ tends to increase proportionally to $(\sigma'_c/p_0)^{0.5}$, the square root of the confining stress.

From experimental observations shown in Figure 22 (a), the normalized energy $\sum \Delta W/\sigma'_c$ looks to be proportional to $(\sigma'_c)^{0.5}$ as in Eq. (14) in terms of pressure buildup r_u. However, in terms of induced strain γ_{DA} in (b), it seems more appropriate to assume that $\sum \Delta W/\sigma'_c$ is σ'_c-independent. In the latter case, the energy $\sum \Delta W/\sigma'_c$ can be normalized dimensionally and quantitatively. Then, the normalized dissipated energy in determining liquefaction-induced strain becomes almost independent of soil depth, to be beneficial for in situ liquefaction evaluations based on energy.

3.4. Torsional shear tests by irregular loading

3.4.1. Irregularity of input stress waves

A variety of earthquake motions A to F, covering intra-plate as well as plate-boundary earthquakes recorded in recent decades in Japan widely varied in terms of magnitudes (M_J = 6.8 to 9.0), hypocenter distance (R = 24~380 km), duration, and number of cycles, were used for the liquefaction tests as tabulated in Table 1. The undrained cyclic torsional shear tests were conducted twice using the same waves with different amplitudes on Futtsu sands of $D_r \approx 50\%$, $F_c = 0\%$ under initial isotropic effective confining stress $\sigma'_c = 98$ kPa [19].

Table 1. Six irregular stress waves A~F from recent devastating earthquake records, each testing twice by different amplitudes with their pertinent parameters and major results.

Stress wave		Earthquake & Recorded site	M_J JMA Earthq. Mag.	R (km) Hypoc. Dist.e	Max. stress ratio CSR_{max} τ_{max}/σ_c'	$N_{c\text{-}total}$ Total number of cycles $\tau_{d,DA}$ >5%	N_c for γ_{max} (only for DA strs. amp. > 5% of max. DA strs. Amp.)			Damage level for $b=-0.258$	D_r (%) Relative density of sand	Normalized dissipated energy $\Sigma\Delta W/\sigma_c'$		
							$\gamma_{max}=$ 3%	$\gamma_{max}=$ 7.5%	$\gamma_{max}=$ 15%			$\gamma_{max}=$ 3%	$\gamma_{max}=$ 7.5%	$\gamma_{max}=$ 15%
A	A-1	2007 Niigataken Chuetsu-oki EQ.	6.8	27	1.22	16	3.2	3.9	6,5	1.18	48	0.0105	0.0280	0.0621
	A-2	K-NET Kashiwazaki			0.57	7	4.2	5.3	x	1.42	44	0.0092	0.0277	x
B	B-1	1995 Kobe EQ. Port Island (PI) VA. GL. -0 m	7.2	24	0.83	11	6.7	7.5	9.4	1.61	49	0.0120	0.0316	0.0600
	B-2				0.76	11	3.5	4.5	7.9	1.56	42	0.0088	0.0273	0.0532
C	C-1	1998 Kobe EQ. Port Island (PI) VA. GL.-32.4 m Outcrop	7.2	24	0.94	18	1.9	2.6	5.9	1.39	49	0.0108	0.0351	0.0716
	C-2				0.96	18	1.7	2.5	5.2	1.39	48	0.0108	0.0338	0.0733
D	D-1	1998 Kobe EQ. Takasago (TKS) VA. GL. -0 m	7.2	36	0.59	65	16.9	18.0	20.2	6.37	50	0.0097	0.0264	0.0514
	D-2				0.51	56	13.1	15.9	17.6	6.56	50	0.0123	0.0256	0.0478
E	E-1	2003 Tokachi-oki EQ. K-NET Kitami	8.0	229	0.62	57	36.3	38.9	43.2	4.13	49	0.0120	0.0337	0.0568
	E-2				0.59	67	48.2	55.6	58.0	4.08	49	0.0146	0.0375	0.0504
F	F-1	2011 Tohoku EQ. K-NET Urayasu	9.0	380	0.55	109	58.8	60.1	61.7	6.53	48	0.0131	0.0221	0.0419
	F-2				0.29	72	54.3	59.5	61.8	4.82	43	0.0182	0.0268	0.0351

In Figure 23 (a), six acceleration time histories are illustrated with dash lines superposed by corresponding stress time histories with solid lines; A-1 to F-1, reproduced in the undrained cyclic torsional simple shear tests. The duration and number of cycles are considerably differentiated among the waves depending on the magnitudes M_J and the hypocenter distances R.

Sequences of double amplitudes of acceleration/stress obtained by zero-cross calculations of the time histories are illustrated in Figure 23 (b) with open/close columns, respectively, from larger to smaller DA amplitudes normalized by the first maximum value (starting from unity) versus the sequential number of cycles (a half of zero-crossing numbers). This reveals that the stress time histories are good enough to represent wave irregularities of widely varied earthquakes, though they are not in exact proportion to the acceleration amplitudes due to insufficient performance of the test device in reproducing smaller amplitudes. The total number of cycles $N_{c\text{-}total}$ of the stress waves with amplitudes exceeding 5% of the maximum listed in Table 1 tends to increase from Wave A to F with corresponding M_J and R-values, which seems to divide the motions into two groups A ~ C and D ~ F of smaller and larger N_c, respectively.
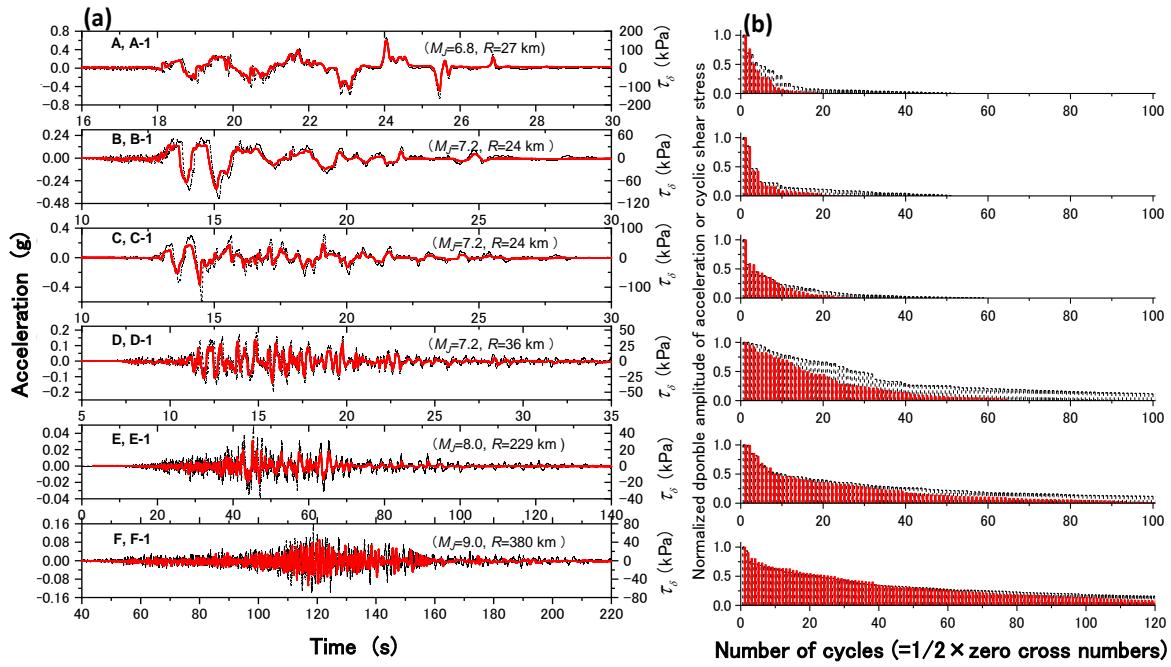
Figure 23. Irregular acceleration/shear stress waves of A to F: (a) Accelerations superposed by stress time histories in torsional simple shear tests, (b) Sequences of normalized double-amplitude acceleration/stress versus number of cycles N_c.

Also indicated in Table 1 are relative damage levels D_L for liquefaction calculated on Wave A to F in the fatigue theory sometimes addressed as a theoretical background of the stress-based liquefaction evaluation (e.g. Annaki and Lee [32]).

Postulate here that substituting the maximum cyclic stress ratio $CSR = CSR_{max} = 1.0$ and the number of cycles $N_c = N_L = 1$ into Eq. (1) gives a relative damage level $D_L = 1.0$, then a single cycle of an arbitrary stress ratio CSR_j smaller than $CSR_{max} = 1.0$ gives a relative damage level given as $D_{Lj} = 1/N_{Lj} = (CSR_j)^{-1/b}$, and the sum of the relative damage levels for individual amplitudes can be calculated as;

$$D_L = \sum_j D_{Lj} = \sum_j 1/N_{Lj} = \sum_j \left(CSR_j\right)^{-1/b} \tag{15}$$

The D_L-values summarized in Table 1 are larger in wave group D ~ F than in group A~C, though Wave D shows unexpectedly large D_L despite its smaller earthquake magnitude and epicenter distance. However, despite the large differences among the D_L-values, the test results indicate that the liquefaction potentials by the six motions are almost solely dependent on the dissipated energy $\sum \Delta W / \sigma'_c$ as shown later in Figure 28.

3.4.2.   Effect of wave irregularity on dissipated energy for liquefaction

Figure 24 shows 12 stress-strain curves from the start to double-amplitude strain $\gamma_{DA} = 20\sim30\%$ obtained by the torsional tests using the 6 waves A to F tested twice each with different amplitudes. From each chart, the cumulative dissipated energy $\sum \Delta W$ to a given cycle addressed in the following

figures was calculated in the same way as in harmonic waves using Eq. (5). Each hysteresis curve here is defined in terms of stress, starting upward from $\tau_d = 0$ and ending with the next $\tau_d = 0$.
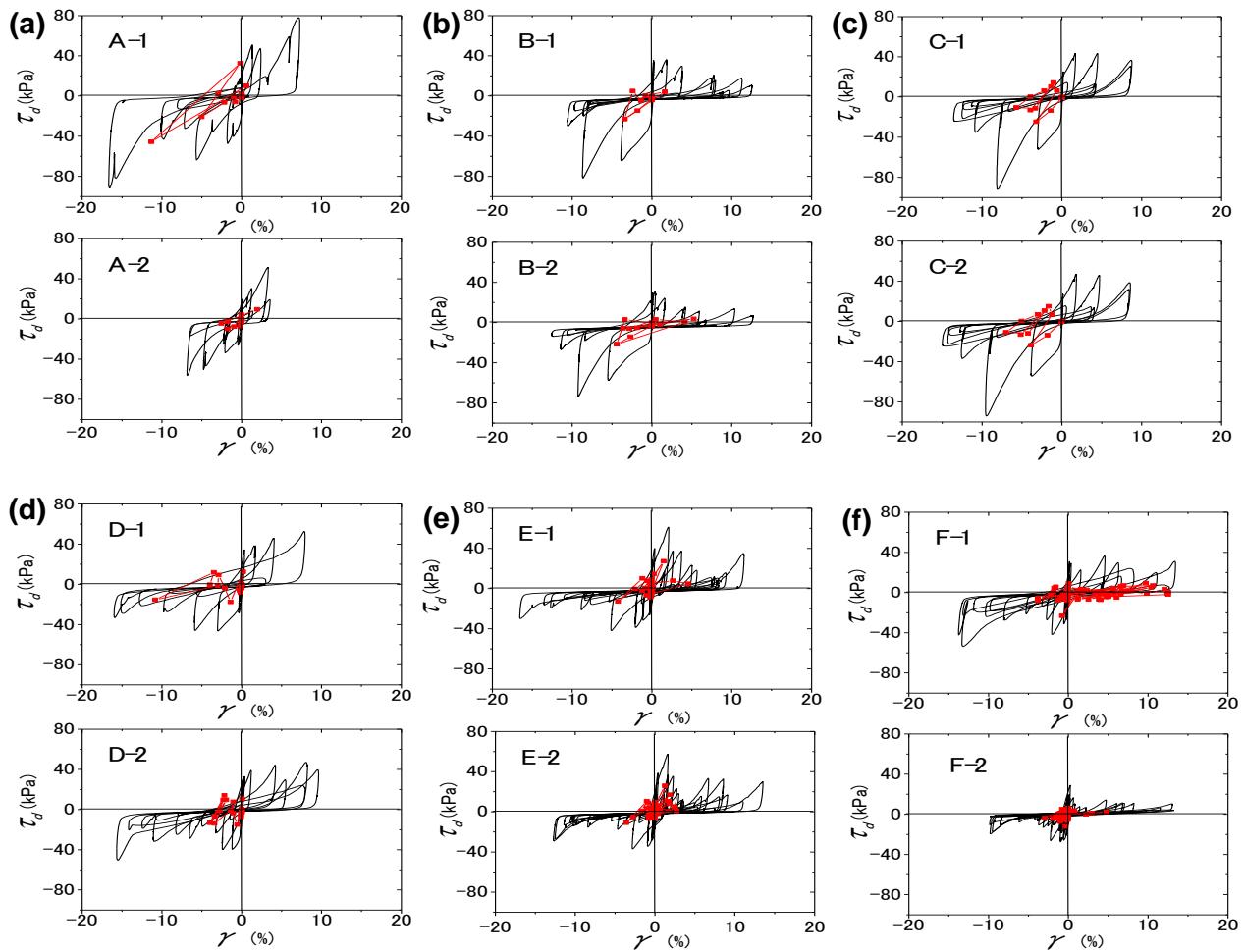
Figure 24. All stress-strain hysteresis loops and loop center movements around the origins during irregular loading by six motions A to F tested each twice with two amplitudes by torsional simple shear tests.

The solid dots connected with solid lines overlaid on the diagrams represent the means of maximum and minimum stresses and corresponding strains in individual cycles of the irregular motions. Unlike harmonic loading where stress and strain are both symmetrical over the origin, the stress-strain loops are not only irregular but their centers tend to deviate from the origin cycle by cycle.

In Figure 25 (a), the plots of the pressure ratio r_u versus energy $\sum \Delta W/\sigma'_c$ are superposed for all the irregular waves to compare with those of harmonic waves shown in Figure 18. The correlations for the former are more dispersed than the latter presumably because of poor reproductions of the targeted D_r-values, though their mean values are essentially coincidental. The γ_{DA} versus $\sum \Delta W/\sigma'_c$ plots in Figure 25 (b) look similar between the irregular and harmonic motions, and the two inflection points mentioned before in the harmonic motions can be identified in the irregular motions, too. The correlations may be recognized to be almost unique up to the energy around $\sum \Delta W/\sigma'_c \approx 0.02\sim0.04$, corresponding to the initial liquefaction but increasingly dispersed beyond that.
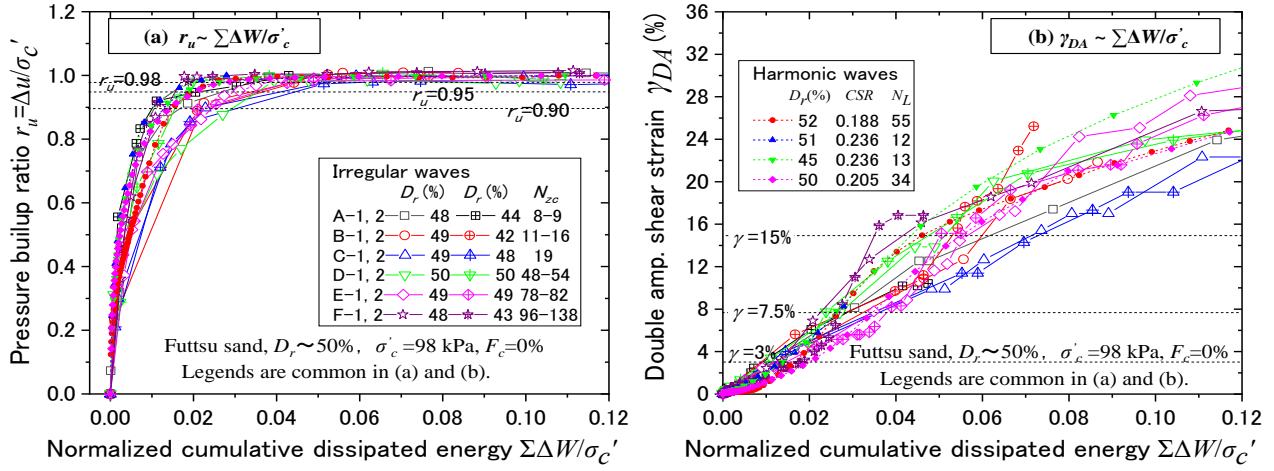
Figure 25. Torsional simple shear test results by irregular waves A to F compared with those by harmonic waves: (a) Pore-pressure ratio r_u versus dissipated energy $\sum \Delta W/\sigma'_c$ and (b) Double-amplitude shear strain γ_{DA} versus dissipated energy $\sum \Delta W/\sigma'_c$.

3.4.3. Uniqueness of dissipated energy for liquefaction by torsional shear test

In Figure 26 (a) ~ (c), dissipated energies $\sum \Delta W/\sigma'_c$ for given strains γ_{DA} = 3, 7.5, 15% in the harmonic wave tests read off from Figures 18,19 and 21 are plotted versus the corresponding number of cycles N_c in the horizontal axis. Among them, the chart (a) shows plots for $D_r \approx 50\%$, $F_c = 0$, $\sigma'_c =$ 49, 98, 196 kPa, while the charts (b) for $D_r \approx 30\%$, $F_c = 0$, and the charts (c) for $D_r \approx 50\%$, $F_c = 10$~30%, respectively, both under $\sigma'_c = 98$ kPa. In Figure 26 (a), $\sum \Delta W/\sigma'_c$ may be considered N_c-independent for a wide range of $N_c \approx 2$ to 100 and DA strains γ_{DA} =3, 7.5, 15%. If the difference of confining stress σ'_c = 49~196 kPa on $\sum \Delta W/\sigma'_c$ is ignored as suggested in Figure 22 (b), the average dissipated energies for $D_r \approx 50\%$ are $\sum \Delta W/\sigma'_c$ = 0.017, 0.028, and 0.047 as indicated with the thick dashed lines corresponding to γ_{DA} = 3, 7.5, 15%, respectively. For other test conditions in Figure 26 (b) and (c), no systematic N_c-dependent variations of energy outrivaling the data dispersions may be observed, indicating that the dissipated energy is almost uniquely correlated with double-amplitude shear strain γ_{DA} for sands regardless of the number of cycles N_c or the cyclic stress ratio CSR.
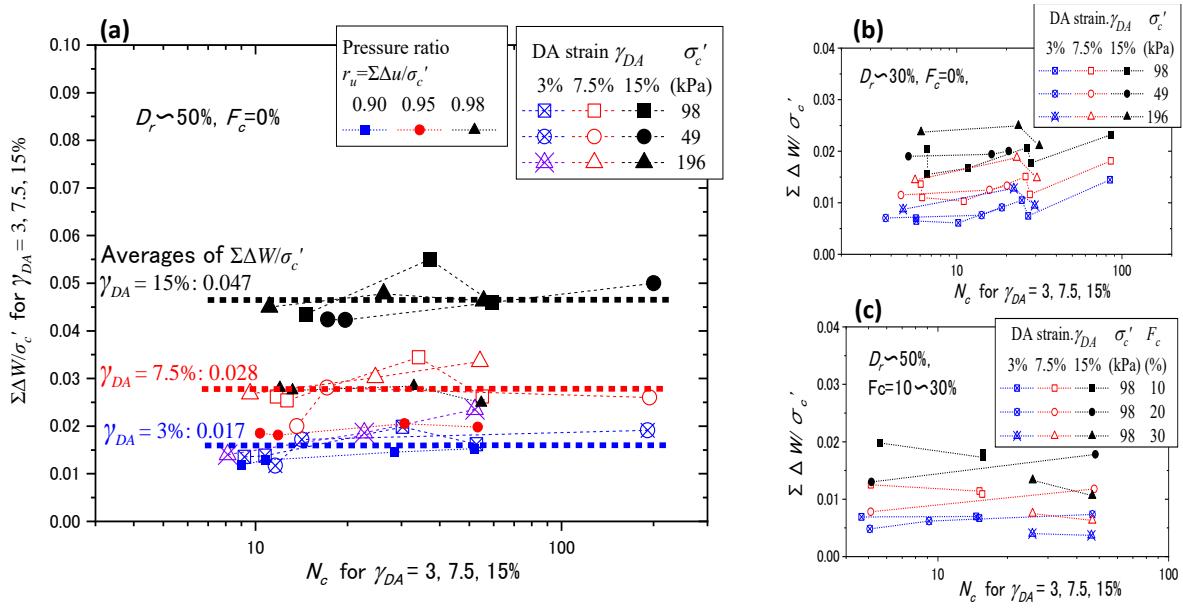
Figure 26. $\sum\Delta W/\sigma'_c$ for γ_{DA} = 3, 7.5, 15% versus N_c for harmonic wave: (a) $D_r \approx 50\%$, F_c = 0%, σ_c' = 49, 98, 196 kPa, (b) $D_r \approx 30\%$, F_c = 0%, σ_c' = 98 kPa, and (c) $D_r \approx 50\%$, F_c = 10~30%, σ_c' = 98 kPa.
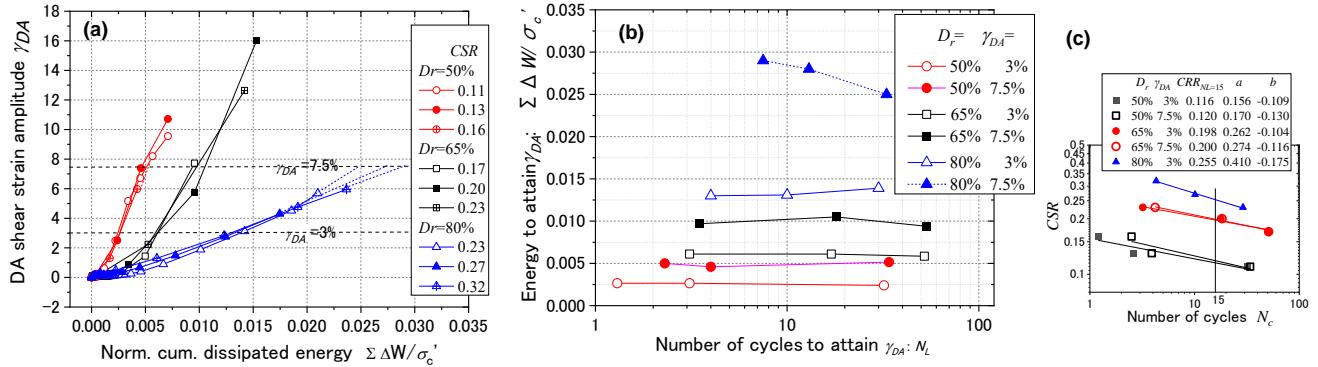
Figure 27. Torsional test results on Toyoura sand with D_r = 50, 65, 80% (by Prof. Sako of Nihon University & processed in [20]): (a) $\sum\Delta W/\sigma'_c$ versus γ_{DA}, (b) $\sum\Delta W/\sigma'_c$ versus number of cycles N_c, and (c) corresponding *CSR* versus N_c for SBM.

In Figure 27 (a), another torsional shear test using clean Toyoura sand conducted by Sako (2019) [38] (the data was processed later by the present author [20]) is depicted in terms of the strain amplitude γ_{DA} versus the energy $\sum\Delta W/\sigma'_c$ relationships. Because the test was carried out with greater care in precisely reproducing targeted relative densities, the energies $\sum\Delta W/\sigma'_c$ are very uniquely correlated with the double amplitude strain γ_{DA}, and those for γ_{DA} = 3, 7.5% read off are surprisingly flat versus the number of loading cycles N_c in Figure 27 (b). Though the D_r-value reported as D_r = 50% [38] seems to be too small considering $\sum\Delta W/\sigma'_c$ or $CRR_{NL=15}$ shown in Figure 27 (c), the almost perfect N_L-independency of $\sum\Delta W/\sigma'_c$ shown here serves as good experimental evidence demonstrating the uniqueness of energy for induced shear strain in the simple shear stress condition if sand density is kept precisely the same.
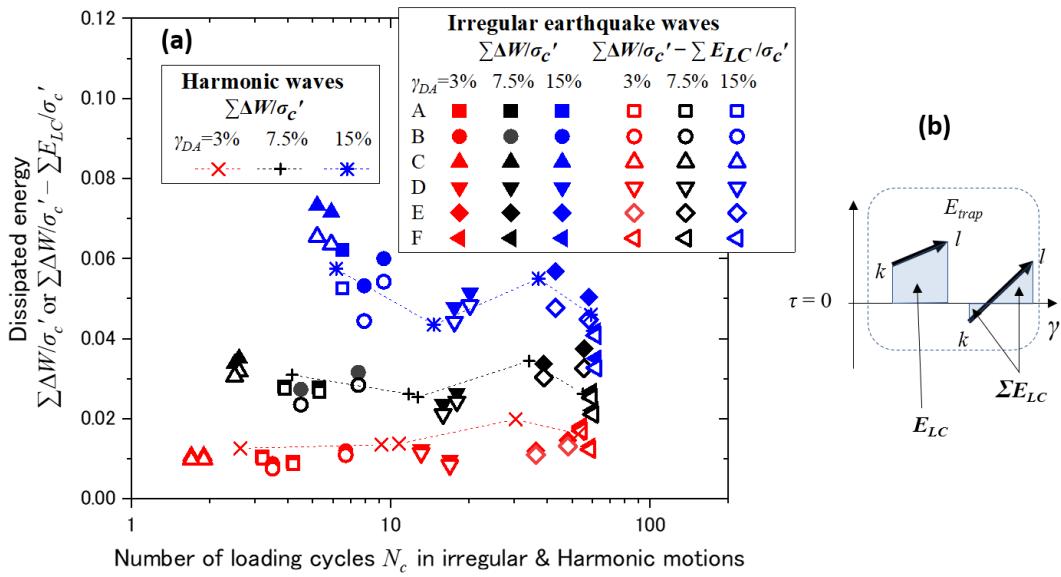
Figure 28. Dissipated energy $\sum\Delta W/\sigma'_c$ or modified dissipated energy ($\sum\Delta W/\sigma'_c - \sum E_{LC}/\sigma'_c$) considering moving loop centers versus N_c for γ_{DA} = 3, 7.5, 15%, in torsional tests for irregular motions (a), and Dissipated energies ΣE_{LC} from vector kl connecting stress ~ strain hysteresis centers (b).

In Figure 28, the cumulative dissipated energies $\sum\Delta W/\sigma'_c$ by the irregular waves A~F on the clean Futtsu sand with $D_r \approx 50\%$ under $\sigma'_c = 98$ kPa, which are read off from Figure 25 (b) for γ_{DA} = 3, 7.5, 15%, are plotted with solid symbols versus the number of cycles N_c in a log scale corresponding to those particular strains. To count N_c from the start of the irregular waves, major cycles with DA stress amplitudes exceeding 5% of the maximum were selected as already explained in Figure 23 (b).

On the same diagram, the $\sum\Delta W/\sigma'_c$ versus N_c plots by harmonic wave for $D_r \approx 50\%$ and $\sigma'_c = 98$ kPa shown in Figure 26 (a) are superposed, by assuming similarity between the numbers N_c in harmonic and irregular motions, respectively. The irregular and harmonic test results are almost compatible in terms of the absolute value of $\sum\Delta W/\sigma'_c$ for γ_{DA} = 3, 7.5, and 15% despite data scatters. It also shows that the energy $\sum\Delta W/\sigma'_c$ is essentially flat against N_c for γ_{DA} = 3 and 7.5%, indicating that the dissipated energy uniquely determines the initial liquefaction regardless of the motions, harmonic or irregular.

Thus, Figure 28 indicates that the energies for γ_{DA} = 3% and 7.5% are essentially independent of N_c, implying that the performance up to the initial liquefaction is uniquely determined by energy even in the irregular waves A ~ F widely varied in terms of earthquake magnitude and epicenter distance, *CSR*, number of cycles, frequency contents, duration, and the damage level D_L already explained.

Figure 28 also indicates that the energies $\sum\Delta W/\sigma'_c$ at larger strains such as γ_{DA} = 15% appear to decrease with increasing N_c though not so drastically. It is shown that, in irregular waves unlike harmonic waves, the center points of stress ~ strain hysteresis loops tend to move around the origin as already pointed out with solid lines & dots in Figure 24. This indicates that the deviated shear stress may increase the liquefaction resistance due to the cyclic mobility of dilative sands (e.g. Kokusho 2020 [39]). This will increase the dissipated energy for irregular motions of smaller N_c or larger *CSR* particularly, wherein the off-origin deviations of the mean stress tend to be greater.

To evaluate the stress-deviation effect quantitatively, the additional energy due to the stress bias may be roughly assessed from the movements of the solid dots in Figure 24, schematically illustrated by the vector k to l in Figure 28 (b). Then, the additional dissipated energy may be roughly evaluated by shaded areas E_{LC}, trapezoidal or triangular depending on whether the vector kl is on one side or crossing the $\tau = 0$ line. Thus, the energy $\sum E_{LC}/\sigma'_c$, using E_{LC} calculated individually and summed up for all the major loops of an irregular wave and normalized by σ'_c, may evaluate the dissipated energy by the stress bias.

In Figure 28 (a), the dissipated energy after subtracted by the biased energy, $(\sum \Delta W/\sigma'_c - \sum E_{LC}/\sigma'_c)$, is also overlaid with open symbols. Note that the energy $\sum E_{LC}/\sigma'_c$ seems to have an insignificant impact regarding the calculated energy for $\gamma_{DA} = 3$ and 7.5. Also note for $\gamma_{DA} = 15\%$ that, the N_c-dependency of dissipated energy becomes milder by this modification, resulting in the energy trend almost flat against N_c and compatible with the harmonic motion except for the two motions C and F.

Thus, the test results indicate that the initial liquefaction can be uniquely predicted using the dissipated energy irrespective of input waves. However, the energy-based prediction for larger strains in high precision seems to be difficult and less meaningful from an engineering point of view, considering the variabilities of soil properties under ultra-low effective confining stress during liquefaction and irregular design motions. Hence, uncertainties in predicting strains far beyond the initial liquefaction should be accepted in design to a certain extent.

Such an acceptance seems inevitable not only in the energy-based evaluation but also in other sophisticated numerical tools when larger post-liquefaction strains need to be evaluated in Performance-Based Design. This also indicates that a deterministic approach for post-liquefaction residual deformation based on near-zero effective stress properties of liquefying sands using a single earthquake motion is irrelevant. Instead, a probabilistic approach taking account of the variability of soil properties and irregular waves has greater relevance in evaluating post-liquefaction large strains. Regarding this, the energy approach can serve as a simple and effective tool to quantify not only the liquefaction potential but also post-liquefaction strain development quite reasonably.

4. Energy demand for liquefaction to compare with capacity

Earthquake energy was first dealt with quantitatively by seismologists (Gutenberg and Richter 1942 [40], 1956 [6,41]) to evaluate the total energy released from a seismic source based on observed earthquake records assuming the spherical energy radiation for body waves. From the viewpoint of engineering design where acceleration and stress are always focused on, very few researchers have tried to interpret earthquake motions as energy demand. Among them, Sarma (1971) [42] calculated site-specific demand energies from velocity records and compared them with spherically radiated energy from the earthquake source. In liquefaction evaluations, energy-based methods have been proposed [3–5], where the energy capacity for liquefaction triggering was compared with earthquake energy demand [6].

While the wave energy defined seismologically seems to correspond to demand energy at hard bedrock neglecting the effect of softer surface layers, how the demand energy transmits as earthquake waves from hard bedrock at a depth to ground surface had not been discussed for a long time. Kokusho and Motoyama (2002) [24] performed a basic study on the energy flow of seismic waves in surface layers based on the one-dimensional multi-reflection theory of SH waves utilizing vertical array records during the 1995 Kobe earthquake, which was followed by a theoretical study on the same topic by Kokusho et al., (2007) [43]. Similar studies using numerous vertical array data were further carried out to understand general trends of the energy demand in surface layers [25,26].

In this chapter, the energy demand in surface soils is calculated assuming 1D multi-reflection of SH-wave using vertical array records in actual soil profiles. After touching upon basic theories on wave energy, empirical formulas already developed using a vertical array strong motion database are explained. Then, how to determine the demand energy from a given earthquake and compare it with the capacity energy in the liquefaction evaluation is discussed considering the effect of free ground surface.

4.1. Energy flow of a 1D propagating SH wave

The horizontal displacement u in the SH wave propagating to the positive direction of the z-axis, as illustrated in Figure 29, can be expressed as;

$$u = A \cdot f\left(z - V_s t\right) \tag{16}$$

Here, t = time, z = upward coordinate, V_s = S-wave velocity, A = wave amplitude, and $f(\ )$ is an arbitrary waveform function. Then, shear strain γ is readily obtained.

$$\gamma = \partial u / \partial z = \dot{u} / V_s \tag{17}$$

where $\dot{u} = \partial u / \partial t$ is particle velocity (e.g., Kokusho 2017 [37]).
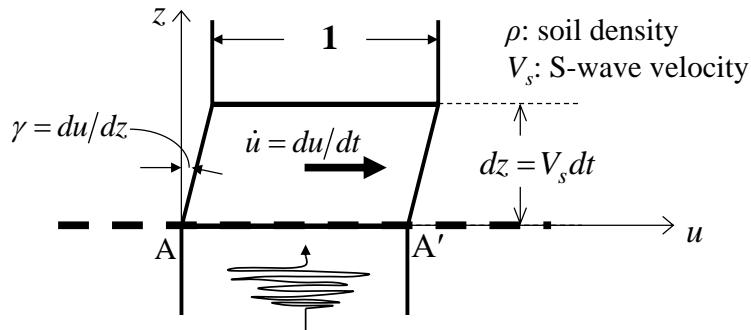
Figure 29. Schematic illustration of wave energy in upward SH wave propagation.

As for the wave energy carried by the upward SH wave passing through a horizontal plane A-A' of a unit area, kinetic energy increment ΔE_k can be written as Eq. (18) for a soil element of a unit horizontal area times a small thickness $dz = V_s \Delta t$ (a travel distance in a time increment Δt) having particle velocity $\dot{u}$.

$$\Delta E_k = \frac{1}{2} \rho V_s \Delta t \left(\dot{u}\right)^2 \tag{18}$$

Strain energy ΔE_γ is expressed similarly by shear stress $\tau = G\gamma$ and shear strain γ, and using Eq. (17) as:

$$\Delta E_\gamma = \int_0^\gamma \left(V_s \Delta t\right) \tau \, d\gamma = \left(V_s \Delta t\right) G \int_0^\gamma \gamma \, d\gamma = \frac{1}{2} \rho V_s^3 \Delta t \gamma^2 = \frac{1}{2} \rho V_s \Delta t \left(\dot{u}\right)^2 \tag{19}$$

Hence, $\Delta E_k = \Delta E_\gamma$ holds in the same soil element, and the wave energy passing through the unit area in the time increment Δt is their sum expressed as:

$$\Delta E = \Delta E_k + \Delta E_\gamma = \rho V_s \Delta t \left(\dot{u} \right)^2 \tag{20}$$

Cumulative energy in a time interval $t = t_1 \sim t_2$ can be expressed as the sum of the kinetic and strain energies, E_k and E_e, of an equal amount (Timoshenko and Goodier 1951 [44], Bath 1956 [45], and Sarma 1971 [42]).

$$E = E_k + E_\gamma = \rho V_s \int_{t_1}^{t_2} \left(\dot{u} \right)^2 dt \tag{21}$$

Note that the unit of E is *Energy* divided by *Area*, and kJ/m^2 will be used hereafter. The time derivative of the energy called energy flux or energy flow rate is written as:

$$dE/dt = dE_k/dt + dE_\gamma/dt = \rho V_s \left(\dot{u} \right)^2 \tag{22}$$

Thus, the seismic wave energy depends on the particle velocity $\dot{u}$ and the S-wave impedance ρV_s of the soil where the ground motion is recorded. In this context, it seems unreasonable from the viewpoint of energy to define design motions in terms of acceleration or velocity without specifying the associated impedance value ρV_s. Hence, when a design motion with a given amplitude is discussed, it is essential from the viewpoint of energy to identify the impedance value or soil condition where the motion is recorded.

4.2. Energy flow calculated by vertical array records

Subsurface energy flows were calculated utilizing vertical array records during nine strong earthquakes acquired in recent decades in Japan by assuming the vertical propagation of SH waves to know depth-dependent energy demands and apply them in energy-based liquefaction evaluation.

4.2.1.   How to calculate energy flow

First, the level ground is idealized by a model of horizontal soil layers where the SH wave propagates vertically as shown in Figure 30. Then, it is necessary to evaluate the energy flow by separating a recorded subsurface record into upward and downward waves. Let $E_{u,m}$ and $E_{d,m}$ denote the upward and downward energies at the upper boundary of the m-th layer, and corresponding energies at the lower boundary of the $(m-1)$-th layer as $E'_{u,m-1}$, $E'_{d,m-1}$, respectively. Considering the energy balance at the boundary between the m-th and $(m-1)$-th layer, the next equation holds, where E_T means the total energy passing through the boundary during a given earthquake.

$$E_{u,m} + E'_{d,m-1} = E'_{u,m-1} + E_{d,m} \equiv E_T \tag{23}$$

From this, the following equation is readily derived.

$$E_{u,m} - E_{d,m} = E'_{u,m-1} - E'_{d,m-1} \equiv E_w \tag{24}$$

Here, E_w is the energy dissipated in soil layers above the layer boundary during an earthquake, because all the energy computed here is assumed to transmit vertically.
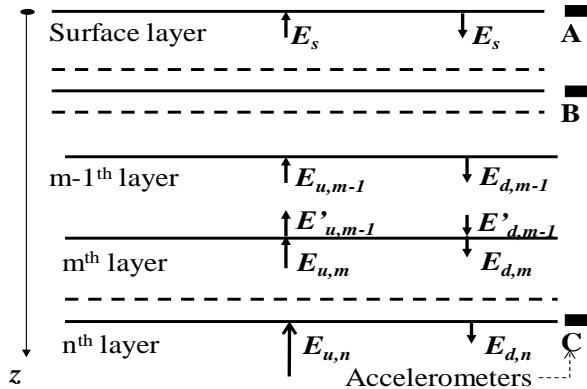
Figure 30. Level ground idealized by a set of horizontal soil layers with vertical array seismometers, A, B, and C.

Based on the multiple reflection theory, the upward and downward SH waves and corresponding wave energies at arbitrary levels can be evaluated from a single record at a given level using the condition that the ground surface is free from shear stress (e.g., Schnabel et al., 1972 [46]). If downhole records are available, however, they will considerably improve the energy flow evaluation, which may not fully comply with the simple 1D SH-wave propagation theory. Suppose seismic records at two subsurface levels, B and C, are available in addition to surface A, as illustrated in Figure 30. The energy flow between B and C can be calculated from earthquake records at the two levels [24]. Between the ground surface, Point A, and Point B, conversely, two sets of energy flow can be calculated using the earthquake record either at A or B. The two sets of energy may then be averaged with the weight of relative proximity to A and B to have plausible values (Kokusho and Suzuki 2011 [25]).

Nine earthquakes (Kobe EQ. & EQ1 to EQ8) are addressed here with the moment magnitude M_W = 6.6 to 7.9 or JMA magnitude (magnitude in Japan Meteorological Agency scale, similar to Richter scale) M_J = 6.7 to 8.0. In total, 30 vertical array sites were selected during the nine earthquakes with focal distances ranging from 9 to 227 km. The deepest depth of the vertical arrays of three-dimensional accelerometers spanned from 83 to 260 m, though most of them were nearly 100 m. The S-wave velocities at the base were widely diverged as V_s = 380~2800 m/s due to geological differences, while the surface velocities were mostly V_s = 90~430 m/s. Four vertical array sites for the 1995 Kobe EQ. and one site for EQ7 consist of accelerometers at three or more different levels, including the ground surface, while all others belonging to the KiK-net consist of only two levels, a surface and base [25].

The scalar sum of the wave energies calculated from the two orthogonal horizontal acceleration records was used for the energy flow evaluations. Equivalent linear soil properties, S-wave velocity V_s and damping ratio D both assumed as non-viscous or frequency independent (Ishihara 1996 [47]), were optimized for the main shock records and incorporated in the evaluations.

4.2.2. General trends of energy flow in vertical arrays

Figure 31 depicts the variations of upward energy E_u along the depth z calculated for the nine earthquakes at 30 vertical array sites [25]. Considering the large differences in the absolute energies

among the records, the horizontal axis is taken in log scale. The energy E_u shows an obvious decreasing trend in most sites with decreasing depth regardless of the energy magnitude. In some sites, it tends to decrease to less than one-tenth from the base to the surface, and the trend is more pronounced near the surface in contrast to the depth of 50~100 m or below.
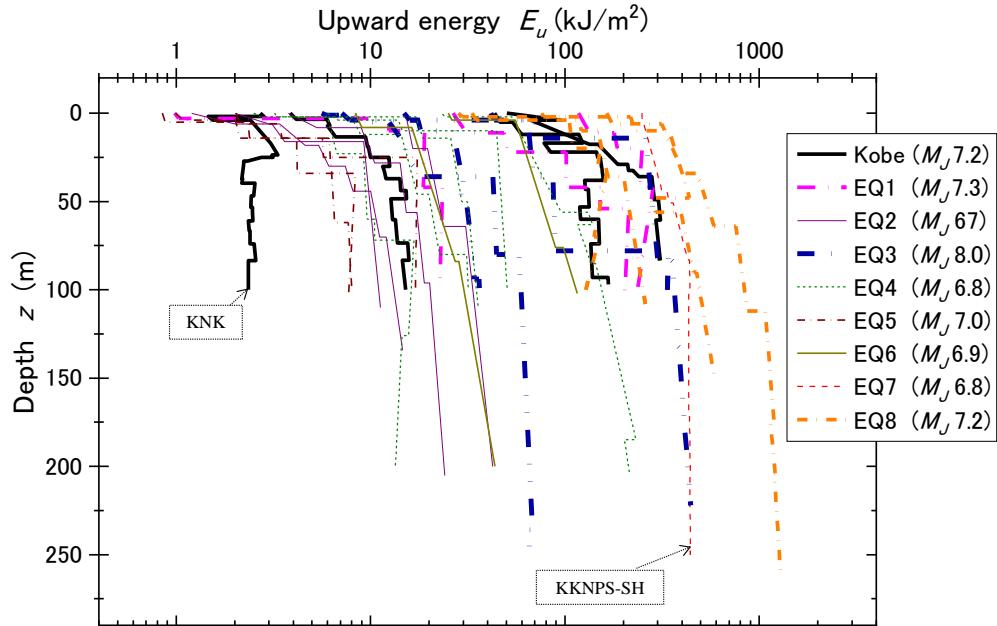
Figure 31. Variations of upward energy E_u along depth z calculated assuming SH-wave propagation by vertical array records at 30 vertical array sites during nine earthquakes.

There used to be a traditional view in engineering seismology that the wave energy (=*square of velocity amplitude × wave impedance*) is kept constant as seismic waves propagate underground (e.g., Joyner and Fumal 1984 [48]). Hence, the velocity amplitude was generally considered inversely proportional to the square root of the impedance ρV_s. Figure 31 indicates that this view is not true, at least in shallow depths at most sites despite a few exceptions (KNK and KKNPS-SH).

Closer scrutiny of Figure 31 has revealed ([25], Kokusho 2022 [49]) that the major cause of the drastic decrease of upward energy with decreasing depth is layer boundaries of clear impedance ratio near the ground surface, where a large amount of upward wave energy is reflected downward to return to the earth before arriving at surface soils. Also revealed was that internal energy dissipation is another cause in those sites where soft soils are prevalent near the surface.

4.3. Empirical formulas for upward energy

4.3.1.   Upward energy ratio versus impedance ratio

In order to evaluate the decreasing rate of the upward energy as it approaches the ground surface, an empirical formula has been developed, wherein ratios of upward energies between layers are correlated to corresponding impedance ratios using the dataset of vertical array records addressed above [26]. Among the depth-dependent upward energy variations, 23 sites are used where the mutual

difference is within 25% between the two upward energies at the deepest level calculated from measured motions at the ground surface and the deepest level.

Impedance ratios α and upward energy ratios β defined between two neighboring layers, m and $m+1$, in a given soil profile in Figure 30 are calculated at individual sites from surface to base as;

$$\alpha = \left(\rho V_s\right)_m \Big/ \left(\rho V_s\right)_{m+1} \;,\; \beta = \left(E_u\right)_m \Big/ \left(E_u\right)_{m+1} \tag{25}$$

The soil density was assumed depending on the S-wave velocity as: $\rho=1.6\sim2.0$ t/m^3 for $V_s \leq 300$ m/s, $\rho = 2.0\sim2.2$ t/m^3 for 300 m/s $\leq V_s \leq 700$ m/s, $\rho = 2.3\sim2.4$ t/m^3 for 700 m/s $\leq V_s \leq 1000$ m/s, and $\rho = 2.5\sim2.7$ t/m^3 for 1000 m/s $\leq V_s < 3000$ m/s. The energy ratios β are plotted versus the corresponding impedance ratios α in Figure 32 (a) for all layers above the deepest levels with different symbols in the 23 vertical array sites. For most data points, $\alpha \leq 1.0$ holds because the impedance ratio is normally less than unity (ρV_s is getting larger in deeper layers). It is quite reasonable to assume that $\beta=0$ for $\alpha=0$ at a ground surface, and $\beta = 1$ for $\alpha = 1$ within a uniform base layer. Hence, a next simple power function may be practically used for $0 \leq \alpha \leq 1.0$ to approximate the plots as the thick solid curve in Figure 32 (a), and the power $n = 0.70$ is obtained from the least mean square method with the determination coefficient $R^2 = 0.81$.

$$\beta = \alpha^{0.70} : 0 \leq \alpha \leq 1.0 \tag{26}$$

Furthermore, the impedance ratio α and the upward energy ratio β may be redefined differently from Eq. (25), between an arbitrary m-th layer and the deepest base layer in a vertical array as follows.

$$\alpha = \left(\rho V_s\right)_m \Big/ \left(\rho V_s\right)_{base} \;,\; \beta = \left(E_u\right)_m \Big/ \left(E_u\right)_{base} \tag{27}$$
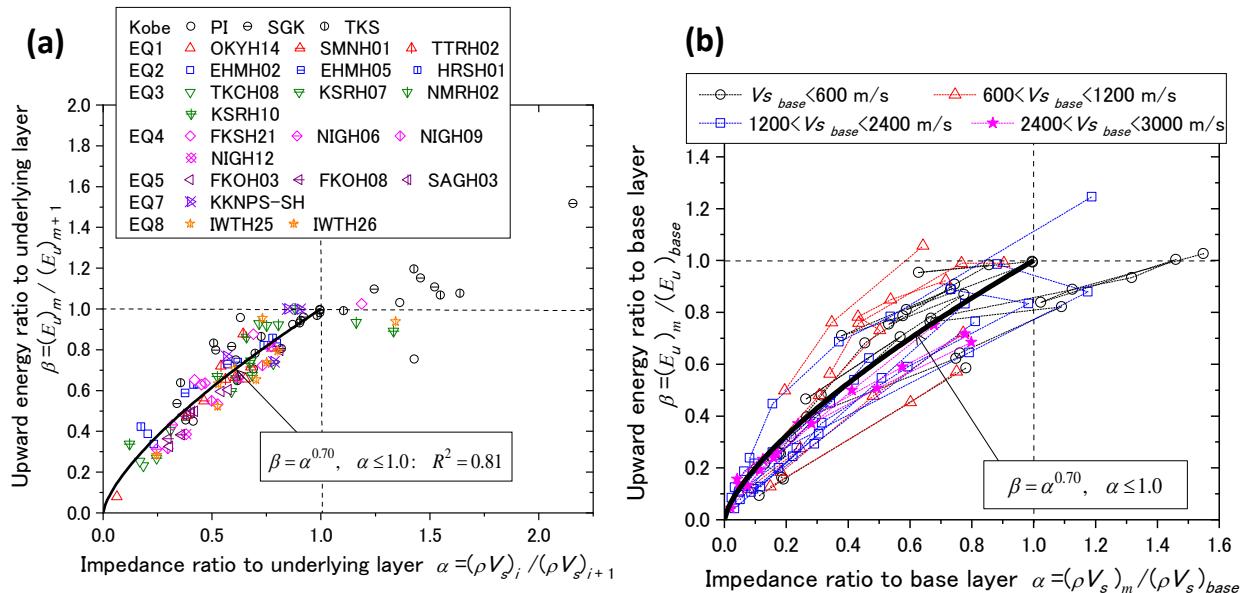
Figure 32. Upward energy ratios β versus corresponding impedance ratios α compared with the empirical formula: (a) Between two neighboring layers and (b) Between arbitrary layer & base layer.

In Figure 32 (b), data points for all the layers at the 23 vertical array sites are plotted on the α versus β diagram following the definition in Eq. (27), wherein the symbols are connected with thin dashed lines for individual sites and differentiated by four steps of V_s-values at the base layers. Though the plots are more dispersed than in Figure 32 (a), the curve by Eq. (26), using α and β redefined in Eq. (27) seems to approximate the plots to a certain degree. As shown in the chart (b), some of the V_s-values of base layers are very high, 2400–3000 m/s, almost equivalent to seismologically defined stiff bedrocks. This indicates that Eq. (26) may be used for practical purposes to evaluate the upward energy in a shallow soil layer directly from the incident energy at a deep seismological bedrock using the impedance ratio defined between the two in Eq. (27).

4.3.2. Upward energy at seismological bedrock

Upward energies at the deepest levels (base layers) denoted here as $(E_u)_{base}$ calculated from the downhole records and the associated impedance values are plotted with close symbols in the full-logarithmic scale versus hypocenter distances R (m) in Figure 33 at all 30 vertical array sites for nine earthquakes [25,26]. Although the plots are widely scattered, the decreasing trends in $(E_u)_{base}$ with increasing R for individual earthquakes are not difficult to identify. Among the nine earthquakes, the plots of EQ3 with $M_J = 8.0$ (2003 Tokachi-Oki earthquake) are relatively higher on the upper-right side of the diagram reasonably as a larger magnitude subduction earthquake, while other crustal earthquakes with M_J around 7.0 are lower on the lower-left side.

Based on the finding that Eq. (26) may be conveniently used to roughly evaluate the energy ratio between arbitrary two layers, the same equation is further used here to estimate the incident or upward energies at the seismological bedrocks $(E_u)_{sbr}$ from those at the base layers $(E_u)_{base}$ of individual vertical arrays. The impedance for the seismological bedrock is calculated thereby using $V_s = 3000$ m/s and $\rho = 2.7$ t/m^3. It may well be justified here that major wave energy is carried by vertically propagating SH waves even in seismological bedrocks as stiff as $V_s=3000$m/s, as substantiated by some of the vertical array data in Figure 32 (b), despite the potential involvement of SV waves.
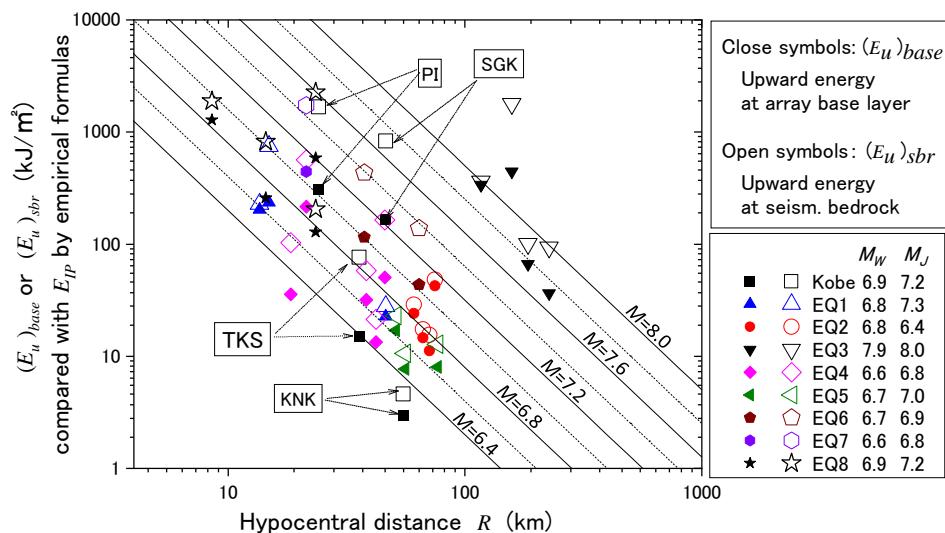
Figure 33. Upward energies at vertical array base $(E_u)_{base}$ or seismological bedrock $(E_u)_{sbr}$ versus hypocenter distance R, compared with incident energies E_{IP} versus R lines by empirical formulas.

In Figure 33, the upward energies at the calculated seismological bedrock $(E_u)_{sbr}$ are also plotted with open symbols for the nine earthquakes. They are positioned higher than the corresponding close plots because of higher ρV_s-values than those at the bottom of the vertical arrays, reflecting the upward energy decreasing as it goes up from the seismological to engineering bedrock. Straight lines drawn in Figure 33 represent the following formula of incident energy E_{IP} (kJ/m^2) versus hypocenter distance R (m) by assuming the spherical energy radiation from the center of energy release, assumed here as the hypocenter (e.g. [6]).

$$E_{IP} = E_{Total}\big/\left(4\pi R^2\right) \tag{28}$$

Total released wave energy E_{Total} in kJ is calculated by the next empirical formula [6] from earthquake magnitudes M,

$$\log E_{Total} = 1.5M + 1.8 \tag{29}$$

Concerning magnitude M, it should be reminded that in the original paper [6] the surface wave magnitude M_S was employed as M in Eq. (29). According to Utsu (1982) [50], M_S may be similar to M_W (Moment Magnitude) and M_J (Japanese Meteorological Agency Magnitude) as well with a small difference. However, the actual magnitude values of the nine earthquakes (Kobe EQ, EQ1~EQ8), which were announced by JMA in Japan and USGS in the USA, are all distinctively larger for M_J than the corresponding M_W. We also found that the incident wave energies estimated by the empirical formula Eqs. (28) and (29) using $M = M_J$ tend to be more compatible than those by $M = M_W$ with the upward energies $(E_u)_{sbr}$ calculated at the seismological bedrock using Eqs. (26) and (27) [49]. Thus, the JMA magnitude may be suitable to estimate the incident energy E_{IP} at the seismological bedrock for engineering purposes. Certainly, more detailed studies will be needed to upgrade the empirical equations by incorporating fault and path mechanisms of individual earthquakes.

4.4. Energy flow in wave propagation
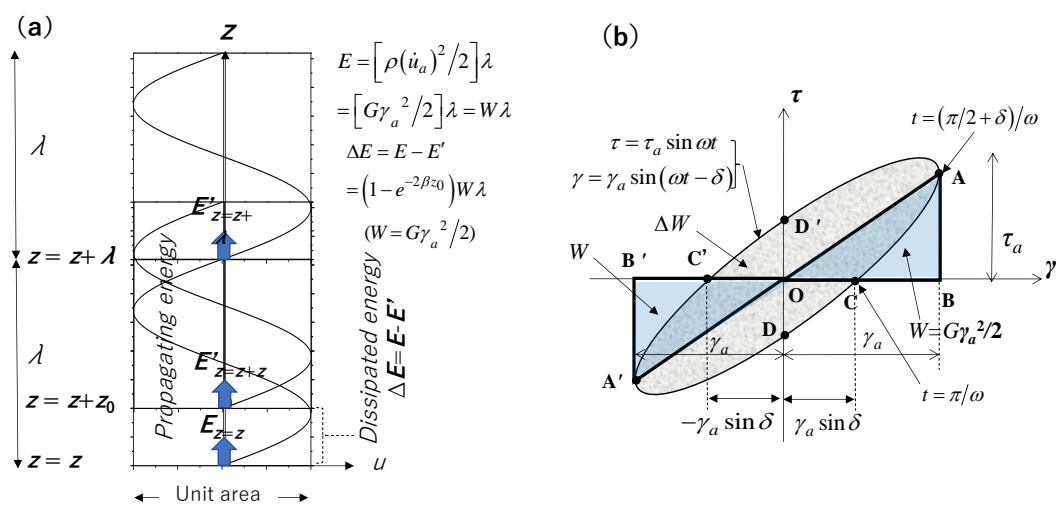
Figure 34. Wave energy E and dissipated energy ΔE in upward propagating harmonic SH-wave with wavelength λ (a), Strain energy W, and dissipated energy ΔW in cyclic loading (b), in ideal viscoelastic materials.

One of the highlights of the energy-based liquefaction evaluation developed here is to grasp the total amount of demand energy and directly compare it with the capacity to determine the extent of liquefaction at a site. The upward energy going up through a soil profile will reflect at the ground surface and come down again as the downward energy except that dissipated in the upper layers [43]. Thus, the upward energy represents all the demand energy to be compared with the capacity energy in the EBM, because the downward energy is originally a part of the upward energy. In this regard, how to compare the demand energy of design earthquake waves with the capacity or dissipated energy for liquefaction considering wave attenuation and surface reflection of the SH-wave is discussed below.

Let us consider a harmonic SH-wave shown in Figure 34 (a) propagating in the z-axis (upward direction) with time t in a viscoelastic medium as;

$$u = B \sin \omega \left(t - \left(z/V_s^* \right) \right) \tag{30}$$

Here, B = wave amplitude, $\omega = 2\pi f$ = angular frequency, and V_s^* = complex S-wave velocity considering non-viscous damping (Ishihara 1996 [47]) which can be written as;

$$V_s^* = \sqrt{(G + iG')/\rho} = V_s \left(1 + \tan^2 \delta \right)^{1/4} e^{i\delta/2} \tag{31}$$

where $G + iG'$ = complex shear modulus with real and imaginary parts and ρ = soil density. δ is the phase delay angle of the stress-strain hysteresis obtained in cyclic loading of soils, using G and G' and also correlated with damping ratio D (e.g. [37,47]) as;

$$\delta = \tan^{-1} \left(G'/G \right) = \tan^{-1} \left(2D \right) \tag{32}$$

Eq. (30) is also written in the following form;

$$u = Be^{-\beta z} \sin \omega \left(t - z/V_s' \right) \tag{33}$$

where modified S-wave velocity is defined as

$$V_s' = \frac{V_s}{\left(\cos \delta \right)^{1/2} \left(\cos \left(\delta/2 \right) \right)} \tag{34}$$

which can be approximated as $V_s' \approx V_s^*$ for $\delta \ll 1.0$. The wave attenuation coefficient β is defined [37,47] as;

$$\beta = \left(\cos \delta \right)^{1/2} \left(\sin \left(\delta/2 \right) \right) \left(\omega/V_s \right) = \left(\tan \left(\delta/2 \right) \right) \left(\omega/V_s' \right) \tag{35}$$

This can be approximated for $\delta \ll 1.0$ as

$$\beta \approx \left(\omega \tan \delta \right) / \left(2V_s \right) = \omega D / V_s \tag{36}$$

If Eq. (33) is substituted into Eq. (21), and integrated for one period $T = 2\pi/\omega$ of the harmonic wave, the energy in one wavelength $\lambda = 2\pi V_s/\omega$ can be obtained as;

$$E = \rho V_s \int_0^{2\pi/\omega} (\ddot{u})^2 dt = \rho \left(\omega^2 B^2 e^{-2\beta z} / 2 \right) \lambda \tag{37}$$

Let the amplitude of particle velocity be expressed as

$$\dot{u}_a = \left| \omega B e^{-\beta z} \cos \omega (t - z/V_s) \right|_{\max} = \omega B e^{-\beta z} \tag{38}$$

and the shear strain amplitude is assumed $\delta \ll 1.0$ as

$$\gamma_a \approx -Bk e^{-\beta z} \left| \cos \omega (t - z/V_s) \right|_{\max} = -Bk e^{-\beta z} = -\dot{u}_a/V_s \tag{39}$$

Then, the upward wave energy in Eq. (37) can be expressed as

$$E = \rho \left(\omega^2 B^2 e^{-2\beta z} / 2 \right) \lambda = \left[\rho (\dot{u}_a)^2 / 2 \right] \lambda = \left[G \gamma_a^2 / 2 \right] \lambda = W \lambda \tag{40}$$

Hence, the energy density per unit volume in the upward wave is

$$E/\lambda = \rho (\dot{u}_a)^2 / 2 = G \gamma_a^2 / 2 = W \tag{41}$$

Here, W is equal to the maximum strain energy defined in a cyclic loading test of an ideally viscoelastic material of shear modulus $G = \rho V_s^2$ with the amplitude γ_a shown in Figure 34 (b).

The wave energy E' arriving at $z+z_0$ shown in Figure 35 (a) is formulated using the energy E at z in Eq. (40) as;

$$E' = \rho \left(\omega^2 B^2 e^{-2\beta(z+z_0)} / 2 \right) = W e^{-2\beta z_0} \lambda = E e^{-2\beta z_0} \tag{42}$$

Hence, the energy dissipated in travelling from z to $z+z_0$ in one wavelength $z_0 = \lambda$ is;

$$\Delta E = E - E' = \left(1 - e^{-2\beta z_0} \right) W \lambda = \left(1 - e^{-4\pi D(z_0/\lambda)} \right) W \lambda \tag{43}$$

Thus, the ratio of dissipated energy to the total energy in one wavelength $z_0 = \lambda$ is written as;

$$\Delta E/E = 1 - e^{-4\pi D} \tag{44}$$

It can be approximated by using the Taylor expansion for $\beta = \omega D/V_s \ll 1.0$ or $D \ll 1.0$ as;

$$\Delta E/E = 1 - e^{-4\pi D} \approx 1 - (1 - 4\pi D) = 4\pi D \tag{45}$$

This relationship (Kokusho 2017) [37] resembles the next equation which correlates the dissipated energy ΔW with the elastic strain energy W using the damping ratio D in cyclic loading tests as indicated in Figure 34 (b).

$$\Delta W/W = 4\pi D \tag{46}$$

Hence, the same mechanism is supposed to govern the wave propagation as in the laboratory cyclic loading test, wherein E and ΔE correspond to W and ΔW, respectively. If the dissipated energy ΔW is negligibly small, strain energy W given to the system in the first half cycle is all recovered and used in the subsequent loading. It is thus clear that the wave energy dissipates with the ratio defined in Eq. (45) for small D during wave propagation.

4.5. Energy demand near free surface

The upward SH-wave is reflected at a ground surface and becomes a downward SH-wave as illustrated in Figure 35 (a). In this condition, the displacement of the harmonic wave with angular frequency ω may be formulated as;

$$u = Ae^{i\omega(t-z/V_s)} + Be^{i\omega(t+z/V_s)} \tag{47}$$

where the z-axis is taken downward to be positive, and A and B are amplitudes of downward and upward waves, respectively. The internal damping is assumed zero in this case for simplicity. Due to zero shear stress $\tau = 0$ at the free ground surface,

$$\tau = G\gamma = G\partial u/\partial z = -iG(\omega/V_s)(A-B)e^{i\omega t} = 0 \tag{48}$$

or $A = B$, indicating that the wave reflection occurs with the surface displacement $u = 2Be^{i\omega t}$. Accordingly, the depth-dependent variations of displacement u, particle velocity $\dot{u} = du/dt$ and shear strain $\gamma = du/dz$ during steady-state vibration by the harmonic wave are written respectively as;

$$u = Be^{i\omega t}\left(e^{i(\omega/V_s)z} + e^{-i(\omega/V_s)z}\right) = 2B\cos(\omega/V_s)z \times e^{i\omega t} \tag{49}$$

$$\dot{u} = 2B\omega\cos(\omega/V_s)z \times ie^{i\omega t} = 2i\dot{u}_a\cos(\omega/V_s)z \times e^{i\omega t} \tag{50}$$

$$\gamma = 2B(\omega/V_s)\sin(\omega/V_s)z \times (-e^{i\omega t}) = -2\gamma_a\sin(\omega/V_s)z \times e^{i\omega t} \tag{51}$$

The displacement in Eq. (49) illustrated with a dashed curve in Figure 35 (a) indicates that nodes and antinodes of vibration, $\lambda/4$ apart in between, appear regularly at every $\lambda/2$, starting from the top antinode at the surface. The kinetic and strain energies per unit volume E_k/λ and E_γ/λ averaged over the period $T = 2\pi/\omega$ can be obtained as Eqs. (52) and (53) [31].

$$E_k/\lambda = \frac{1}{2}\rho\dot{u}^2 = \frac{2\rho B^2\omega^2\cos^2(\omega/V_s)z}{2\pi/\omega}\int_0^{2\pi/\omega}\sin^2\omega t\,dt = \rho B^2\omega^2\cos^2(\omega/V_s)z \tag{52}$$

$$E_\gamma/\lambda = \frac{1}{2}G\gamma^2 = \frac{2GB^2(\omega/V_s)^2\sin^2(\omega/V_s)z}{2\pi/\omega}\int_0^{2\pi/\omega}\cos^2\omega t\,dt = \rho B^2\omega^2\sin^2(\omega/V_s)z \tag{53}$$

The sum of the two energy densities becomes quite reasonably a constant twice larger than the upward energy density as;

$$E_k \big/ \lambda + E_\gamma \big/ \lambda = \rho B^2 \omega^2 = 2W \tag{54}$$

As shown in Figure 35 (a), the strain energy normalized as $(E_\gamma/\lambda)/2W$ is 0% at the antinodes and 100% at the nodes, while the kinetic energy $(E_k/\lambda)/2W$ is vice versa. Thus, the two kinds of energy are distributed with a fixed rate of 0 to 100% depending on the depth and are not convertible to each other because of the constraints of the nodes and antinodes appearing at every quarter wavelength $\lambda/4$ for the steady-state harmonic vibration. This is a significant difference from the one-way wave propagation without any boundary in Figure 34 (a), where both the kinetic and strain energies are eligible to compensate for the dissipated energy.
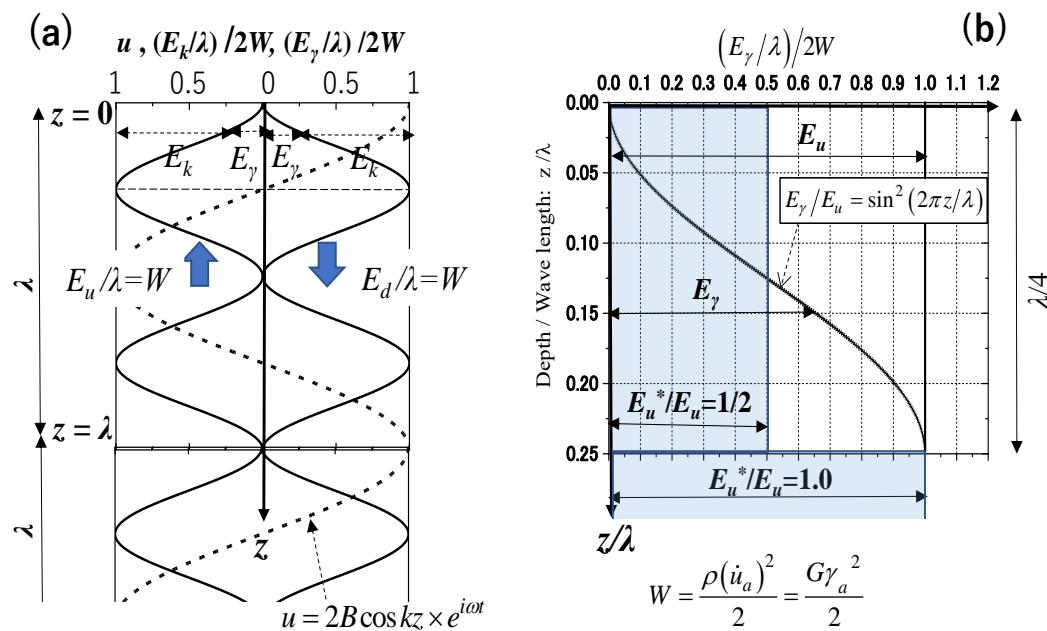
Figure 35. Wave energy versus depth near free ground surface: (a) Upward and reflected downward waves and corresponding kinetic & strain energies; E_k & E_γ, (b) Upward wave in ¼-wave length depth and energy ratio E^*/E for liquefaction.

Figure 35 (a) is, however, an extreme case by a steady harmonic motion of a single frequency and may not represent a realistic seismic response by transient irregular waves, wherein nodes and antinodes are difficult to appear steadily. Nevertheless, even in irregular seismic motions, the free ground surface consistently serves as an antinode for waves of any frequencies because of the stress-free condition. Such a surface boundary effect may well be assumed to fade away with increasing depth from the surface, difficult to transmit beyond a certain depth.

In Figure 35 (b), where the shallow depth of $\lambda/4$ from the surface is zoomed in, the normalized strain energy $(E_\gamma/\lambda)/2W$ is depicted using Eq. (53), indicating that the ratio of strain energy E_γ imparted from the upward energy E_u to compensate for the liquefaction-induced dissipated energy is increasing from zero at the ground surface to the maximum value 1.0 at $z = \lambda/4$, and the ratio is fixed depending on z during harmonic vibration as;

$$E_\gamma \big/ E_u = \sin^2 \left(2\pi z / \lambda \right) \tag{55}$$

For earthquake motions, however, the effect of the surface boundary may be limited within a shallow depth because of the irregularity of motions and the nonlinear soil properties during strong earthquakes, too. Hence, it is assumed here that, beyond the depth of a quarter wave-length $z = \lambda/4$ for $\lambda = V_s T$ corresponding to predominant periods T of earthquake motions, the SH wave propagates up and down as in Figure 34 (a) without any surface boundary effect where E_k and E_γ can freely compensate for the dissipated energy. In other words, if $E_u{}^*$ stands for the wave energy that can compensate for the dissipated energy, and E_u is the total wave energy available at the same depth z, then:

$$E_u{}^* / E_u = 1.0 \qquad \text{for} \quad z \geq \lambda/4 \tag{56}$$

In between the surface and $z = \lambda/4$, the boundary effect gradually weakens with increasing depth from $E_\gamma = 0$ or $E_u{}^* = 0$ at $z = 0$ to Eq. (56) at $z = \lambda/4$. Hence, it may be possible to take the average of Eq. (55) in between considering the effects of irregular earthquake motions as well as soil nonlinearity and simplify the energy ratio as the next equation for practical purposes.

$$E_u{}^* / E_u = 1/2 \qquad \text{for} \quad \lambda/4 > z > 0 \tag{57}$$

Considering that the wavelength $\lambda = V_s T$ may be 80 ~ 160 m in most liquefiable site conditions with average shallow S-wave velocity $V_s > 160$ m/s for $z < 20$ m and predominant periods of earthquake motions $T > 0.5$ s, the depth of $\lambda/4$ means around 20 m or deeper, indicating that for normal liquefaction evaluation depths $z < 20$ m, the upward energy may be halved as in Eq. (57) to compare with the liquefaction energy capacity [31].

To examine how well the simplification mentioned above holds, we conducted an additional numerical study on irregular earthquake motions. A uniform horizontal soil layer of 20 m thick with $\rho = 1.8$ t/m^3, $V_s = 160$ m/s, and the damping ratio $D = 0$, 20 & 40% is vibrated by surface input motions as illustrated in Figure 36 (a). Four acceleration records EQ1 to EQ4 listed in Figure 36 (b) with different durations and irregularities obtained at soft soil sites in Japan have been used. Their predominant periods read off in velocity response spectra in Figure 36 (c) are varied from $T = 0.26$ s to 2.5 s. Induced strains due to upward and downward waves, $\gamma_u(t,z)$ and $\gamma_d(t,z)$, have been calculated at different depths z in the 1D wave propagation analysis, respectively, from which cumulative strain energies $E_\gamma(z)$ are determined by the next equation derived from Eqs. (17) and (19).

$$E_\gamma(z) = \frac{1}{2} \rho V_s{}^3 \int_0^t \left\{ \left[\gamma_u(t,z) \right]^2 - \left[\gamma_d(t,z) \right]^2 \right\} dt \tag{58}$$

The energy E_γ thus calculated is plotted versus depth z with open symbols in Figure 37 to compare with the demand energy of close symbols of constant E_u along the depth z for the case of $D = 0\%$. If $D > 0\%$, the demand energy is the average of upward and downward energies, $(E_u + E_d)/2$ along z considering wave attenuation. Here, a quarter wavelength $\lambda/4$ calculated from the predominant period T as $\lambda/4 = V_s T/4$ for $V_s = 160$ m/s is indicated with a horizontal dash line for each earthquake. The quarter wavelength $\lambda/4$ tends to decrease along with equivalent linear V_s lowering with increasing soil nonlinearity. Furthermore, the damping ratio will also increase as $D = 0\%$, 20%, and 40%, for example, which shows the effect of damping on the strain energy E_γ, appearing insignificant in shallower depths as illustrated.
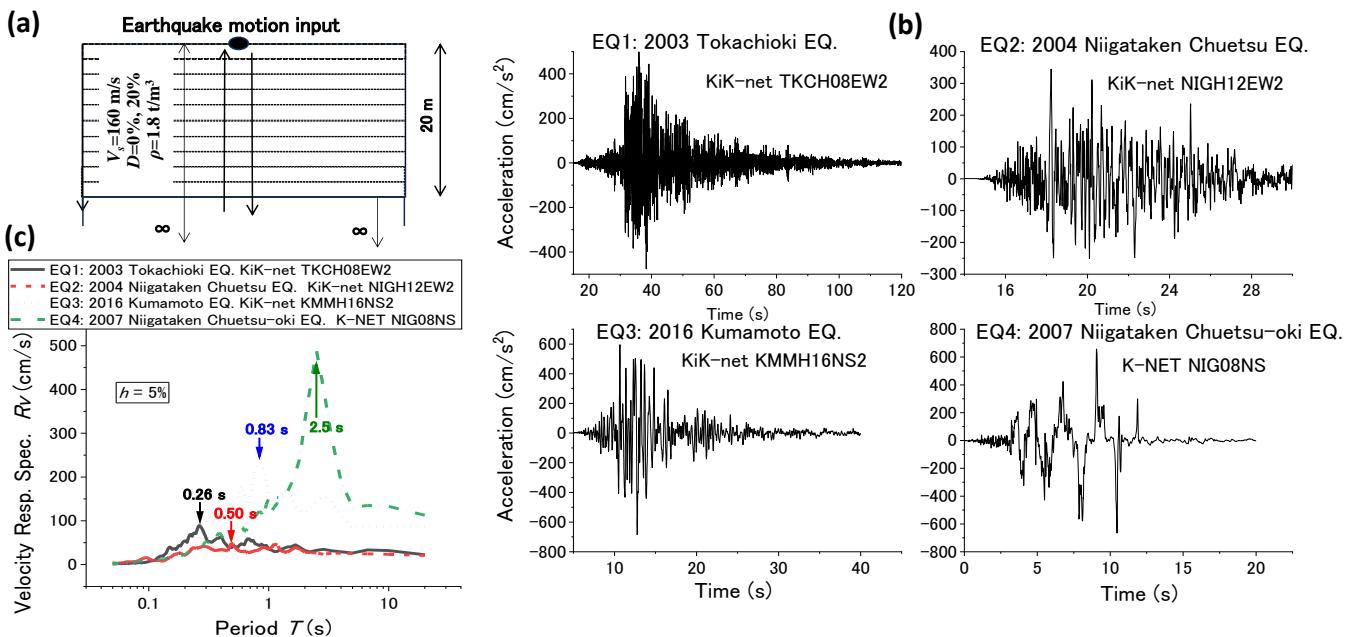
Figure 36. One-dimensional SH-wave propagation model and input motions: (a) Uniform 1-D soil model vibrated by surface input motions, (b) Acceleration time histories EQ1 to EQ4 given to soil model, and (c) Velocity response spectrums of 4 recorded earthquake motions.

According to Figure 37, the depth-dependent increase of E_γ seems variable among the four earthquakes: First, due to the difference in the characteristic wavelength; second, due to the wave irregularity. Nonetheless, the strain energy E_γ to compensate for the dissipated energy has been confirmed to start from zero at the ground surface, implying that liquefaction is difficult to occur near the surface as long as the SH-wave field is assumed. With increasing depth, E_γ tends to be nearly half of $(E_u+E_d)/2$ for the same D-value at the same depth but never goes far beyond.
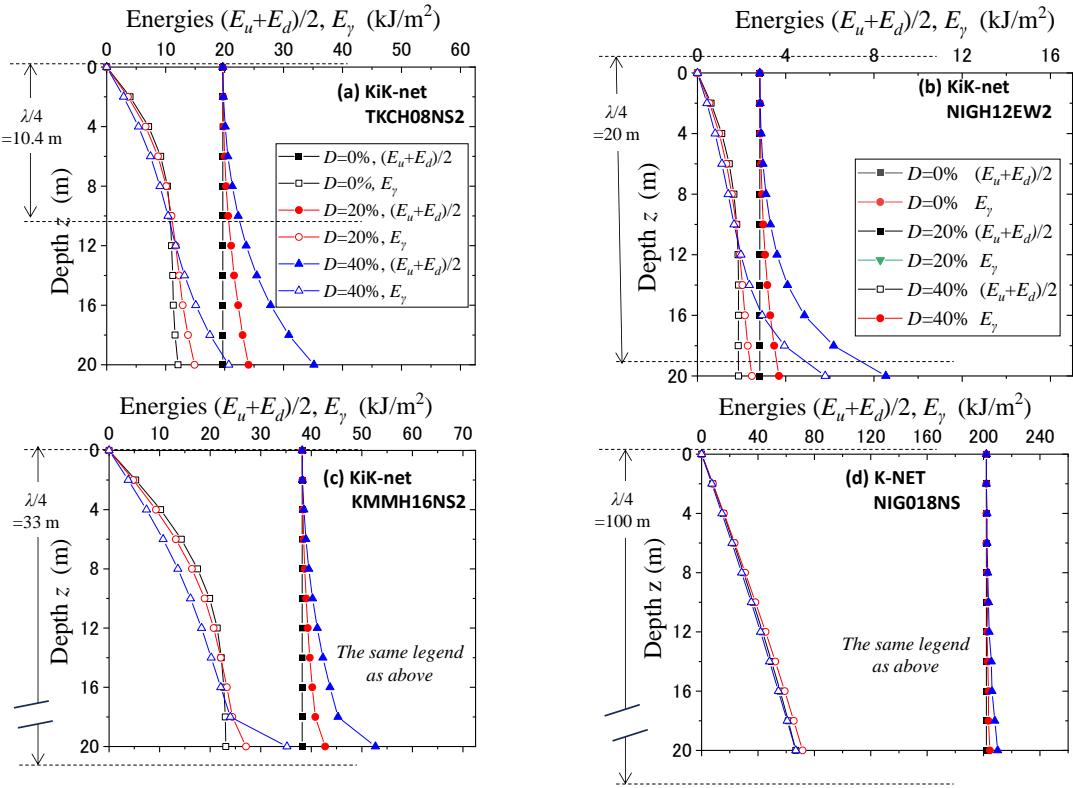
Figure 37. Depth-dependent distributions of strain energy E_γ and wave energy $(E_u+E_d)/2$ in 20 m–thick uniform layer calculated for different damping ratio D and 4 different surface earthquake motions (a), (b), (c), and (d).

Thus, as assumed for the harmonic motion in Figure 35 (b), the strain energy E_γ averaged over the depth of a quarter wavelength $\lambda/4$ cannot be larger than $1/2$ of the demand energy for strong earthquake motions causing soil nonlinearity. Hence, the simplification by Eq. (57) may be justified in determining the energy $E_u{}^*$ compensating for liquefaction-induced dissipated energy within the depth of a quarter-wavelength or any depth for normal liquefaction evaluations.

4.6. How to compare upward energy with dissipated energy

As mentioned, the key of the present EBM is that the upward wave energy is quantified and directly compared with the dissipated energy for liquefaction. The comparison should be made so that liquefaction occurs when the cumulative wave energy in the field attains the same amount of dissipated energy to liquefy the soil in laboratory cyclic loading tests.

In the laboratory test of a viscoelastic material in Figure 38 (a), shear stress $\tau = \tau_a \sin \omega t$ induces strain $\gamma = \gamma_a \sin(\omega t - \delta)$ with a phase-delay angle δ. The dissipated energy ΔW is formulated from the area of the $\tau \sim \gamma$ hysteresis loop ACDA'C'D'A as

$$\Delta W = \int \tau \, d\gamma = \omega \tau_a \gamma_a \int_0^{2\pi/\omega} \sin \omega t \cos(\omega t - \delta) \, dt = \tau_a \gamma_a \pi \sin \delta \tag{59}$$

Thus, the angle δ is a key parameter determining the dissipated energy during cyclic loading. In the same loading, twice the elastic strain energy $W = Area$ (OAB) $= Area$ (OA'B') is given to the

material. Of the energy $W = Area$ (OAB) in the first 1/2 cycle, the energy corresponding to $Area$ (ABC) can be recovered and recycled in the second 1/2 cycle filling $Area$ (A'B'C'). The $Area$ (ABC) is calculated as

$$Area(ABC) = \int \tau d\gamma = \omega \tau_a \gamma_a \int_{(\pi/2+\delta)/\omega}^{\pi/\omega} \sin \omega t \cos(\omega t - \delta) dt$$
$$= \Delta W \left[1 - 2(\pi/2 - \delta) D \right] / 4\pi D \tag{60}$$

Hence, the energy supply in one cycle loading denoted here as $2W_-$ considering the energy recycling by the $Area$ (ABC) is obtained as [23,37];

$$2W_- = \Delta W + Area(ABC) = \left[\Delta W + Area(ABCDA'B'C'D') \right] / 2$$
$$= (\Delta W / 4\pi D) \times \left\{ 3\pi D + 2D \tan^{-1}(2D) + 1 \right\} \tag{61}$$

Then, the ratio of the dissipated energy ΔW to the supplied energy $2W_-$ in one cycle is written as;

$$\Delta W / 2W_- = 4\pi D \Big/ \left\{ 3\pi D + 2D \tan^{-1}(2D) + 1 \right\} \tag{62}$$

In Figure 38 (b), the variation of the energy ratio $\Delta W/2W_-$ in Eq. (62) is shown versus the damping ratio D and compared with $\Delta E/E = 1 - e^{-4\pi D}$ in Eq. (45). The two curves on the chart are very similar to each other, both have the same initial tangent and tend to approach to the asymptote $\Delta W/2W_- = \Delta E/E = 1.0$ with increasing D [23]. This indicates that the energy dissipation mechanism during wave propagation is very similar for not only infinitely small but also large damping and reproduced by laboratory cyclic loading tests despite a small gap of a maximum of 10%. The gap may be attributed to the difference in loading mechanism; simultaneous cyclic loading on a whole soil specimen versus time-delayed loading on in situ soils during wave propagation [23].
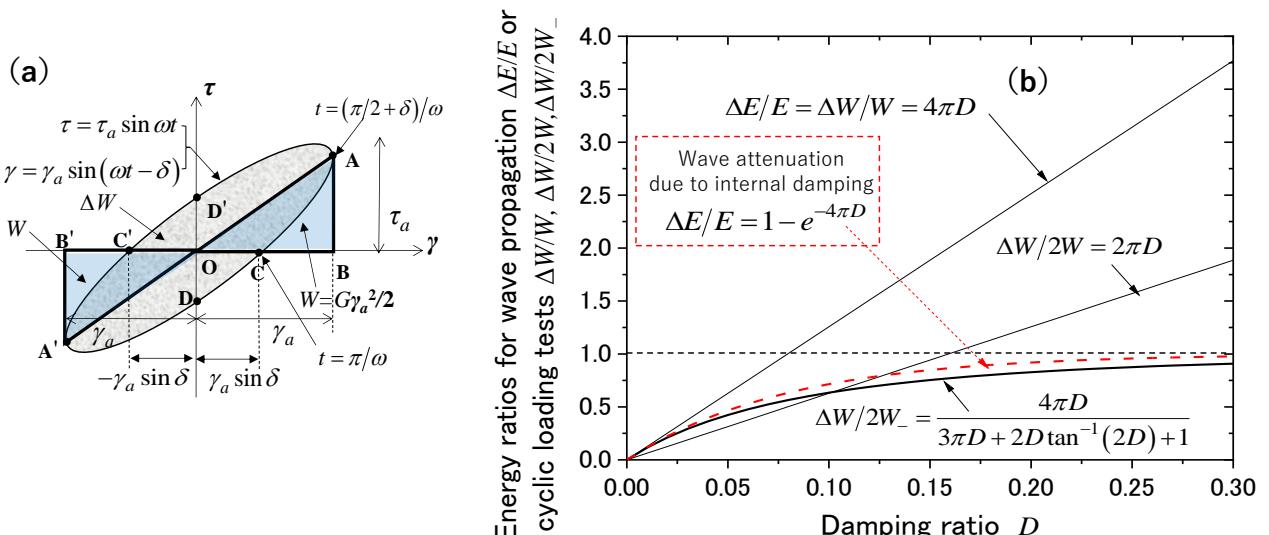
Figure 38. Schematic stress-strain hysteresis loop of ideal viscoelastic material (a), and $\Delta W/2W_- \sim D$ curve by cyclic loading compared with $\Delta E/E \sim D$ curve in wave propagation.

In conventional data reduction of cyclic loading tests, the elastic strain energy $W = Area$ (OAB) is normally employed to divide the dissipated energy ΔW, as $\Delta W/W$. Figure 36 (b) shows that the wave energy ratio $\Delta E/E = 1 - e^{-4\pi D}$ is represented very well by $\Delta W/W = 4\pi D$ when D is less than a few percent. This is because of the energy $2W$ supplied in one cycle, W is recycled without being dissipated on account of small damping D. With increasing D, $\Delta W/W = 2\pi D$ may become better to approximate $\Delta E/E$ (e.g. Kazama et al. [17]) though there is a distinctive difference from $\Delta E/E$. In contrast, Eq. (62) seems to successfully simulate the energy dissipation ratio during wave propagation for wide D-values as shown in Figure 38 (b).

The above formulation in one-cycle loading may be extended to a similar relationship for cumulative energies in liquefaction tests by multi-cycle loading if the damping ratio D can be approximated as a constant averaged over the whole developing process of liquefaction. We will demonstrate that the damping ratio stays $D = 0.1$ to 0.2 with the average $D = 0.15$ during liquefaction tests of saturated sands in Figure 39. Hence, the following equation may be valid in place of Eq. (62).

$$\sum \Delta W \Big/ \sum 2W_{-} \approx 4\pi D \Big/ \left\{ 3\pi D + 2D\tan^{-1}(2D) + 1 \right\} \tag{63}$$

Instead of the above equation where the soil is assumed ideally viscoelastic, the value $\sum\Delta W/\sum 2W_{-}$ may be calculated on actual soil materials using laboratory cyclic loading test data already addressed. Figure 39 (a) exemplifies a typical stress-strain relationship in the undrained cyclic triaxial test on saturated Futtsu sand. Namely, using the dissipated energy per cycle, $\Delta W = Area$ (ABCDA), and the energy corresponding to $Area$ (ABB'CDD'A) as well, the strain energy $2W_{-}$ supplied per cycle considering the recycling effect of elastic energy can be formulated as;

$$2W_{-} = \left[\Delta W + Area(\text{ABB'CDD'A}) \right] \Big/ 2 \tag{64}$$
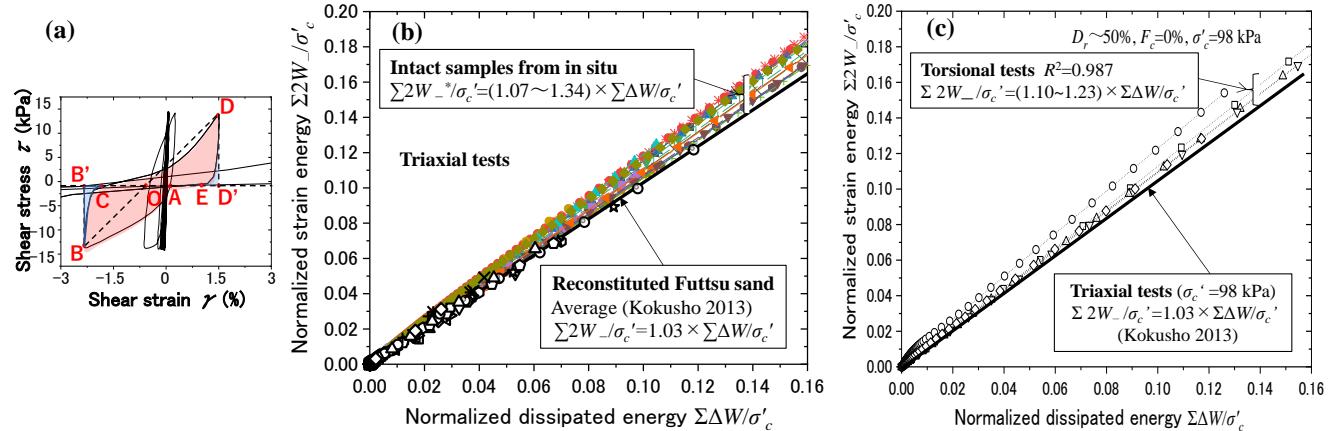
Figure 39. Typical stress-strain relationship in undrained cyclic loading triaxial test (a), and energy calculation results $\sum\Delta W/\sigma_c'$ versus $\sum 2W_{-}/\sigma_c'$ obtained by triaxial tests on intact samples (b), and by triaxial/torsional tests on reconstituted samples (c).

In Figures 39 (b) and (c), the cumulative energies $\sum 2W_{-}$ thus calculated are plotted versus the cumulative dissipated energy $\sum\Delta W$ ([31], JGS Committee Report 2018 [51]) from the 1st to the last

cycle in triaxial and torsional liquefaction tests, respectively. Note that the gradient of the plots, $(\Sigma 2W_-/\sigma'_c)/(\Sigma\Delta W/\sigma'_c)$, evaluates very similarly among the test results of different conditions; 1.03 for the reconstituted Futtsu sand, 1.07~1.34 for intact soils both tested in triaxial tests, and 1.10~1.23 for the Futtsu sand tested in torsional tests. Also noted is the evident proportionality of $\Sigma 2W_-$ to $\Sigma\Delta W$ in all the plots, indicating that the D-value in Eq. (63) is almost constant throughout the loading cycles as already assumed. This implies that the energy dissipation mechanism in soils will not significantly vary with the development of liquefaction.

The finding that the gradients $(\Sigma 2W_-/\sigma'_c)/(\Sigma\Delta W/\sigma'_c)$ read off from all the plots are near unity can lead to a simple result as $\Delta W = 2W_-$, so that the soils tend to dissipate almost all the energy supplied cycle by cycle throughout the liquefaction process during cyclic loading tests. Hence, it may be justified to make use of such simplification in the EBM of liquefaction evaluation as;

$$\sum \Delta W \Big/ \sum 2W_- \approx 1 \tag{65}$$

Thus, $\sum\Delta W/\sum 2W_- \approx 1$ in Eq. (65) and $E_u^*/E_u = 1/2$ in Eq. (57) are two essential formulas on energy ratios in the EBM of liquefaction evaluation developed here. Because the dissipated energy for liquefaction in the laboratory, $\sum\Delta W$, should be compared with the wave energy density E_u^*/λ available in situ, $\sum 2W_-$ has to be compared with $E_u/(2\lambda)$ in evaluating in situ liquefaction behavior. Consequently, E_u is to be compared with $2\times\sum 2W_-$ as already stated in the previous paper [18,23], which is denoted as $\sum W_-^* \equiv 2\times\sum 2W_-$ and also used in this paper hereafter.

5. Evaluation steps and examples of EBM

After visiting basic research findings on the energy-based method (EBM) for liquefaction evaluation in terms of capacity, demand, and their mutual comparison, it seems necessary to show practical steps to implement the EBM in engineering practice. Thus, the evaluation steps are as simplified and practical as possible, reliable, and presented and followed by some examples. Some of the equations and methods used here have been updated from previous publications by the author and his coworkers reflecting more recent research findings.

The evaluation steps of the current EBM [31] quantifying the upward wave energy as the energy demand are illustrated in Figure 40, composed of two stages. Stage-I comprises *Step-1* to *Step-6* to make a preliminary evaluation of the liquefaction potentials of individual layers. Stage-II comprising *Step*-7 to *Step*-10 is to make a higher-level liquefaction prediction including induced shear strains and settlements based on the results of Stage-I.
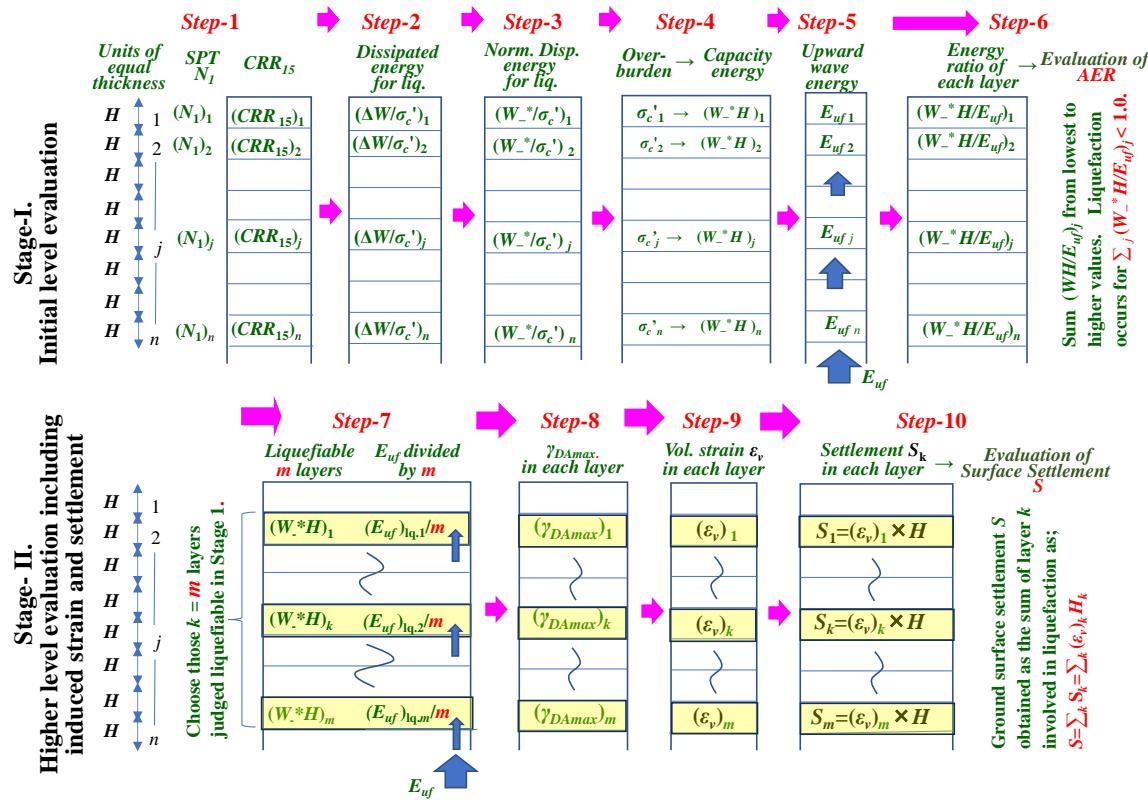
Figure 40. Energy-based liquefaction evaluation steps: Stage-I consisting of Step-1~6 for initial level evaluation by *AER*, and Stage-II consisting of Step-7~10 for higher level evaluations of max. shear strain γ_{DAmax} and ground settlement *S*.

5.1. Stage-I: Preliminary Evaluation Steps for Initial Liquefaction

Step-1:

At a given site, a soil profile is divided into layers of an identical thickness $H = 1$ to 2 m throughout the soil model following in situ penetration test data available. The *CRR*- values for an equivalent number of cycles N_L for the initial liquefaction in SBM, typically CRR_{15} for $N_L = 15$, are determined in individual layers based on the penetration resistances or other soil test data.

Step-2:

Normalized cumulative dissipated energy (abbreviated as dissipated energy hereafter) $\sum \Delta W/\sigma'_c$ for soil to attain the initial liquefaction (corresponding to maximum double amplitude axial strain $\varepsilon_{DA\max} = 5\%$ in triaxial tests or maximum double amplitude shear strain $\gamma_{DA\max} = 7.5\%$ in simple shear tests) is determined in each layer from *CRR*-value; such as CRR_{15} for $N_L = 15$;

$$\sum \Delta W/\sigma'_c = 2.7 \cdot (CRR_{15} - 0.1)^2 + 0.008 \tag{66}$$

Here, the dimension of $\Sigma \Delta W$ is energy per unit volume, and non-dimensionalized by effective confining stress σ'_c. Eq. (66) is identical to Eq. (5) developed from a series of triaxial liquefaction tests on intact soils of various properties. Thus, the correlation is available to uniquely determine the dissipated energy $\Sigma \Delta W/\sigma'_c$ corresponding to the initial liquefaction ($\varepsilon_{DA\max} = 5\%$ or $\gamma_{DA\max} = 7.5\%$)

regardless of earthquake motions from *CRR* in SBM for widely varying in situ soils irrespective of soil types [20].

Step-3:

The strain energy $\sum 2W_-$ considering the energy-recycling effect is identical to the dissipated energy $\sum \Delta W$ all through the liquefaction development as already given in Eq. (65) based on the cyclic loading test results shown in Figure 39. Because the upward energy compensating for the dissipated energy is approximated as half of the upward wave energy E_u in surface soils down to a quarter wavelength $\lambda/4$ (normally larger than 20m) as in Eq. (57), $\sum 2W_-/\sigma'_c$ is doubled in advance and denoted as $\sum W_-^*/\sigma'_c$ to directly compare with the demand energy E_u later on in *STEP*-6.

$$\sum W_-^* \big/ \sigma'_c = 2 \times \sum 2W_- \big/ \sigma'_c = 2 \times \sum \Delta W \big/ \sigma'_c \tag{67}$$

Step-4:

Energy capacity (energy per area in dimension) in a layer of thickness H is calculated as $\sum W_-^* H$ from Eq. (67) using $\sum \Delta W/\sigma'_c$ corresponding to the initial liquefaction, where $\sigma'_c = (1+2K_0)\,\sigma'_v/3$ is effective confining stress, K_0=earth-pressure coefficient at rest, and σ'_v =effective overburden.

Step-5:

The upward wave energy E_u (energy per area in dimension) is calculated from an equivalent linear one-dimensional SH-wave propagation analysis in a soil profile at a given site using $\dot{u}$ =particle velocity of upward wave, ρV_s =impedance of SH wave wherein the degradation of V_s due to soil nonlinearity is reflected, and energy at the end of motion E_{uf} is determined in each layer by integrating Eq. (68) or Eq. (21) in terms of time t.

$$E_{uf} = \rho V_s \int_0^t (\dot{u})^2 \, dt \tag{68}$$

For those sites where a design earthquake motion is unavailable, the energy E_{uf} may be roughly estimated by incorporating empirical formulas, Eqs. (26) to (29) as delineated. From earthquake magnitude M and focal distance R (unit: m) as well as the impedance ratio $\alpha = (\rho V_s)_m/(\rho V_s)_{sbr}$ between m-th layer and a seismological bedrock, the upward energy at a layer m, $(E_u)_m$ (unit: kJ/m^2), is determined using;

$$\beta = \alpha^{0.7}; \quad \alpha = (\rho V_s)_m \big/ (\rho V_s)_{sbr}, \quad \beta = (E_u)_m \big/ (E_u)_{sbr} \tag{69}$$

where the upward energy at the seismological bedrock $(E_u)_{sbr}$ (unit: kJ/m^2) is computed as;

$$(E_u)_{sbr} = E_{Total} \big/ (4\pi R^2) = 10^{1.5M+1.8} \big/ (4\pi R^2) \tag{70}$$

If the upward energy is estimated using these empirical equations, note that the ultimate upward energy E_{uf} equivalent to Eq. (68) at m-th layer should be halved as $E_{uf} = (E_u)_m/2$ to compare with the dissipated energy $\sum \Delta W$, because $(E_u)_{sbr}$ in Eq. (69) is evaluated as the sum of two horizontal directions while $\sum \Delta W$ is normally determined from soil tests by one-directional shearing.

Step-6:

The energy ratio $\sum W_-^* H/E_{uf}$ is calculated in each layer using the values $\sum W_-^* H$ and E_{uf} above. A layer with a smaller energy ratio has higher and earlier liquefaction potential than others among a given soil profile [18]. The energy ratios of individual layers are numbered sequentially starting from the

lowest ratio ($j = 1$) toward the higher ones and summed up in terms of j, which is named *AER* (Accumulated Energy Ratio).

$$AER = \sum_j \left(\sum W_-^* H / E_{uf} \right)_j \tag{71}$$

Liquefaction occurs in that sequence exclusively in those layers of $AER \leq 1.0$, because the upward energy can liquefy individual layers in the above sequence until it is completely dissipated by liquefaction. Thus, unlike the conventional Stress-Based Method, the EBM has the potential to decide the extent of liquefaction to be within the availability of the total energy demand. To make the most of this potential, the steps in Stage-II are taken for a higher-level liquefaction evaluation as below.

5.2. Stage-II: Steps for Strain and Settlement Evaluation

As mentioned, a remarkable feature of the present EBM is that the total energy demand for liquefaction can be prescribed at a site if a design earthquake is given. This will enable one to evaluate not only if liquefaction occurs or not but also if it occurs how large liquefaction-induced strain and settlement will develop.

This is possible in a simple case, where only a single layer has the potential to liquefy, to evaluate the induced strain by demand energy exclusively given there. In the case of multiple liquefiable layers, it may also become possible to calculate the strains if a rule is adopted on how the upward energy is shared among the layers. However, such a universal rule is never easy to establish because the energy distribution seems to be dependent on soil profiles, input seismic motions, and nonlinear soil properties. Sophisticated nonlinear effective stress analyses based on rigorous constitutive laws may provide the solution, though that is out of the scope of simplified and efficient liquefaction evaluations investigated here.

Instead of postulating the same induced strain of $\gamma_{DA} = 7.5\%$ corresponding to the initial liquefaction in all layers in Stage-I, a simple rule may be introduced in Stage-II that the wave energy is equally shared among those layers where liquefaction has been judged to occur ($AER < 1.0$) in Stage-I in Eq. (71) [31]. It may well be expected that this rule despite its simplicity will lead the evaluation not exactly but closer to actual behavior than Stage-I. Let us assume for example the number of liquefied layers in Stage-I as m, and count other sequential numbers for Stage-II from the top to the bottom of the soil layers, $k=1\sim m$, as indicated in Figure 40.

Maximum induced DA shear strain in one of the liquefiable layers k may be calculated assuming the proportionality to dissipated energy as;

$$\left(\gamma_{DA\max} \right)_k = 7.5\% \times \left(\left(E_{uf} \right)_k / m \right) \Big/ \left(\sum W_-^* H \right)_k \tag{72}$$

Here, $(\sum W_-^* H)_k$ = the energy capacity (determined by dissipated energy for the initial liquefaction) corresponding to $\gamma_{DAmax} = 7.5\%$, and $(E_{uf})_k/m$ = the energy demand (upward energy) allocated to the k-th layer among the m liquefiable layers. This equation stems from experimental observations such as in Figure 25 (b) or Figure 4 in cyclic torsional or triaxial tests using harmonic and earthquake motions [18,31] despite the data scatters between double amplitude shear strain γ_{DAmax} and dissipated energy $\sum \Delta W / \sigma_c'$. Thus, the uniqueness of energy in terms of induced strain seems valid regardless of different loading histories as a great merit of the energy-based evaluation.

The maximum strain γ_{DAmax} in Eq. (72) is accepted to be closely correlated with liquefaction-induced volumetric strain ε_v by many investigators (Silver and Seed (1971) [52], Tatsuoka et al. [53],

Nagase and Ishihara [54], Tsukamoto et al. [55]). Quite a lot laboratory test data are available for the volumetric strain by undrained cyclic loading. Among them, Ishihara and Yoshimine [56] simplified their data as a bilinear relationship between volume change ε_v and single or double amplitude maximum shear strain, γ_{max} or $\gamma_{DAmax} = 2\gamma_{max}$, schematically shown in Figure 41 (a), where ε_v is proportional with γ_{DAmax} up to the upper limit ε_{vmax} corresponding to $\gamma_{DAmax} = 20\%$ ($\gamma_{max} = 10\%$), and the volumetric strain in the vertical axis is normalized by the corresponding upper limit as $\varepsilon_v/\varepsilon_{vmax}$.

To evolve the ε_v versus γ_{DAmax} correlations to be more robust and applicable to in situ soils of various physical properties, the database [34] of in situ intact soils disseminated by PWRI is utilized. This consists of numerous cyclic triaxial liquefaction tests of intact soils sampled from various natural and manmade ground in liquefied areas during the 2011 Tohoku earthquake in Japan together with pertinent in situ test data mainly by Standard Penetration Test including N_1 (corrected blow counts for effective overburden 98 kPa), F_c (fines content), and G_c (gravel content). A multiple regression analysis for the volumetric strain ε_{vmax} corresponding to the maximum shear strain $\gamma_{DAmax} = 20\%$ by utilizing the database has yielded the following formula, though the determination coefficient $R^2 = 0.458$ is not high [31].

$$\varepsilon_{v\max} = 3.85 - 0.0562 \times N_1 + 0.0120 \times F_c + 0.0290 \times G_c \tag{73}$$

In Figure 41 (b), the values ε_{vmax} on the vertical axis are plotted versus N_1 and F_c horizontally in the three-dimensional diagram. The plots are projected on the two-dimensional plane of ε_{vmax} versus N_1, and compared with the star plots connected with solid lines for clean sand of $F_c = 0$, which are from a design chart [56] based on reconstituted clean sands for $\gamma_{max} = 10\%$ ($\gamma_{DAmax} = 20\%$). The two plots essentially share a similar trend of ε_{vmax} decreasing with increasing N_1-value, wherein the widely varying fines content in the natural soils ($F_c = 1\sim97\%$) obviously has a great influence.
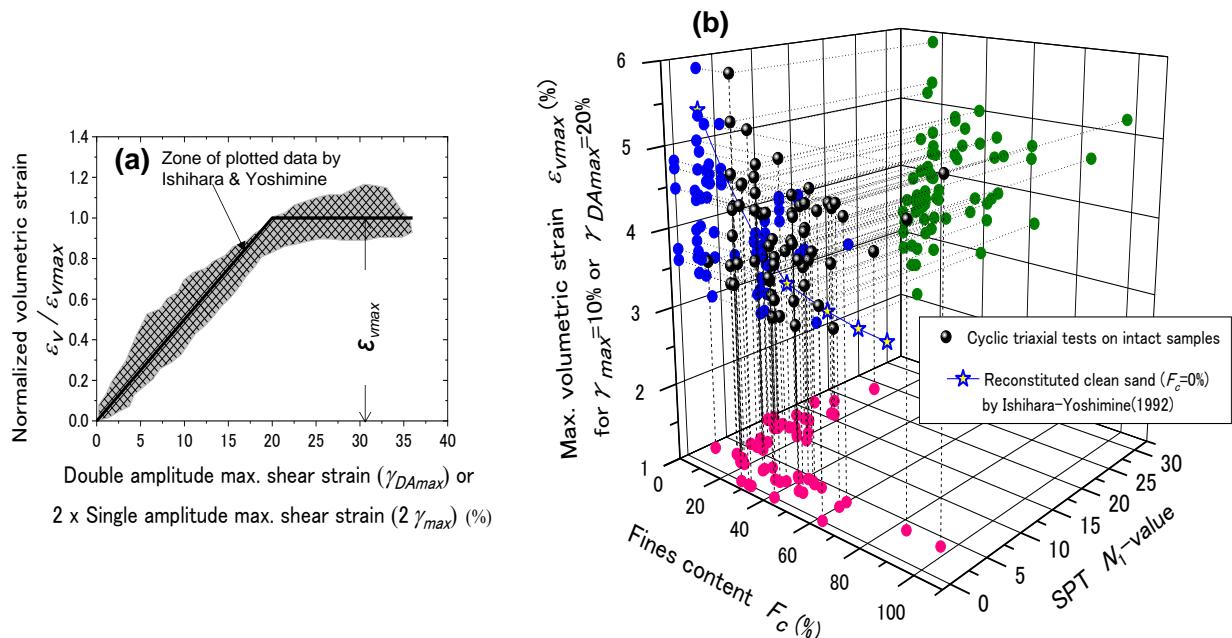
Figure 41. Conceptual correlation between volumetric strain & DA max. shear strain (a), and Max. volumetric strain ε_{vmax} versus SPT N_1 & fines content F_c by triaxial liquefaction tests on intact samples from in situ (b).

Based on the above test data and interpretations, the following steps to evaluate liquefaction-induced strains and settlements can be developed as Stage-II of the energy-based liquefaction evaluation procedure.

Step-7:

The upward energy at a base layer is divided by m (the number of liquefied layers in Stage-I), and the energy at a k-th layer $(E_{uf})_k /m$ comes up independently to layer k to be dissipated for liquefaction exclusively there.

Step-8:

The maximum induced shear strains assumed in Stage-I as $\gamma_{DAmax} = 7.5\%$ and identical in all those layers that were judged liquefiable are now recalculated in Eq. (72) to yield individually different $(\gamma_{DAmax})_k$-values caused by the allocated upward energy $(E_{uf})_k/m$ using the strain energy $(\Sigma 2W_{-}^*H)_k$ corresponding to the initial liquefaction. Consequently, the number of layers beyond the initial liquefaction ($\gamma_{DAmax}=7.5\%$) tends to be smaller because the equally-allocated upward energy tends to induce higher strain than $\gamma_{DAmax}=7.5\%$ in weaker layers, and lower strain in stronger layers. Thus, the higher-level liquefaction evaluation in Stage-II can be implemented differently from Stage-I, which may be more plausible in actual liquefaction performance.

Step-9:

Using the induced shear strains in individual liquefiable layers determined in the previous step, the corresponding volumetric strains ε_v are calculated in proportion to γ_{DAmax} if $\gamma_{DAmax} \leq 20\%$ as;

$$\left(\varepsilon_v \right)_k = \left(\varepsilon_{v\max} \right)_k \times \left(\gamma_{DA\max} \right)_k / 20\% \tag{74}$$

or a constant if $\gamma_{DAmax} > 20\%$.

$$\left(\varepsilon_v \right)_k = \left(\varepsilon_{v\max} \right)_k \tag{75}$$

where $(\varepsilon_{vmax})_k$ is determined in Eq. (73) in individual layers.

Step-10:

One-dimensional ground surface settlement S can be obtained as the sum of settlements in individual layers $k = 1 \sim m$ involved in liquefaction as;

$$S = \sum_k S_k = \sum_k \left(\varepsilon_v \right)_k H_k \tag{76}$$

Here, not only those beyond the initial liquefaction ($\gamma_{DAmax} > 7.5\%$) but also those before are involved in calculating the settlement as long as they are judged liquefiable in Stage-I.

5.3. Examples & case histories

Four soil models; one hypothetical uniform sand deposit and three case history sites liquefied and are evaluated using the EBM steps delineated above. The results are compared with those of the conventional stress-based method (SBM). The ground surface settlements in the case history sites are compared with the observation if available during the earthquakes.

5.3.1. Uniform sand model

A hypothetical uniform sand model 10 m thick with corrected SPT blow counts $N_1 = 8$ and $F_c = 0\%$, underlain by a stiff base shown in Figure 42 (a) was studied [18]. The cyclic resistance ratio corresponding to $N_1 = 8$ and $F_c = 0\%$ for the equivalent number of cycles $N_{eq} = 20$ is given by a Japanese design code (Japan Road Bridge Association [57]) as $CRR_{20} = (\gamma_{DAmax})_{triax.Neq=20} = 0.191$ determining the energy for the initial liquefaction $\Sigma\Delta W/\sigma'_c = 0.0372$ in Eq. (6). Due to the uniqueness of energy, CRR_{15} can be derived from Eqs. (5) and (6) as;

$$CRR_{15} = \sqrt{3.5/2.7}\left(CRR_{20} - 0.1\right) + 0.1 \tag{77}$$

$CRR_{15} = 0.204$ thus calculated is used hereafter in the SBM because $N_{eq} = 15$ is more widely accepted internationally than $N_{eq} = 20$ corresponding to $M = 7.5$ earthquakes.
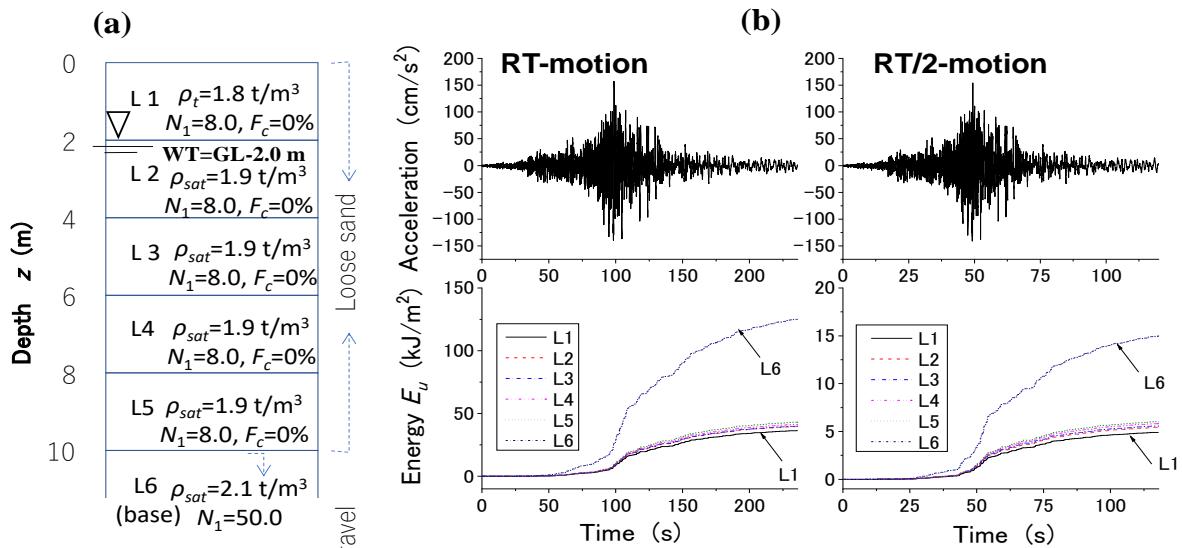
Figure 42. Soil profile of uniform sand model (a), and input surface accelerations (K-NET Urayasu EW) during the 2011 Tohoku earthquake ($M_J = 9.0$) and calculated upward wave energies for RT and RT/2-motions (b).

The soil conditions of the model are listed on the left side of Table 2. The model is sliced into 5 layers of $H = 2$ m thick, L1 to L5, with the top (L1) unsaturated and the rest saturated. The SPT N at each layer was calculated from $N_1 = 8$ using $N_1 = 1.7N/(\sigma'_v/p_0 + 0.7)$ [35] where σ'_v = effective overburden, p_0 = unit pressure, and the S-wave velocity V_s (m/s) was determined from the N-value using an empirical formula $V_s = 80\,N^{1/3}$ [57].

The dynamic ground response was calculated by an equivalent linear 1D response program [45] using the hyperbolic model (Hardin & Drnevich 1972 [58]) modified for better fitting to laboratory data [18]. The acceleration motion in Figure 42 (b) recorded at K-NET Urayasu (EW-direction) during the 2011 Tohoku earthquake in Japan (offshore subduction event of $M_W = 9.0$) was given to the model surface either in the real-time scale (RT: Duration 236 s) or in a compressed half time scale (RT/2: Duration 118 s) with the same acceleration amplitude. Note that the cumulative upward energy E_u and

its ultimate value at the end of earthquake E_{uf} calculated by Eq. (68) differs tremendously (8 to 1 ratio) between RT and RT/2 despite the same absolute accelerations as depicted in the bottom of (b).

In Table 2, Stage-I evaluations of EBM are shown together with Stage-II for the RT and RT/2-motions, where layers judged to liquefy are shaded in the columns (note that summations Σ for cumulative energy by cyclic loading in EBM are all abbreviated in the following tables). From the dissipated energy for liquefaction onset $\Sigma\Delta W/\sigma'_c = 0.0372$, the strain energy per unit volume is given as $\Sigma W_-^*/\sigma'_c = 0.0744$ from Eq. (67). The liquefaction energy capacities WH for $H = 2$ m thick layers to liquefy are calculated using the average confining stresses $\sigma'_c = \sigma'_v(1+2K_0)/3$, assuming the lateral earth-pressure coefficient at rest $K_0 = 0.5$. Energy ratio $\Sigma W_-^*H/E_{uf}$ is calculated in each layer using the values ΣW_-^*H and E_{uf} above, and summed up as $AER = \Sigma_i(\Sigma W_-^*H/E_{uf})_i$ in terms of i from the lowest ratio ($i = 1$) toward the higher ones in Eq. (71). In the RT-motion, all four saturated layers show AER-values below unity and hence liquefy in the EBM evaluation. In contrast, for the RT/2-motion, $\Sigma_i(\Sigma W_-^*H/E_{uf})_i < 1.0$ only for L2, indicating the upward energy is insufficient to liquefy more than that. Thus, a clear difference exists between the liquefaction potentials of the two input motions, reflecting the tremendous energy reduction in the RT/2-motion as mentioned before.

Table 2. Liquefaction evaluation by EBM, Stage-I & II, (compared with SBM) in a uniform sand model for RT & RT/2-motions.

Layer name / Depth (m) WT=GL-2 m	Density ρ (t/m³)	Corrected SPT N_1	S-wave vel.(m/s): $V_s=80N^{1/3}$	SBM $(\sigma_d/2\sigma_c')_{triax.}=CRR/[0.9\times(1+2K_0)/3]$, $N_1=15$, $K_0=0.5$	RT-motion $(\tau_{max}/\sigma_v')_{triax}=CSR/r_n$, $r_n=0.1(M-1)=0.8$, $M=9.0$	$F_s=CRR/CSR$ RT-motion $0.75\times(\sigma_d/2\sigma_c')_{triax.}/(\tau_{max}/\sigma_v')_{field}$	RT/2-motion $(\tau_{max}/\sigma_v')_{triax}=CSR/r_n$, $r_n=0.1(M-1)=0.65$, $M=7.5$	$F_s=CRR/CSR$ RT/2-motion $0.92\times(\sigma_d/2\sigma_c')_{triax.}/(\tau_{max}/\sigma_v')_{field}$	$\Delta W/\sigma_c'$	W_-^*/σ_c'	W_-^*H (kJ/m³)	RT Stage-I E_{uf} (kJ/m³)	W_-^*H/E_{uf}	AER	Liq. seq.	RT Stage-II E_{uf}/m m=4 (kJ/m³)	γ_{DAmax} (%)	$(\varepsilon_v)_{20\%}$ (%)	$\varepsilon_v\times H$ (cm)	RT/2 Stage-I E_{uf} (kJ/m³)	W_-^*H/E_{uf}	AER	Liq. seq.	RT/2 Stage-II E_{uf}/m m=4 (kJ/m³)	γ_{DAmax} (%)	$(\varepsilon_v)_{20\%}$ (%)	$\varepsilon_v\times H$ (cm)
L1 0-2	1.8	8	128																								
L2 2-4	1.9	8	140	0.204	0.188	0.81	0.182	1.03	0.0372	0.0744	4.37	39.7	0.110	0.110	1	9.9	17.0	3.40	5.79	5.42	0.81	0.81	1	5.42	9.3	3.40	3.16
L3 4-6	1.9	8	147	0.204	0.222	0.69	0.194	0.97	0.0372	0.0744	6.12	40.0	0.153	0.263	2	10.0	12.2	3.40	4.16	5.57	1.10	1.90	×	×	×	3.40	×
L4 6-8	1.9	8	154	0.204	0.234	0.65	0.205	0.92	0.0372	0.0744	7.88	41.4	0.190	0.454	3	10.3	9.9	3.40	3.35	5.83	1.35	3.26	×	×	×	3.40	×
L5 8-10	1.9	8	160	0.204	0.233	0.66	0.211	0.89	0.0372	0.0744	9.62	43.1	0.223	0.677	4	10.8	8.4	3.40	2.85	6.02	1.60	4.85	×	×	×	3.40	×
Base 10-	2.1	50	350											Settlement (cm) $\Sigma(\varepsilon_v\times H)_k$						16.2		Settlement (cm) $\Sigma(\varepsilon_v\times H)_k$						3.2

The corresponding SBM evaluation results on the same model are also listed in Table 2 in terms of a safety factor $F_s = CRR/CSR$. So far, the terms "CSR" and "CRR" have been defined to represent stress ratios between cyclic shear stress $\tau_d = \sigma_d/2$ and isotropic effective confining stress σ'_c considering laboratory soil tests on isotropically consolidated specimens as $CSR = (\sigma_d/2\sigma'_c)_{triax.}$ and $CRR = (\sigma_d/2\sigma'_c)_{triax.}$ for N_L, respectively. In calculating F_s in SBM, CRR has to be redefined as a ratio of cyclic shear stress to effective vertical stress $CRR = \sigma_d/\sigma'_v$ and further written as $CRR = 0.9 \times (1 + 2K_0)/3 \times (\sigma_d/2\sigma'_c)_{triax.}$, using the stress ratio obtained in isotropically consolidated cyclic triaxial tests $(\sigma_d/2\sigma'_c)_{triax.}$, and K_0=earth-pressure coefficient at rest, as well as a reduction constant 0.9 for horizontal two-directional shaking (Tokimatsu & Yoshimi 1983 [59]). The CSR is also redefined hereafter to represent the cyclic stress ratio of a given earthquake in the field $CSR = (\tau_d/\sigma'_v)_{field} = r_n \times (\tau_{max}/\sigma'_v)$ where $\tau_{max} =$ the maximum shear stress of an earthquake motion and σ'_v=effective overburden in the field. The index $r_n = \tau_d/\tau_{max}$ is a stress reduction coefficient empirically proposed as $r_n = 0.1 \times (M-1.0)$ [59] to convert maximum shear stress τ_{max} to equivalent shear stress τ_d of a harmonic motion of the equivalent number

of cycles $N_L=15$ using earthquake magnitudes M. The index r_n is correlated with Magnitude Scaling Factor used in North American practice; MSF, as $MSF = 0.65/[0.1(M-1)] = 0.65/r_n$, [28]. Hence, $r_n = 0.8$ and 0.65 correspond to $M = 9.0$ and 7.5 for the RT and RT/2-motion, respectively.

The results in the SBM and the EBM Stage-I (Step-1 to 6) l for the RT-motion do not look mutually contradictory in that all the saturated layers liquefy. For the RT/2-motion, however, only L2 liquefies in EBM because of the drastic reduction of upward energy from the RT-motion. In contrast, the SBM results are not markedly different between RT and RT/2 with only small increases in F_s. As an interesting trend generally observed in the comparison, liquefaction tends to occur more easily in shallower layers in EBM, while vice versa in SBM in the uniform soil model.

Hereafter, the EBM can evaluate the maximum strain γ_{DAmax} in Steps 7 and 8 of Stage II as listed in bold letters in the columns of strain evaluation in Table 2. In the RT-motion, where the four layers liquefied in Stage-I, the upward wave energy is equally divided by $m = 4$, from which γ_{DAmax} can be calculated in each layer by Eq. (72) as 17.0% ~ 8.4% and beyond 7.5% of liquefaction onset. Note that the strain tends to be higher in weaker layers where liquefaction occurs earlier in the sequence. For the RT/2-motion where L2 is a single layer to liquefy, the strain can easily be determined as 9.3% because all the wave energy is exclusively consumed there.

Based on the strain evaluated above, the 1D surface settlement is computed by following Step-9 and 10 in the settlement evaluation columns with bold letters. The upper limit strain ε_{vmax} is determined as 3.40% from Eq. (73) for $N_1 = 8.0$, $F_c = G_c = 0$, and the volumetric strains ε_v are calculated from γ_{DAmax} in individual layers by Eqs. (74) or (75). Then, they are multiplied by the layer thickness $H = 2$ m and summed up to determine the surface settlement S in Eq. (76). Eventually, the settlements $S = 16.2$ cm and $S = 3.2$ cm are obtained for the RT and RT/2-motion, respectively, which are widely varied despite the same acceleration. Thus, the EBM proposed here highlights a significant impact of wave energy or frequency content of earthquake motions other than acceleration intensity on the liquefaction-induced settlement without resorting to sophisticated effective stress numerical analyses.

5.3.2. Liquefaction case of loose sand fill by small PGA earthquake

A gently inclined farmland artificially filled with loose volcanic sandy soil liquefied and fluidized, leaving surface depression behind as shown in the photographs of Figure 43 (a) in Kitami city in Hokkaido, Japan, during the 2003 Tokachi-oki earthquake ($M = 8.0$) [27]. The site was 230 km from the hypocenter of the offshore subduction earthquake, and the maximum acceleration near the site was only 0.056 g.
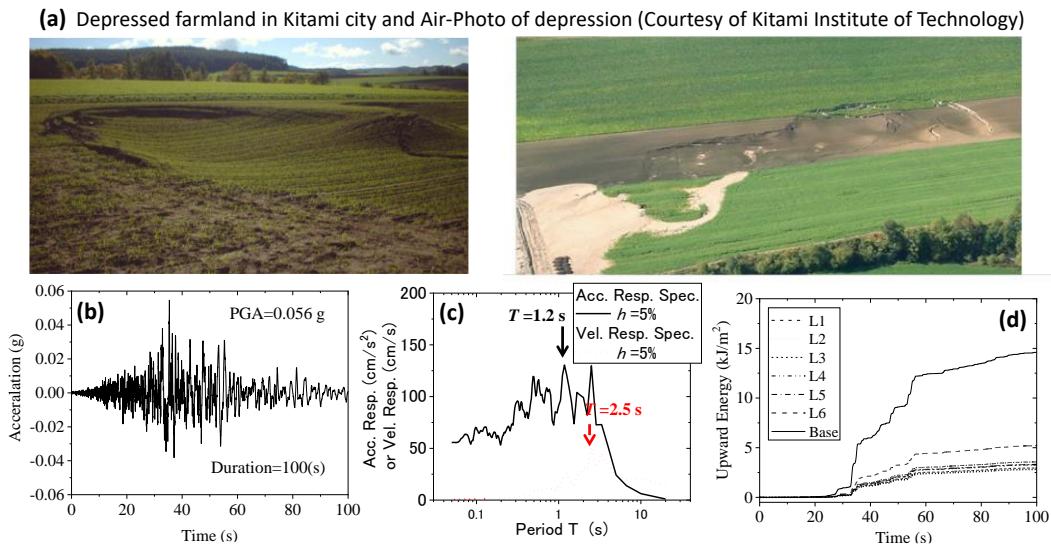
Figure 43. Liquefaction of filled farmland in Kitami city, Hokkaido, Japan during 2003 Tokachi-oki earthquake: a) Photographs of surface depression, (b) Acceleration records (K-NET Kitami EW), (c) Acc/Vel-response spectra, and (d) Calculated upward energies of different layers at P7.
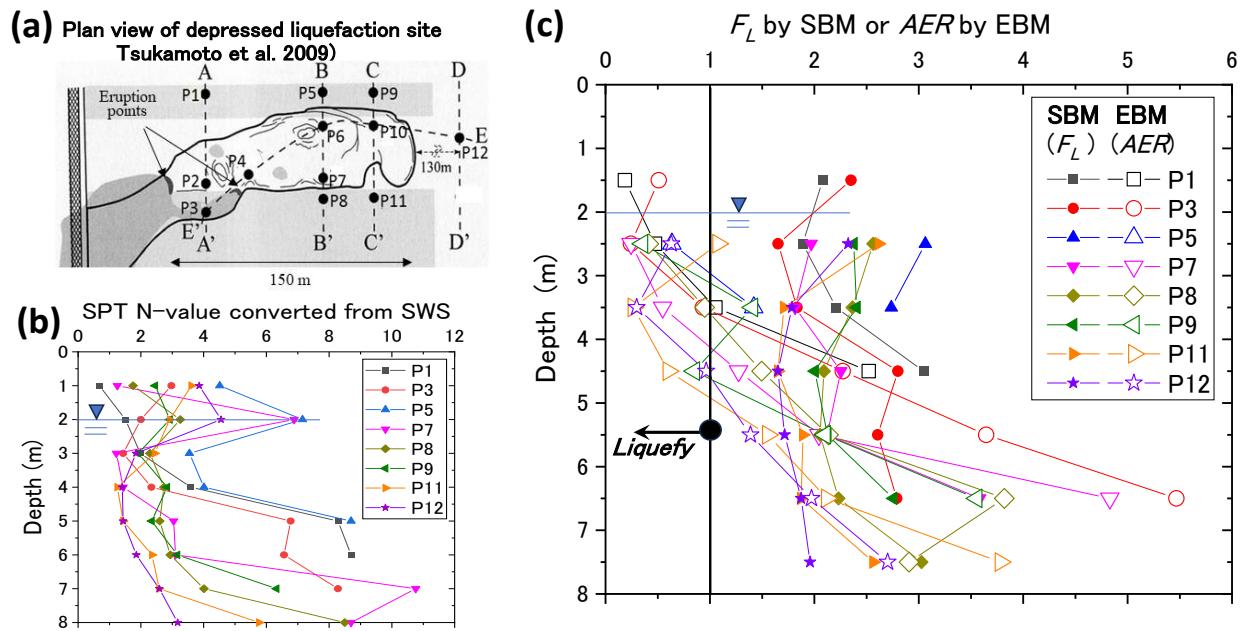
Figure 44. Soil investigation points in liquefied sand fill at Kitami- city (a), Investigation results (b), and Comparison of FL by SBM with AER by EBM along the ground depth (c).

The strange liquefaction with underground fluidization seems to have occurred along an old shallow valley filled with sand relatively thick, 4~7 m, and the water table was GL. −1~−2 m [23,27]. The upslope portion of the farmland, 200 m long and 50 m wide, was depressed by 3.5 m maximum, but the ground surface remained intact with marginal fissures and no sand boils there. On the downslope side, the boiled sand erupted collectively at several ejection holes and flowed 1 km away

along a ditch. Figures 44 (a) and (b) show in situ soil investigation points P1 to P12, and depth-dependent SPT N-values converted from SWS (Swedish Weight Sounding) carried out there after the earthquake. The sandy fill contained 33% non-plastic fines with the mean grain size $D_{50} = 0.02$ mm.

In Table 3, representative soil models at the two points, P1 and P7, are tabulated. The liquefiable sand fill was sliced into 5–7 layers 1 m thick each with soil density $\rho_{sat} = 1.8$ t/m^3. The converted SPT N-values in individual layers were corrected to N_1 corresponding to effective overburden stress $\sigma'_v = 98$ kPa using $N_1 = 1.7N/(\sigma'_v / p_0 + 0.7)$, and the S-wave velocity V_s (m/s) was determined from a corresponding N-value using $V_s = 80\ N^{1/3}$.

The weak acceleration motion with a long duration of more than a hundred seconds in Figure 43 (b) recorded at K-NET Kitami (EW-direction), 10 km far from the site, was given at the surface of the soil model. The velocity response spectrum in (c) indicates a very long predominant period of about 2.5 s presumably due to the large magnitude of M_J=8.0 earthquake and long hypocenter distance R=230 km. Figure 43 (d) exemplifies upward energies calculated at Point 7 in the one-dimensional equivalent linear analysis, which merely exceeds a few kJ/m^2 in the fill.

In the SBM, values of $N_L = 15$ were first determined from CRR_{20} in the design code [57] using N_1 and F_c listed in Table 3. It was converted to the corresponding dissipated energy for the initial liquefaction $\sum \Delta W / \sigma'_c$ using Eq. (5) for EBM, and the normalized strain energy $\sum W_-^* / \sigma'_c$ was calculated from it by Eq. (67) in each soil layer. The liquefaction energy capacity $W_-^* H$ for $H = 1$ m thick soil layer to liquefy was calculated using corresponding average confining stress $\sigma'_c = \sigma'_v (1 + 2K_0)/3$, assuming the earth-pressure coefficient at rest K_0 is 0.5.

Table 3 compares the liquefaction potentials of EBM with those of SBM at P1 (a) and P7 (b). In the EBM, liquefaction is to occur from the groundwater level GL-1 to -2 m down to GL -3 to -4 m at P1 and P2, respectively, as shaded in the table columns. Moreover, the liquefaction potential is higher (*AER* is smaller) for shallower soils as seen in the uniform sand layer. In contrast, F_L-values in SBM (for two stress reduction coefficients $r_n = 0.65$ for $M = 7.5$ as a default value and 0.70 for the 8.0 earthquake, respectively) are considerably larger than 1.0 at all depths both for $r_n = 0.65$ and 0.70 predicting no possibility of liquefaction at all.

Table 3. Soil models for Liquefaction evaluation by EBM (Stage-I) compared with SBM in farmland in Kitami city, Hokkaido, Japan during the 2003 Tokachi-oki earthquake.

$CRR_{15} = \sqrt{3.5/2.7}\,(CRR_{20}-0.1)+0.1$ $\Delta W/\sigma_c' = 2.7\cdot\left[(\tau_d/\sigma_c')_{lab}-0.1\right]^2+0.008$ Summation Σ for ΔW, W_* is abbreviated in EBM.

(a) Point 1

Depth (m)	Layer	Eff. overburden σ_v' (kPa)	$\sigma_c'=2\sigma_v'/3$ (kPa)	SPT-N	SPT-N_1	Fines content F_c (%)	$R_{L20}=(\sigma_d/2\sigma_c')_{lab}$ from N_1, $F_c=33\%$	$R_{L15}=(\sigma_d/2\sigma_c')_{lab}$ $=CRR_{15}/[0.9\times(1+2K_0)/3]$	$(\tau_{max}/\sigma_v')_{field}=CSR/r_n$ $r_n=0.1(M-1)=0.65$, $M=7.7$	$F_s = CRR/CSR=0.92\times$ $(\tau_d/\sigma_c')_{triax.}/(\tau_{max}/\sigma_v')_{field}$	$(\tau_{max}/\sigma_v')_{field}=CSR/r_n$ $r_n=0.1(M-1)=0.70$, $M=8.2$	$F_s = CRR/CSR=0.86\times$ $(\tau_d/\sigma_c')_{triax.}/(\tau_{max}/\sigma_v')_{field}$	$\Delta W/\sigma_c'$	W_*/σ_c'	W_*H (kJ/m³)	E_{uf} (kJ/m²)	W_*H/E_u (%)	Liq. Sequence	AER (%)
0–1	L1	17.7	11.8	0.7	1.3	33													
1–2	L2	25.5	17.0	1.5	2.7	33	0.154	0.162	0.0668	2.22	0.0668	2.08	0.0182	0.0365	0.62	3.32	19	1	19
2–3	L3	33.3	22.2	2.0	3.2	33	0.166	0.175	0.0795	2.02	0.0795	1.89	0.0231	0.0463	1.03	3.58	29	2	47
3–4	L4	41.2	27.5	3.6	5.4	33	0.206	0.220	0.0856	2.37	0.0856	2.21	0.0470	0.0940	2.58	4.46	58	3	105
4–5	L5	49.0	32.7	8.3	11.7	33	0.290	0.317	0.0892	3.27	0.0892	3.05	0.1346	0.2692	8.80	5.99	147	4	252

(b) Point 7

| Depth (m)	Layer	Eff. overburden σ_v' (kPa)	$\sigma_c'=2\sigma_v'/3$ (kPa)	SPT-N	SPT-N_1	Fines content F_c (%)	R_{L20}	R_{L15}	$(\tau_{max}/\sigma_v')_{field}$ $M=7.5$	F_s $M=7.5$	$(\tau_{max}/\sigma_v')_{field}$ $M=8.0$	F_s $M=8.0$	$\Delta W/\sigma_c'$	W_*/σ_c'	W_*H (kJ/m³)	E_{uf} (kJ/m²)	W_*H/E_u (%)	Liq. Sequence	AER (%)
0–2	L1	35.3	23.5	6.9	11.0	33													
2–3	L2	43.1	28.8	1.2	1.8	33	0.134	0.139	0.0606	2.11	0.0606	1.97	0.0121	0.0242	0.70	2.84	25	1	25
3–4	L3	51.0	34.0	1.4	2.0	33	0.139	0.144	0.0682	1.94	0.0682	1.82	0.0132	0.0265	0.90	2.98	30	2	55
4–5	L4	58.8	39.2	3.0	4.0	33	0.180	0.191	0.0727	2.42	0.0727	2.26	0.0305	0.0610	2.39	3.29	73	3	128
5–6	L5	66.7	44.5	3.1	3.8	33	0.177	0.188	0.0758	2.28	0.0758	2.13	0.0289	0.0577	2.57	3.34	77	4	204
6–7	L6	74.5	49.7	10.8	12.5	33	0.299	0.327	0.0781	3.85	0.0781	3.60	0.1469	0.2939	14.60	5.24	279	5	483

Figure 44 (c) depicts liquefaction potentials *AER* by EBM and F_s by SBM ($r_n = 0.70$ for the $M_J = 8.0$ earthquake) directly compared at multiple points near the periphery of the subsided zone. Obviously, liquefaction is very unlikely to occur at all the points according to SBM, while it is highly probable in EBM at shallower depths beneath the water table. The fundamental reason for this gap seems to rest on very small PGA (only 5% of *g*) versus non-negligible energy demand due to long predominant period and long duration as indicated in Figure 43 (b) to (d).

Thus, this liquefaction case study suggests better applicability of EBM to a large-magnitude far-field earthquake, in which the acceleration was too small to be accountable for the liquefaction onset by adjusting the coefficient in SBM. In contrast, the seismic wave energy was sufficient to liquefy sands in EBM because of the long duration and predominant period of the ground motion.

### 5.3.3. Takasu elementary school during the 2011 Tohoku earthquake

During the 2011 Tohoku earthquake (*M* = 9.0), reclaimed areas along Tokyo Bay, Japan, more than 350 km from the offshore causative fault, underwent widespread liquefaction. Takasu Elementary School in Urayasu City, Chiba prefecture, was focused as one of the typical study sites [27], where extensive liquefaction occurred and induced large subsidence accompanying huge sand boils of more or less 10 centimeters thick as photographed in Figure 45 (a). The soil consisted of landfill (B1, B2), hydraulic fill (F), alluvial sand (As1, As2), and clay (Ac, Nac) underlain by stiff gravelly base Dg at GL-43.7 m as illustrated in Figure 45 (b) together with their layer-by-layer soil properties. Fines contained in the soils in large percentages are assumed here to be non-plastic, because the ejecta coming out from the liquefied layers contained lots of fines that were non-plastic; however, according to some soil investigation reports before the earthquake, the plasticity of in situ fines were very spatially variable (Kokusho et al. 2014 [60], Kokusho 2015 [61]).

Figure 45 panel (b) soil profile table:

Depth (m)	Thick-ness (m)	Soil type	SPT N-value	Eff. Over-burden σ_v' (kN/m²)	N_1	S-wave vel. V_s (m/s) (Initial)	Density ρ_t (t/m³)
0.00	1.5	B1	6.0	13.2	12.3	145	1.80
1.50 (WT=GL 1.5 m)	2.2	B2	1.8	35.1	3.0	98	1.80
3.70	3.0	F	1.0	52.6	1.4	100	1.60
6.70	9.3	As1-1	8.6	93.6	9.2	160	1.90
14.00 (Seism.)	2.0	As1-2	8.6	102.4	8.7	160	1.90
16.00	19.7	Ac	0.9	192.6	0.6	140	1.60
35.70	3.0	As2	9.1	263.8	4.7	160	1.90
38.70	5.0	Nac	4.1	293.0	2.0	180	1.65
43.70	Base	Dg	50.0			350	2.00

Figure 45. Photographs of liquefaction of Takasu elementary school & soil settlement (a), Soil profiles (b), and input acceleration & upward energies (c).

Table 4. Liquefaction evaluation by EBM (compared with SBM), induced strain and settlement at Takasu elementary school liquefied site.

Depth (m)	Layer	Eff. overburden σ_v' (kPa)	SPT-N_1	Fines content F_c (%)	$(\sigma_d/2\sigma_c')_{triax.} = CRR / [0.9 \times (1+2K_0)/3], N_L=15, K_0=0.5$	$(\tau_{max}/\sigma_v')_{field} = CSR/r_n$, $r_n=0.1(M-1)=0.8, M=9.0$	$F_s = CRR / CSR = 0.75 \times (\sigma_d / 2\sigma_c')_{triax.} / (\tau_{max}/\sigma_v')_{field}$	$\Delta W/\sigma_c'$	$W\text{-}^*/\sigma_c$	$W\text{-}^* H$ (kJ/m³)	E_{uf} (kJ/m²)	$W\text{-}^* H/E_{uf}$	AER	Liquefaction sequence	E_{uf}/m, m=11 (kJ/m²)	γ_{DAmax} (%)	ε_v (%) for $\gamma_{DAmax}=20\%$	$\varepsilon_v \times H$ (cm)
					SBM (r_n=0.80)			EBM (H=1 m): Summation Σ for ΔW, W-* is abbreviated in EBM.										
								Stage-1							Stage-2			
								Liquefaction potential							Strain		Settlement	
GL: 0 m																		
1.00	B1																	
WT= GL-1.5 m 2.00	B2	30.4	3.0	52	0.2784	0.259	0.81	0.0939	0.188	3.81	36.81	0.103	0.513	8	3.35	6.6	4.31	1.42
3.00		38.2	3.0	52	0.116	0.259	0.34	0.0087	0.017	0.44	36.81	0.012	0.012	1	3.35	56.6	4.31	4.31
4.00		45.5	1.4	95	0.1696	0.314	0.41	0.0211	0.042	1.28	29.98	0.043	0.089	3	2.73	16.0	4.91	3.93
5.00	F	51.4	1.4	95	0.1956	0.314	0.47	0.0327	0.065	2.24	29.98	0.075	0.216	5	2.73	9.1	4.91	2.24
6.00		57.3	1.4	95	0.1684	0.314	0.40	0.0206	0.041	1.57	29.98	0.053	0.141	4	2.73	13.0	4.91	3.19
7.00		64.0	9.2	23	0.309	0.329	0.70	0.1259	0.252	10.75	64.71	0.166	1.228	13	×	×	×	×
8.00		72.9	9.2	23	0.3971	0.329	0.90	0.2463	0.493	23.93	64.71	0.370	1.866	15	×	×	×	×
9.00		81.7	9.2	23	0.2764	0.329	0.63	0.0920	0.184	10.02	64.71	0.155	0.898	11	5.88	4.4	×	0.80
10.00	As1-1	90.5	9.2	23	0.2415	0.329	0.55	0.0620	0.124	7.49	64.71	0.116	0.743	10	5.88	5.9	×	1.06
11.00		99.3	9.2	23	0.3136	0.329	0.71	0.1311	0.262	17.37	64.71	0.268	1.497	14	×	×	×	×
12.00		108.2	9.2	23	0.21	0.329	0.48	0.0407	0.081	5.87	64.71	0.091	0.307	6	5.88	7.5	×	1.36
13.00 Seismo-meter		117.0	9.2	52	0.2212	0.329	0.50	0.0476	0.095	7.43	64.71	0.115	0.627	9	5.88	5.9	×	1.17
14.00 GL-14 m		125.8	9.2	52	0.2431	0.329	0.55	0.0633	0.127	10.61	64.71	0.164	1.062	12	×	×	×	×
15.00	As1-2	134.6	8.7	52	0.2024	0.390	0.39	0.0363	0.073	6.52	63.57	0.103	0.409	7	5.78	6.6	×	1.32
16.00		143.5	8.7	52	0.135	0.390	0.26	0.0113	0.023	2.16	63.57	0.034	0.046	2	5.78	20.0	×	3.99
															Settlement (cm) $\Sigma (\varepsilon_v \times H)_k$			24.8

An equivalent linear one-dimensional SH-wave propagation analysis was carried out using V_s-logging data and a downhole acceleration record in the EW direction at 14 m below the ground surface provided by the Earthquake Research Institute, the University of Tokyo [27]. As depicted in Figure 45 (c), the recorded peak acceleration was 0.096 g downhole, and the upward wave energy calculated

based on the SH-wave propagation analysis was E_{uf}=146 kJ/m^2 in the gravelly base layer at the end of the major motion.

Table 4 shows the EBM liquefaction evaluation compared with SBM in the top 16 m soils from the ground surface, comprising 16 layers of $H = 1$ m each (with the top layer unsaturated), together with pertinent parameters such as N_1-values and fines content F_c, from which $(\sigma_d/2\sigma'_c)_{triax.}$ for $N_L = 15$ was determined using [57], and the dissipated energy $\Sigma\Delta W/\sigma_c'$ was further derived from it by Eq. (5).

The layers with AER smaller than 1.0 in EBM Stage-I and F_s smaller than 1.0 in SBM are judged liquefiable and shaded in the table. The SBM employing $r_n = 0.80$ for the $M = 9.0$ earthquake estimates all the saturated layers to liquefy, while the EBM Stage-I predicts not all but quite many layers belonging to hydraulic fill (F), B2, and As1 to liquefy.

Following the EBM results obtained in Stage I, induced strains are evaluated in the EBM Stage-II. As the total number of layers to liquefy is $m = 11$ in Step-6, the upward energies allocated to individual layers are 1/11 of the total energy, from that the maximum induced shear strain γ_{DAmax} can be determined in Eq. (72) as listed in the right of Table 3 with bold letters. The induced strains γ_{DAmax}, assumed as 7.5% in all the liquefied layers in Stage-I, are recalculated quite differently, as a maximum of 56.6% to a minimum of 4.4%. Consequently, the number of layers beyond the initial liquefaction (γ_{DAmax}>7.5%) reduces to 6 (fewer than 11 in Stage-I) as a result of strain concentration in fewer layers, which is seemingly closer to actual liquefaction behavior than Stage-I.

Maximum volumetric strains ε_v are calculated by Eq. (74) as tabulated in Table 3 following Step-9 using $\varepsilon_{vmax} = 3.61 \sim 4.91\%$ determined by Eq. (73) according to N_1 and F_c (G_c can be assumed to be 0) in those layers, which were judged to liquefy in Stage-I. In one layer with $\gamma_{DAmax} = 56.6\%$ exceeding the upper strain limit $\gamma_{DAmax} = 20\%$, ε_v is calculated by Eq. (75). Then, the ground surface subsidence can be obtained in Eq. (76) as the sum of settlements of individual layers of thickness H=1.0 m. Here, not only those beyond the initial liquefaction (γ_{DAmax}>7.5%) but also those before are involved in calculating the subsidence if they have been judged liquefiable in Stage-I.

The calculated subsidence of 24.8 cm at the bottom of Table 3 seems to be smaller than the soil settlement, which was around 40 cm observed by the present author during his reconnaissance at a pile-supported building of the Takasu elementary school as photographed in Figure 45 (a). However, the difference between the two values may probably be narrowed because the ejecta in large volumes (more or less 10 cm thick on average) will help increase the ground subsidence, which is defined solely in Eq. (76) from the volume contraction by undrained cyclic loading.

5.3.4. Maihama Ni-Chome during the Tohoku earthquake

In another liquefied site during the same Tohoku earthquake, Maihama Ni-Chome, also in a reclaimed area of Urayasu City (Azuno & Kokusho 2020) [62], the soil consisted of landfill (B), hydraulically reclaimed clay and sand (Rc, Rs), alluvial sand (As, with high silt content in the lower part), and alluvial clay (Ac1, Ac2), underlain by stiff gravelly base layer at GL.-51 m, as illustrated in Figure 46 (a). The acceleration motion in (b) was obtained by deconvoluting a record a few km distant at a KIK-NET Urayasu station (EW) (NIED 2021 [63]), and given at the base layer of this site. The equivalent linear SH-wave propagation analysis was conducted to calculate dynamic shear stress τ_d, CSR and upward energies E_u as depicted in the bottom of (b) at different levels of the soil profile.
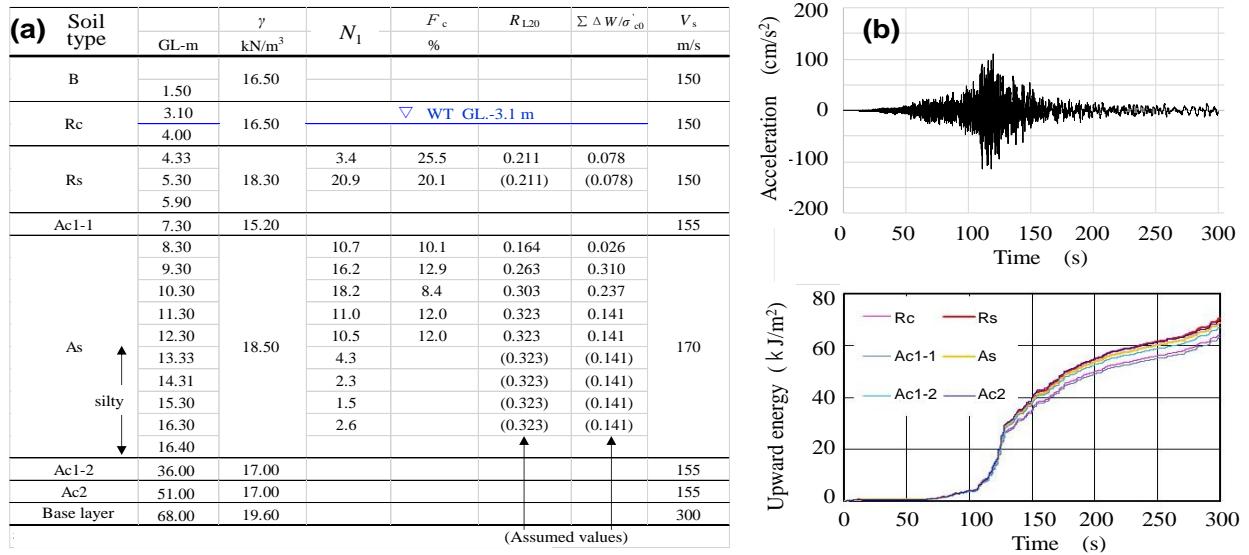
Figure 46. Soil profiles (a), and input acceleration and upward energies (b), at Maihama Ni-Chome liquefied site.

Table 5. Liquefaction evaluation by EBM (compared with SBM), induced strain and settlement at Maihama Ni-Chome liquefied site.

Depth (m) GL: 0 m	Layer	Eff. overburden σ_v' (kPa)	SPT-N_1	Fines content F_c (%)	$(\sigma_d/2\sigma_c')_{triax} = CRR / [0.9\times(1+2K_0)/3]$, $N_L=15$, $K_0=0.5$	$(\tau_{max}/\sigma_v')_{field}=CSR/r_n$, $r_n=0.1(M-1)=0.8$, $M=9.0$	$F_s = CRR/CSR = 0.75\times(\sigma_d/2\sigma_c')_{triax}/(\tau_{max}/\sigma_v')_{field}$	$\Sigma\,\Delta W/\sigma_c'$	$\Sigma\,W^*/\sigma_c'$	$\Sigma\,W^*H$ (kJ/m³)	E_{uf} (kJ/m²)	$\Sigma\,W^*H/E_{uf}$	AER	Liquefaction sequence	E_{uf}/m, $m=11$ (kJ/m²)	$\gamma_{D,Amax}$ (%)	ε_v (%) for $\gamma_{D,Amax}=20\%$	$\varepsilon_v\times H$ (cm)
1.50	B		4.8															
3.10	Rc		4.6															
4.00			2.4															
4.95	Rs	59.9	3.4	25.5	0.2264	0.167	1.02	0.051	0.102	3.88	70.5	0.055	0.093	*2*	14.1	27.2	3.96	3.77
5.90		68.2	20.9	20.1	0.2264	0.178	0.95	0.051	0.102	4.42	69.5	0.064	0.156	*3*	13.9	23.6	2.92	2.77
7.30	Ac1-1																	
8.30	As	89.6	10.7	10.1	0.1729	0.199	0.65	0.022	0.045	2.67	70.6	0.038	0.038	*1*	14.1	39.7	3.37	3.37
9.30		98.3	16.2	12.9	0.2856	0.199	1.07	0.101	0.202	13.24	69.9	0.189	0.346	*4*	14.0	7.9	3.10	1.23
10.30		107.0	18.2	8.4	0.3311	0.200	1.24	0.152	0.304	21.72	69.3	0.314	0.659	*5*	13.9	4.8	2.93	0.70
11.30		115.7	11.0	12.0	0.3539	0.200	1.32	0.182	0.364	28.08	68.7	0.409	1.068	*6*	×	×	×	×
12.30		124.4	10.5	12.0	0.3539	0.202	1.31	0.182	0.364	30.19	68.3	0.442	1.510	*7*	×	×	×	×
13.33		133.3	4.3	12.0	0.3539	0.204	1.30	0.182	0.364	33.17	67.8	0.489	1.999	*8*	×	×	×	×
14.31		141.8	2.3	12.0	0.3539	0.206	1.29	0.182	0.364	33.74	67.4	0.500	2.500	*9*	×	×	×	×
15.30		150.5	1.5	12.0	0.3539	0.207	1.28	0.182	0.364	36.35	67.1	0.541	3.041	*10*	×	×	×	×
16.40		159.2	2.6	12.0	0.3539	0.204	1.30	0.182	0.364	42.51	67.0	0.634	3.675	*11*	×	×	×	×

SBM ($r_n=0.65$) spans the three columns for $(\sigma_d/2\sigma_c')_{triax}$, $(\tau_{max}/\sigma_v')_{field}$, F_s. EBM ($H=1$ m): Summation Σ for ΔW, W-* is abbreviated in EBM. 1st stage evaluation — Liquefaction potential. 2nd stage evaluation — Strain and Settlement.

Settlement (cm) $\Sigma\,(\varepsilon_v\times H)_k$ = 11.8

Table 5 shows the soil model developed in the research [62] for evaluating liquefaction potential in the shallower soils with the water table GL.-3.1 m, wherein 11 layers of $H \approx 1$ m each are chosen excluding clayey soils. From N_1-values and fines contents F_c, $(\sigma_d/2\sigma_c')_{triax}$ for $N_L = 15$ was determined using [57], and the dissipated energy $\Sigma\Delta W/\sigma_c'$ was further derived from it by Eq. (5).

The evaluation results by the EBM Stage-I in Table 5 indicate that 5 shaded layers (2 layers of Rs and 3 layers of upper As) are to liquefy [62]. In the SBM, two layers shaded each at Rs and As are to liquefy for $r_n = 0.8$ corresponding to the $M = 9.0$ earthquake according to [59] to be slightly similar to the EBM in terms of liquefied depth.

Near this site, Taira et al. (2012) [64] carried out post-earthquake drilling/sampling of soils and X-ray CT-scan imaging of core samples for the depth GL.−2~−13 m, and observed that, in the hydraulically reclaimed soils of GL. −6.15~−8.85 m, the original sedimentary structures were completely obliterated because of liquefaction. The observation seems compatible with the present evaluation of EBM or SBM, despite the slight difference in soil profiles due to the horizontal distance of 450 m between the two points.

At this site, a 1D effective stress liquefaction analysis was also conducted to compare the results utilizing the triaxial liquefaction data on in situ intact specimens [62]. Despite sophisticated constitutive laws of soil properties incorporated in a commercially available widespread computer code, a pressure buildup ratio of $r_u = 0.90$ was recommended there as a criterion to determine the onset of liquefaction. While the analytical result using the $r_u = 0.90$ criterion was mostly compatible with the corresponding EBM & SBM results, $r_u = 0.90$ was found to correspond to the axial strain only $\varepsilon_{DA} = 0.5\%$ and the normalized dissipated energy only $\Sigma\Delta W/\sigma_c' = 0.005$ [62] in the program, which is seemingly far smaller than normally anticipated. Hence, from the viewpoint of the uniqueness of energy, it seems recommendable to pay more attention to the compatibility with the energy concept to examine the reliability of sophisticated but quite variable/tricky numerical nonlinear analyses often employed in practical design for liquefaction.

Such research efforts to calibrate nonlinear numerical results in the energy concept have begun (e.g., [65,66]) for sophisticated numerical analyses of various structures. In other words, the EBM is expected to serve as a reasonable/common scale to measure the reliability of sophisticated nonlinear numerical evaluations without no closed-form rigorous solutions.

Following the EBM Stage-I results, induced strains are evaluated in Step-7 and 8. As the energies allocated to individual layers are 1/5 of the total because of $m = 5$, the maximum induced shear strains γ_{DAmax} can be individually determined by Eq. (73) as listed in one of the right columns of Table 5 as 39.7%~4.8%. Among them, only those with the sequence number *1~4* exceed the strain $\gamma_{DAmax} = 7.5\%$ for the initial liquefaction to make the number of liquefied layers smaller from 5 to 4 in the Stage-II evaluation.

As for the surface settlement, the volumetric strains ε_v are calculated by Eq. (74) or (75) in those layers that were judged to liquefy in Stage-I following Step-9 using $(\varepsilon_v)_{\gamma DAmax=20\%} = 2.92~3.96\%$ determined by Eq. (73). In the three layers with their γ_{DAmax}-values exceeding 20%, ε_v is calculated by Eq. (74). The calculated subsidence of 11.8 cm by Step-10 at the bottom of Table 5 is slightly smaller than 15~17 cm reported [34] as the ground settlements relative to tip-supporting piles nearby. The gap between the two values may be narrowed in this site again by ejecta thicker than a few centimeters on average observed in the same report [34].

6. Summary and conclusions

In this review article, the energy-based liquefaction evaluation method (EBM) has been addressed in two different aspects in comparison with the conventional stress-based method (SBM): Energy capacity and Energy demand for liquefaction. How to compare the capacity and demand energies to make simplified and practical liquefaction evaluations has been also discussed. Furthermore, steps for

simple EBM liquefaction predictions have been presented and demonstrated by example-case histories. Major outcomes from the reviews are as follows.

Energy Capacity for Liquefaction:

(1) The capacity of liquefaction can be uniquely determined by cumulative dissipated energy $\Sigma\Delta W$ regardless of earthquake motions much better than applied stress histories employed in the SBM as demonstrated in various lab tests conducted on reconstituted and intact soil samples.

(2) The energy $\Sigma\Delta W$ is almost uniquely correlated with pore-pressure buildup ratio r_u or induced strain amplitude γ_{DA} with no regard to cyclic stress amplitudes or the number of cycles, and waveforms. With increasing $\Sigma\Delta W$, the pore-pressure ratio $r_u = \Delta u/\sigma'_c$ tends to climb up to $r_u = 1.0$ corresponding to initial liquefaction, and stay there for larger $\Sigma\Delta W$. The strain γ_{DA} keeps monotonically increasing almost in proportion to the energy with a slight nonlinearity even beyond the initial liquefaction. Hence, the energy can serve as a good index to evaluate the liquefaction intensity such as induced strain even beyond the initial liquefaction.

(3) The uniqueness of dissipated energy for liquefaction can be confirmed in cyclic simple shear tests which can best mimic in situ stress conditions during earthquakes. For cyclic triaxial tests in contrast, care is needed in dealing with the measured dissipated energy because the uniqueness of energy appears to fail due to the stress anisotropy inherent to the cyclic loading triaxial test system.

(4) The energy capacity in EBM is often expressed in the cumulative dissipated energy normalized by initial effective confining stress σ'_c as $\Sigma\Delta W/\sigma'_c$. This is reasonable because ΔW (energy per unit volume; the same dimension as stress) can be nondimensionalized by σ'_c (stress), though the correlation of $\Sigma\Delta W/\sigma'_c$ versus pore-pressure ratio r_u or induced strain ε may not be fully independent of σ'_c in soil tests.

(5) The *CSR* versus number of cycles N_c curve employed in the SBM can be interpreted as an equal-energy line in the EBM corresponding to a particular pore-pressure buildup ratio or induced strain. Hence, the liquefaction performance can be uniquely determined in the EBM solely by the dissipated energy or the capacity energy without referring to an equivalent number of cycles for liquefaction N_L or the stress reduction coefficient r_n, unlike the SBM.

(6) Thus, an empirical correlation has been established to evaluate the capacity energy for liquefaction from the *CRR* of the SBM for particular N_L values. Using triaxial tests on intact samples recovered from various sites, Eqs. (5) & (6) have been obtained connecting the *CRR* for N_L=15 or 20 to the corresponding energy $\Sigma\Delta W/\sigma'_c$ uniquely with no regard to the difference in soil properties.

(7) Concerning the influence of earthquake wave irregularities investigated by cyclic torsional liquefaction tests using six recorded motions with widely spanned damage level D_L of the fatigue theory, the energy $\Sigma\Delta W/\sigma'_c$ is effective in uniquely determining the induced strain at least up to the initial liquefaction of γ_{DA}=7.5%. This indicates that the energy concept is superior to the fatigue theory, a theoretical basis of the SBM in dealing with wave irregularity, as the liquefaction susceptibility can be governed solely by the dissipated energy despite the widely varied D_L-values.

(8) For strain ranges beyond initial liquefaction ($\gamma_{DA} > 7.5\%$), however, the energy for e.g. $\gamma_{DA} = 15\%$ or larger tends to decrease slightly with an increasing number of cycles or decreasing stress amplitudes in irregular motions. This is probably due to stress bias temporarily working at irregular stress peaks where larger biased stress tends to make the soil more resistant and require larger dissipated energy in dilative soils considered here.

Energy Demand for Liquefaction to Compare with Capacity:

(9) Compared to the energy capacity, the energy demand for liquefaction has scarcely been discussed and more often dealt with implicitly through numerical analyses directly using design earthquake motions. Besides, the seismologically given empirical formula by Gutenberg [6] was utilized in early-time liquefaction evaluations by several researchers, though the energy demand was not directly compared with the capacity but used only as an index for judging liquefaction susceptibility based on previous liquefaction case histories.

(10) One of the highlights of the energy-based liquefaction evaluation developed here is the capability to quantify the total amount of demand energy from upward design earthquake waves and to directly compare them with the energy capacity for liquefaction, not only to predict liquefaction potential, but also to evaluate the extent of liquefaction at a glance. This includes induced strains in individual layers and ground settlements without resorting to complicated nonlinear effective stress analyses.

(11) In the EBM developed here, the demand energy of a given earthquake E_{uf} is determined in Eq. (68) as cumulative upward wave energy using a site-specific design motion. Numerous vertical array strong earthquake motion data during strong earthquakes of recent decades in Japan demonstrated that the E_{uf}-value tends to monotonically decrease with decreasing soil depth depending on the corresponding impedance ratio.

(12) In those sites where specific design motions are not available, empirical formulas, Eq. (69), derived from the vertical array database may be used to roughly evaluate Eu at particular ground depths by employing the well-known formula seismologically given in Eq. (70).

(13) The energy dissipation rate during wave propagations in situ $\Delta E/E_u$ is very similar to that during cyclic loading tests $\Delta W/2W_-$ and is mostly reproducible in laboratory cyclic loading tests if the energy-recycling effect during cyclic loading is taken into account when evaluating $2W_-$. Since the energy dissipated for liquefaction, in situ ΔE and laboratory ΔW, respectively, should be the same; $\Delta E = \Delta W \times H$, for a soil layer of thickness H, the cumulative wave energy E_u coming up through unit horizontal area is to be compared with cumulative strain energy $\Sigma 2W_- \times H$ in the liquefaction evaluation.

(14) Because of 100% reflection of the SH-wave at a free ground surface of zero shear stress, the strain energy cannot be present near the surface to compensate for the dissipated energy for liquefaction. In this regard, wave propagation studies using harmonic and earthquake waves have led to a simple approximation that only half of the upward wave energy is available to compensate for the dissipated energy for liquefaction in soils shallower than a quarter-wavelength $\lambda/4$ from the surface. Considering that $\lambda/4$ is normally larger than 20 m in practical liquefaction problems, the upward energy Eu should be compared with the strain energy twice larger; $\Sigma W_-^* \equiv 2 \times \Sigma 2W_-$.

Evaluation Steps and Case Study Examples:

(15) Ten steps of the energy-based liquefaction evaluation divided into Stage-I and Stage-II are proposed. In Stage-I (Step 1~6), the capacity and demand energies are quantified from site/soil and earthquake conditions and compared layer by layer individually to know the spatial extent of initial liquefaction corresponding to $\gamma_{DAmax} = 7.5\%$ (pore-pressure buildup ratio $r_u = 100\%$) and their sequence of occurrence in terms of *AER* (Accumulated Energy Ratio) in Eq. (71) where liquefaction occurs only for $AER \leq 1.0$. Thus, unlike the conventional SBM, the EBM has the potential to decide the extent of liquefaction within the availability of the total energy demand.

(16) In Stage-II (Step 7~10), the same upward energy Eu is equally allocated exclusively to those layers judged as liquefiable in Stage-I to evaluate induced γ_{DAmax} and post-liquefaction ground

settlements *S*. The equal energy allocation may not be theoretically rigorous but tends to approach nearer to actual liquefaction performance than Stage-I by concentrating larger induced strains in a smaller number of liquefied layers.

(17) The impact of frequency content in input motions on liquefaction potential has been demonstrated by a simple uniform model where, despite the same input motion of the same acceleration amplitude given to a uniform sand model, the liquefaction potential, induced strain, and ground settlement are evaluated significantly lower when the time axis is compressed by 1/2 in the EBM, while the corresponding difference was found marginal in the SBM. Also found was a general trend that liquefaction tends to occur earlier in shallower layers on uniform sand layers in the EBM, while it is reversed in the SBM.

(18) A liquefaction case history in a loose sandy fill with its recorded acceleration of only 0.056 g during a far-field earthquake has been successfully replicated using a recorded motion nearby in the EBM, presumably because the wave energy was large enough due to the large magnitude of $M_J = 8.0$, while the SBM predicted no possibility of liquefaction, quite different from the actual behavior.

(19) Two severe liquefaction cases in hydraulically filled residential lands during a far-field M_J=9.0 earthquake have been studied using acceleration records nearby. Both the EBM (Stage-I) and SBM have similarly predicted heavy liquefaction involving most layers in shallow depth, though, in the EBM Stage-II, the number of liquefiable layers tends to decrease from Stage-I, while their induced strains tend to concentrate to a smaller number of layers with higher liquefaction susceptibility. The post-liquefaction settlements calculated in the EBM Stage-II have been compared with the performance observed at the two sites and found a fair agreement if the thickness of ejected sands is considered.

Consequently, the energy-based liquefaction evaluation has been comprehensively reviewed from various aspects to recognize that it has been mature enough for practical use in engineering design. It can consider a variety of earthquake motions exclusively in terms of demand energy. The capacity energy, uniquely connected with the resistant stress *CRR* in the SBM, is compared with the demand energy to readily evaluate liquefaction potential, induced strain, and settlement without resorting to sophisticated numerical analyses.

Moreover, considering the uniqueness of energy, it can serve as a common scale to measure the reliability of nonlinear numerical liquefaction evaluation tools which attract designers because of the modeling capability of complicated boundary value problems but have no rigorous solutions to depend upon.

There are limitations in the EBM that need to be overcome in future studies. The most crucial is the accumulation of in situ liquefaction case histories in terms of surface manifestations including lateral deformations and settlements to demonstrate the applicability of the EBM in comparison with the SBM for various seismic and geotechnical conditions. Induced strains and settlements calculated in the EBM may be compared first with in situ observation or model shaking table tests, and also with sophisticated stress-based numerical tools to know how well this simplified evaluation works in engineering designs. Another challenge is how the effect of initial shear stress should be considered so that the EBM can be reasonably applied to liquefaction designs concerning slope failures and soil structure interaction problems. With these efforts, the EBM is hoped to serve as a major player in liquefaction-related engineering designs and also a common scale to calibrate numerical results of practical problems in terms of energy.

Acknowledgments

Use of AI tools declaration

The author declares that Artificial Intelligence (AI) tools have not been used in the creation of this article.

Conflicts of interest

The author declares no conflict of interest concerning this article.

Data availability statement

All data presented in this study are available for research purposes upon request directly to the present author.

References

1. Seed HB, Idriss IM (1971) Simplified procedure for evaluating soil liquefaction potential. *J Soil Mech Found Div* 97: 1249–1273. https://doi.org/10.1061/JSFEAQ.0001662
2. Nemat-Nasser S, Shokooh A (1979) A unified approach to densification and liquefaction of cohesionless sand in cyclic shearing. *Can Geotech J* 16: 659–678. https://doi.org/10.1139/t79-076
3. Davis RO, Berrill JB (1982) Energy Dissipation and Seismic Liquefaction of Sands. *Earthquake Eng Struct Dyn* 10: 59–68.
4. Berrill JB, Davis RO (1985) Energy dissipation and seismic liquefaction of sands: Revised model. *Soils Found* 25: 106–118. https://doi.org/10.3208/sandf1972.25.2_106
5. Law KT, Cao YL, He GN (1990) An energy approach for assessing seismic liquefaction potential. *Can Geotech J* 27: 320–329. https://doi.org/10.1139/t90-043

6. Gutenberg B (1956) The energy of earthquakes. *Q J Geol Soc Lond* 112: 1–14. https://doi.org/10.1144/GSL.JGS.1956.112.01-04.02

7. Towhata I, Ishihara K (1985) Shear work and pore water pressure in undrained shear. *Soils Found* 25: 73–84. https://doi.org/10.3208/sandf1972.25.3_73

8. Yanagisawa E, Sugano T (1994) Undrained shear behaviors of sand given shear work. *Intern. Conf. on SMFE* (Special Volume on Performance of Ground and Soil Structures during Earthquakes), New Delhi, India, Balkema Publishers, 155–158.

9. Figueroa JL, Saada AS, Liang L, et al. (1994) Evaluation of soil liquefaction by energy principles. *J Geotech Geoenvironmental Eng* 120: 1554–1569. https://doi.org/10.1061/(ASCE)0733-9410(1994)120:9(1554)

10. Baziar MH, Sharafi H (2011) Assessment of silty sand liquefaction potential using hollow torsional tests–An energy approach, *Soil Dyn Earthq Eng* 31: 857–865. https://doi.org/10.1016/j.soildyn.2010.12.014

11. Pan K, Yang ZX (2017) Evaluation of the liquefaction potential of sand under random loading conditions: equivalent approach versus energy-based method. *Soil Dyn Earthq Eng* 92: 650–665. https://doi.org/10.1080/13632469.2017.1398693

12. Azeiteiro RJN, Coelho PALF, Taborda DMG, et al. (2017) Energy-based evaluation of liquefaction potential under non-uniform cyclic loading. *Soil Dyn Earthq Eng* 92: 650–665. https://doi.org/10.1016/j.soildyn.2016.11.005

13. Green RA, Mitchell JK, Polito CP (2000) An energy-based excess pore pressure generation model for cohesionless soils. *Proc. John Booker Memorial Symposium*, Sydney, Australia, Balkema Publishers.

14. Jafarian Y, Towhata I, Baziar MH, et al. (2012) Strain energy based evaluation of liquefaction and residual pore water pressure in sands using cyclic torsional shear experiments. *Soil Dyn Earthq Eng* 35: 13–28. https://doi.org/10.1016/j.soildyn.2011.11.006

15. Karimzadeh AA, Leung AK, Amini PF (2021) Energy-Based Assessment of Liquefaction Resistance of Rooted Soil. *J Geotech Eng* 148. https://doi.org/10.1061/(ASCE)GT.1943-5606.0002717

16. Baziar MH, Alibolandi M (2023) Liquefaction Evaluation of Microbial Induced Calcium Carbonate Precipitation (MICP) Treated Sands; A Strain Energy Approach. *J Earthquake Eng* 27: 4512–4525. https://doi.org/10.1080/13632469.2023.2171508

17. Kazama M, Suzuki T, Yanagisawa E (1999) Evaluation of dissipated energy accumulated in surface ground and its application to liquefaction prediction. *J Japan Soc Civil Eng* 631: 161–177. https://doi.org/10.1080/13632469.2023.2171508

18. Kokusho T (2013) Liquefaction potential evaluation–energy-based method versus stress-based method. *Can Geotech J* 50: 1–12. https://doi.org/10.1139/cgj-2012-0456

19. Kokusho T, Kaneko Y (2018) Energy evaluation for liquefaction-induced strain of loose sands by harmonic and irregular loading tests. *Soil Dyn Earthq Eng* 114: 362–377. https://doi.org/10.1016/j.soildyn.2018.07.012

20. Kokusho T, Tanimoto S (2021) Energy capacity versus liquefaction strength investigated by cyclic triaxial tests on intact soils. *J Geotech Geoenvironmental Eng* 147: 1–13. https://doi.org/10.1061/(ASCE)GT.1943-5606.0002484

21. Kayen RE, Mitchell JK (1997) Assessment of Liquefaction Potential During Earthquakes by Arias Intensity. *J Geotech Geoenvironmental Eng* 123: 1162–1174. https://doi.org/10.1061/(ASCE)1090-0241(1997)123:12(1162)

22. Arias A (1970) A measure of earthquake intensity. *Seismic Design of Nuclear Power Plants.* Hansen, R.J., Ed.; MIT Press: Cambridge, MA, USA, 438–483.

23. Kokusho T (2017) Liquefaction Potential Evaluations by Energy-Based Method and Stress-Based Method for Various Ground Motions: Supplement. *Soil Dyn Earthq Eng* 95: 40–47. https://doi.org/10.1016/j.soildyn.2017.01.033

24. Kokusho T, Motoyama R (2002) Energy dissipation in surface layer due to vertically propagating SH wave. *J Geotech Geoenvironmental Eng* 128: 309–318. https://doi.org/10.1061/(ASCE)1090-0241(2002)128:4(309)

25. Kokusho T, Suzuki T (2011) Energy flow in shallow depth based on vertical array records during recent strong earthquakes. *Soil Dyn Earthq Eng* 31: 1540–1550. https://doi.org/10.1016/j.soildyn.2011.06.003

26. Kokusho T, Suzuki T (2012) Energy flow in shallow depth based on vertical array records during recent strong earthquakes (Supplement). *Soil Dyn Earthq Eng* 42: 138–142. https://doi.org/10.1016/j.soildyn.2012.06.013

27. Kokusho T, Mimori Y (2015) Liquefaction potential evaluations by energy-based method and stress-based method for various ground motions. *Soil Dyn Earthq Eng* 75: 130–146. https://doi.org/10.1016/j.soildyn.2015.04.002

28. Idriss IM, Boulanger R (2008) Soil liquefaction during earthquakes, Earthquake Engineering Research Institute, MNO-12.

29. Lau KK, Kontoe S, Anatolatis G (2019) A critical comparison between stress and energy based methods for the evaluation of liquefaction potential. *Proc. 2019 Conf. on Earthquake risk and engineering towards resilient world*, London.

30. Kokusho T (2014) Seismic base-isolation mechanism in liquefied sand in terms of energy. *Soil Dyn Earthq Eng* 63: 92–97. https://doi.org/10.1016/j.soildyn.2014.03.015

31. Kokusho T (2020) Energy-based liquefaction evaluation for induced strain and surface settlement—Evaluation steps and case studies. *Soil Dyn Earthq Eng* 143: 106552. https://doi.org/10.1016/j.soildyn.2020.106552

32. Annaki M, Lee KL (1977) Equivalent uniform cycle concept for soil dynamics. *J Geotech Geoenvironmental Eng* 103: 549–564. https://doi.org/10.1061/AJGEB6.0000436

33. Green RA, Terri GA (2005) Number of equivalent cycles concept for liquefaction evaluations-revisited. *J Geotech Geoenvironmental Eng* 131: 477–488. https://doi.org/10.1061/(ASCE)1090-0241(2005)131:4(477)

34. Sasaki T, Ishihara M, Tanimoto S, et al. (2016) PWRI Research Note, No. 4352, Public Works Research Institute (in Japanese).

35. Meyerhof GG (1957) Discussion, Proc. 4th international Conference on SMFE, 3, 110

36. Ishihara K, Tatsuoka F, Yasuda S (1975) Undrained deformation and liquefaction of sand under cyclic stresses. *Soils Found* 15: 29–44. https://doi.org/10.3208/sandf1972.15.29

37. Kokusho T (2017) Chap.1: Elastic wave propagation in soil, *Innovative earthquake soil dynamics*, *CRC Press,* Taylor and Francis Group. https://doi.org/10.1201/9781315645056-1

38. Sako N (2019) Personal data supply of cyclic torsional simple shear test on Toyoura sand from Soil Laboratory of Nihon University. Tokyo: Nihon Univ.

39. Kokusho T (2020) Earthquake-induced flow liquefaction in fines-containing sands under initial shear stress by lab tests and its implication in case histories. *Soil Dyn Earthq Eng* 130: 105984. https://doi.org/10.1016/j.soildyn.2019.105984

40. Gutenberg B, Richter CF (1942) Earthquake magnitude, intensity, energy and acceleration. *Bull Seismol Soc Am* 32: 163–191. https://doi.org/10.1785/BSSA0320030163

41. Gutenberg B, Richter CF (1956) Earthquake magnitude, intensity, energy and acceleration (Second paper). *Bull Seismol Soc Am* 46: 105–145. https://doi.org/10.1785/BSSA0460020105

42. Sarma SK (1971) Energy Flux of Strong Earthquakes. *Techtonophysics* 11: 159–173. https://doi.org/10.1016/0040-1951(71)90028-X

43. Kokusho T, Motoyama R, Motoyama H (2007) Wave energy in surface layers for energy-based damage evaluation. *Soil Dyn Earthq Eng* 27: 354–366. https://doi.org/10.1016/j.soildyn.2006.08.002

44. Timoshenko S, Goodier JN (1951) Theory of Elasticity, McGraw-Hill.

45. Bath M (1956) Earthquake energy and magnitude. *Phys Chem Earth* 23: 115–165. https://doi.org/10.1016/0079-1946(66)90003-6

46. Schnabel PB, Lysmer J, Seed HB (1972) SHAKE—A Computer Program for Earthquake Response Analysis of Horizontally Layered Sites, *Report EERC 72–12*; University of California, Berkeley: Berkeley, CA, USA.

47. Ishihara K (1996) Soil Behaviour in Earthquake Geotechnics, *Oxford Science Publications*: New York, NY, USA, 3.1.3, 22–28. https://doi.org/10.1093/oso/9780198562245.003.0001

48. Joyner WB, Fumal TE (1984) Use of measured shear-wave velocity for predicting geologic site effects on strong ground motion. *Proc. 8th World Conf. on Earthquake Engineering*, San Francisco, 2, 777–783.

49. Kokusho T (2022) Energy demand in surface soils for earthquake engineering by vertical array strong motion records. *Geosciences* 12: 102. https://doi.org/10.3390/geosciences12020102

50. Utsu T (1982) Relationships Between Earthquake Magnitude Scales. *Bull Earthq Res Inst Univ Tokyo* 57: 465–497.

51. JGS committee report (2019) Research Committee on Liquefaction Potential Evaluation based on Energy, Japanese Geotechnical Society (in Japanese).

52. Silver ML, Seed HB (1971) Volume changes in sands during cyclic loading. *J Soil Mech Found Div* 97: 1171–1182. https://doi.org/10.1061/JSFEAQ.0001658

53. Tatsuoka F, Sasaki T, Yamada S (1984) Settlements in saturated sand induced by cyclic undrained simple shear, *Proc. 8th World Conference on Earthquake Engineering*, San Francisco, 3: 95–102.

54. Nagase H, Ishihara K (1988) Liquefaction-induced compaction and settlement of sand during earthquakes. *Soils Found* 28: 65–76. https://doi.org/10.3208/sandf1972.28.65

55. Tsukamoto Y, Ishihara K, Sawada S (2004) Settlement of silty sand deposits following liquefaction during earthquakes. *Soils Found* 44: 135–148. https://doi.org/10.3208/sandf.44.5_135

56. Ishihara K, Yoshimine M (1992) Evaluation of settlements in sand deposits following liquefaction during earthquakes. *Soils Found* 32: 173–188. https://doi.org/10.3208/sandf1972.32.173

57. Japan Road Association (2017) *Specifications for highway bridges-Part V Seismic Design-*, Japan Road Association, (in Japanese).

58. Hardin BO, Drnevich VP (1972) Shear modulus and damping in soils: Design equations and curves. *J Soil Mech Found Div* 98: 667–692. https://doi.org/10.1061/JSFEAQ.0001760

59. Tokimatsu K, Yoshimi Y (1983) Empirical correlation of soil liquefaction based on SPT N-value and fines content. *Soils Found* 23: 56–74. https://doi.org/10.3208/sandf1972.23.4_56

60. Kokusho T, Mukai A, Kojima T (2014) Liquefaction Behavior in Urayasu and Physical Properties of Fines. In *Proc. 14th Japan Earthquake Engineering Symposium* (in Japanese).

61. Kokusho T (2015) Liquefaction research by laboratory tests versus in situ behavior, 5th Ishihara Lecture, *Proc. 6th International Conference on Earthquake Geotechnical Engineering*, Christchurch, NZ.

62. Azuno K, Kokusho T (2020) A case study of energy-based liquefaction evaluation method compared with FL-method and effective-stress analysis –, *JGS committee report, Research Committee on Liquefaction Potential Evaluation based on Energy*, Japanese Geotechnical Society (in Japanese).

63. NIED: National Research Institute for Earth Science and Disaster Resilience. https://www.bosai.go.jp/ (accessed on 20 December 2021).

64. Taira A, Iijima K, Igarashi C, et al. (2012) Identification of a soil liquefied layer due to the 2011 off the Pacific coast of Tohoku Earthquake using X-ray CT scan imaging: An example from core samples from Maihama 3-chome, Urayasu city. *J Geol Soc* 118: 410–418. https://doi.org/10.5575/geosoc.2012.0029

65. Ko KW, Kayen RE (2024) Energy-based and strain-based methods for estimation of pore water pressure within liquefied soil layers. *J Geotech Geoenviron Eng* 150. https://doi.org/10.1061/JGGEFK.GTENG-11458

66. Ko KW, Kayen RE, Kokusho T, et al. (2024) A Case Study at the Port of Kushiro, Hokkaido, 2003 Tokachi-Oki Earthquake. *J Geotech Geoenviron Eng* (In press).